

## THINGS: THE HI NEARBY GALAXY SURVEY

FABIAN WALTER<sup>1</sup>, ELIAS BRINKS<sup>2</sup>, W.J.G. DE BLOK<sup>3</sup>, FRANK BIGIEL<sup>1</sup>, ROBERT C. KENNICUTT, JR.<sup>4</sup>, MICHELE D. THORNLEY<sup>5</sup> ADAM K. LEROY<sup>1</sup>

*Draft version October 12, 2008*

### ABSTRACT

We present “The HI Nearby Galaxy Survey (THINGS)”, a high spectral ( $\leq 5.2 \text{ km s}^{-1}$ ) and spatial ( $\sim 6''$ ) resolution survey of HI emission in 34 nearby galaxies obtained using the NRAO Very Large Array (VLA). The overarching scientific goal of THINGS is to investigate fundamental characteristics of the interstellar medium (ISM) related to galaxy morphology, star formation and mass distribution across the Hubble sequence. Unique characteristics of the THINGS database are the homogeneous sensitivity as well as spatial and velocity resolution of the HI data which is at the limit of what can be achieved with the VLA for a significant number of galaxies. A sample of 34 objects at distances  $2 \lesssim D \lesssim 15$  Mpc (resulting in linear resolutions of  $\sim 100$  to  $500$  pc) are targeted in THINGS, covering a wide range of star formation rates ( $\sim 10^{-3}$  to  $6 M_{\odot} \text{ yr}^{-1}$ ), total HI masses  $M_{\text{HI}}$  ( $0.01$  to  $14 \times 10^9 M_{\odot}$ ), absolute luminosities  $M_{\text{B}}$  ( $-11.5$  to  $-21.7$  mag) and metallicities ( $7.5$  to  $9.2$  in units of  $12 + \log[\text{O}/\text{H}]$ ). We describe the setup of the VLA observations, the data reduction procedures and the creation of the final THINGS data products. We present an atlas of the integrated HI maps, the velocity fields, the second moment (velocity dispersion) maps and individual channel maps of each THINGS galaxy. The THINGS data products are made publicly available through a dedicated webpage. Accompanying THINGS papers address issues such as the small-scale structure of the ISM, the (dark) matter distribution in THINGS galaxies, and the processes leading to star formation.

*Subject headings:* surveys — galaxies: structure — galaxies: ISM — ISM: general — ISM: atoms — radio lines: galaxies

### 1. INTRODUCTION

For the past few decades studies of the atomic interstellar medium (ISM), via observations of the 21-cm line of atomic hydrogen (HI), have proven to be fundamental for our understanding of the processes leading to star formation, the dynamics and structure of the ISM, and the (dark) matter distribution, thereby touching on major issues related to galaxy evolution. Since the detection of the HI line (whose forbidden hyperfine structure line had been predicted by van de Hulst in 1945), this line has been used as the ‘workhorse’ for studies of the atomic gas in our own and other galaxies. One of its benefits is that, in contrast to optical or UV radiation, HI emission does not suffer from extinction by interstellar dust. In addition, its Doppler shift provides information about the velocity of the emitting gas. This provides important information on the physical properties of the interstellar gas and the associated kinematics of the ISM. Furthermore, 21 cm emission is (under most circumstances) optically thin; this means that the total amount of HI seen along a particular line of sight (HI column density) can be converted directly into an HI mass density and, integrated over an entire galaxy, a total HI mass.

Early studies, using single dish telescopes (yielding res-

olutions of  $\sim 10'$ ), naturally concentrated on performing detailed studies of the Galaxy and obtaining some global measurements of other nearby systems. Only after radio interferometers came into operation, did it become feasible to obtain detailed, spatially resolved HI images of external galaxies. However, given the intrinsically low surface brightness of the HI emission, large collecting areas are needed, in particular if high-resolution ( $< 1'$ ) imaging is desired.

Ever since the first pioneering observations with large interferometers in the late 1970’s, many galaxies have been mapped with ever increasing resolution and sensitivity (see, e.g., Bosma 1981a/b, Brinks & Bajaja 1986, Begeman 1987, Kamphuis et al. 1991, Puche et al. 1992, Braun et al. 1995, Staveley-Smith et al. 1997, Walter & Brinks 1999, Kim et al. 1999, de Blok & Walter 2000, Verheijen & Sancisi 2001, Walter & Brinks 2001, Ott et al. 2001, Walter et al. 2002, Swaters et al. 2002). Although remarkable progress has been achieved in these studies, the lack of high-resolution HI observations in a significant sample of nearby galaxies precludes a systematic study of the physical characteristics and dynamics of the atomic ISM.

This paper describes ‘The HI Nearby Galaxy Survey’ (THINGS) which was obtained at the Very Large Array of the National Radio Astronomy Observatory<sup>6</sup>. The goal of THINGS was to obtain high quality observations of the atomic ISM of a substantial sample of nearby galaxies, covering a wide range of Hubble types, star formation rates, absolute luminosities, and metallicities to

<sup>1</sup> Max-Planck-Institut für Astronomie, Königstuhl 17, D-69117, Heidelberg, Germany; walter@mpia.de

<sup>2</sup> Centre for Astrophysics Research, University of Hertfordshire, Hatfield AL10 9AB, U.K.

<sup>3</sup> Department of Astronomy, University of Cape Town, Rondebosch 7700, South Africa

<sup>4</sup> Institute of Astronomy, University of Cambridge, Madingley Road, Cambridge CB3 0HA, UK

<sup>5</sup> Department of Physics and Astronomy, Bucknell University, Lewisburg, PA 17837, USA

<sup>6</sup> The National Radio Astronomy Observatory is a facility of the National Science Foundation operated under cooperative agreement by Associated Universities, Inc.

address key science questions regarding the ISM in galaxies. A key characteristic of the THINGS database is the homogeneous sensitivity, as well as spatial and velocity resolution that is at the limit of what can be achieved in studies of extragalactic HI with the VLA. Most of the galaxies in THINGS were drawn from the “*Spitzer* Infrared Nearby Galaxies Survey (SINGS)” (Kennicutt et al. 2003), a multi-wavelength project designed to study the properties of the dusty ISM in nearby galaxies, to ensure that multi-wavelength observations for each galaxy are available for further analysis.

Science capitalizing on the unique properties of the THINGS data products will be presented in accompanying papers: de Blok et al. (2008) present a detailed analysis of high-resolution rotation curves and mass models (including new constraints for the stellar mass-to-light ratio) for the majority of THINGS galaxies. Trachternach et al. (2008) present a detailed analysis of the centres of the THINGS targets and perform a harmonic decomposition of the velocity fields to constrain the non-circular motions in these objects. Oh et al. (2008) present a new method to remove these non-circular motions from the velocity fields to derive accurate rotation curves unaffected by such motions. The star formation properties are addressed in papers by Leroy et al. (2008) and Bigiel et al. (2008). Leroy et al. test various star formation and threshold recipes that have been proposed to explain the observed star formation in galaxies. They also describe a new method for creating star formation rate maps of individual galaxies. Bigiel et al. perform a pixel-by-pixel comparison of the SFR and measured gas densities for a sample of THINGS galaxies to constrain the ‘star formation law’ on small scales. Tamburro et al. (2008) use the offset seen between the HI and 24 micron emission to derive an average timescale for star formation to commence in spiral arm environments. The wealth of small-scale structure in the ISM revealed in the THINGS data products is analyzed by Bagetakos et al. (in prep.) and Usero et al. (in prep.). Bagetakos et al. concentrate on structures generally referred to as HI holes whereas Usero et al. study the HI peak brightness temperature distribution. Brinks et al. (in prep.) present a study of the HI edges of a sample of THINGS galaxies. Zwaan et al. (2008) use the THINGS data to compare the HI properties in nearby galaxies to the HI absorption properties found in Damped Lyman- $\alpha$  Absorbers systems at high redshift. Finally, the THINGS dataset is of sufficiently high quality that alternative data imaging techniques can be explored. This is described in Rich et al. (2008) who use the THINGS data to investigate the applicability of the Multi-Scale CLEAN algorithm.

This paper is organized as follows: in Sec. 2 we give a description of the sample selection and the setup of the observations. The observations and data reduction details are described in Sec. 3. Sec. 4 presents the resulting THINGS data products (cubes and moment maps). Finally, a summary is presented in Sec. 5.

## 2. THINGS SURVEY DESIGN

### 2.1. Sample Selection

To ensure multi-wavelength coverage of the sample galaxies, THINGS targets were mostly drawn from SINGS (Kennicutt et al. 2003). Some of the THINGS targets are not part of SINGS (as SINGS did not in-

clude a few key targets covered in *Spitzer Space Telescope* guaranteed time observations). Galaxies were chosen to cover the full range of physical properties, from low-mass, metal-poor, quiescent dwarf galaxies to massive spiral galaxies. The THINGS galaxies and their properties are listed in Table 1. Some of our sample galaxies form part of the WHISP survey obtained at the Westerbork radio telescope (e.g., Swaters et al. 2002) and we have labeled these targets in Table 1.

Early type (E/S0) galaxies were excluded from the THINGS target list as their ISM is dominated by hot gas with little, if any, in a neutral atomic phase. Edge-on systems (e.g., M82) were also excluded as the radial structure of the ISM cannot be disentangled from projection effects in these systems. The sample was furthermore limited to galaxies at distances  $D < 15$  Mpc to ensure that structures smaller than 500 pc can be resolved (this is limited by the maximum HI resolution of  $6''$  that can realistically be achieved at the VLA, as discussed below). Local Group galaxies were also excluded because of their large size on the sky. The 34 galaxies in THINGS are listed in Table 1; the galaxy parameters listed in this table are adopted for all THINGS papers listed in the introduction, unless explicitly stated otherwise. Throughout this paper, galaxies are sorted by Right Ascension (RA).

### 2.2. Spatial Resolution

The main scientific goals for THINGS require an angular resolution of a few hundred parsecs in order to resolve neutral atomic gas complexes, to trace the fine structure of the HI and to resolve spiral arms. This resolution is also required to accurately derive the central shape and slope of the rotation curve of a galaxy. Given the distances to our sample galaxies, this necessitates an angular resolution of  $\sim 6''$ , which can be achieved using the VLA in its B array configuration (baselines: 210 m to 11.4 km). B array observations, however, are only sensitive to small-scale structure. Therefore, additional D array (35 m to 1.03 km) and C array (35 m to 3.4 km) data are needed to recover extended emission in the objects. Objects at declinations lower than about  $-20$  degrees are observed with the extended north arm (BnA array) to ensure a homogeneous  $uv$  coverage. Reaching even higher spatial resolution at the VLA is in principle possible (using the A configuration) but would require integration times per object of  $\sim 50$  hours which rules out a large survey. We note that our final resolution of  $6''$  is well matched to that typically obtained for the other data products from the *Spitzer Space Telescope* (e.g., resolution at  $24\mu\text{m}$ :  $\sim 6''$ ) and the *Galaxy Evolution Explorer GALEX* (resolution in Near-Ultraviolet:  $\sim 5''$ ).

### 2.3. Velocity Resolution

Many of the THINGS science goals require high *velocity* resolution: the  $1\sigma$  velocity dispersion of the warm neutral medium is about  $6 - 7 \text{ km s}^{-1}$  (full width half maximum, FWHM:  $\sim 16 \text{ km s}^{-1}$ ); therefore all observations are done with at least  $5 \text{ km s}^{-1}$  velocity resolution in order to Nyquist sample the HI line. The latter constraint implied that many observations in the VLA archive could not be incorporated in our analysis (as typical velocity resolutions chosen for those observations were poorer). Taking into account the velocity range over

which HI was detected in earlier studies (and the limited configurations of the current VLA correlator), two galaxies have been observed at  $1.3 \text{ km s}^{-1}$  resolution, 15 at  $2.6 \text{ km s}^{-1}$  and 17 at  $5.2 \text{ km s}^{-1}$  (see Table 2 for a detailed summary). Two targets (NGC 2841 and NGC 3521) had to be observed twice over two adjacent velocity ranges to cover the large HI line-width. Most observations are done using two orthogonal polarizations (see Table 2 for details). Depending on the width of the HI profile, either correlator mode 2AD or mode 4 is used. The latter setup results in 2 IFs, each IF using 2 polarizations. The IFs can be tuned independently and are set at velocities such that the last channels of one IF overlap with the first few channels of the second IF, allowing roughly twice the bandwidth of a single IF to be covered in a single observation.

#### 2.4. Sensitivity Considerations

High sensitivity is also a key requirement for many THINGS science goals. In B-array, the gain is of order 15 K per mJy for a  $6''$  beam. Observations of on average 7 hours on source, observing 2 polarizations, reach a  $1\sigma$  rms noise of typically  $0.4 \text{ mJy beam}^{-1}$  (or 6 K) which corresponds to a column density limit of  $\sim 3.2 \times 10^{20} \text{ cm}^{-2}$  (a detection in 2 channels of  $5 \text{ km s}^{-1}$  width at the  $3\sigma$  level). Higher surface brightness sensitivities can be reached by convolving the data. THINGS observations have typical column density sensitivities of  $4 \times 10^{19} \text{ cm}^{-2}$  at  $30''$  resolution which is adequate to trace the outer regions of the galaxies. Typical observing times were: 1.5, 2.5, and 7 hours for the D, C and B array configurations (observations are longer in the extended array to account for the reduced surface brightness sensitivity). The amount of observing times required at the VLA and the different array configurations needed are summarized in Table 2. We have included as much archival data in our analysis as possible and the respective project IDs are also given in Table 2. These archival data were observed in various setups, but with at least the minimum equivalent observing time, and spatial/velocity resolution as required for the new observations. The total observing time for this project (including the archival data) is  $\sim 500$  hours.

Given the substantial amount of observing time required at the VLA for THINGS, data for this project were taken over two years, from Summer 2003 to Summer 2005. Based on the requirements outlined in Sec. 2, the key observational data for each galaxy are summarized in Table 2:

**column 1:** galaxy name

**column 2:** VLA array used

**column 3:** program code (AW605: THINGS; others: archival data)

**column 4:** observing date (local time: MST/MDT)

**column 5/6:** start/end of observations (IAT)

**column 7:** duration of observations (hours/minutes)

**column 8/9:** name of phase calibrator and its flux density

**column 10/11:** coordinates of pointing centre of the array (equinox given in column 16)

**column 12:** correlator mode

**column 13:** total bandwidth in MHz

**column 14:** number of channels per IF

**column 15:** channel width in  $\text{km s}^{-1}$

**column 16:** equinox

**column 17:** Barycentric (heliocentric) central velocities in  $\text{km s}^{-1}$ . The observations were done assuming the optical definition for the Doppler shift. In case two independent IFs were used, the central velocity of the second IF is also listed.

### 3. OBSERVATIONS AND DATA REDUCTION

#### 3.1. Amplitude/Phase calibration

The calibration and data reduction is performed using standard routines in the AIPS package<sup>7</sup>. The absolute flux scale for the data is determined by observing one of the standard primary calibrators used at the VLA (3C286=J1331+305; 3C48=J0137+331 or 3C147=J0542+498, using the flux scale of Baars et al. 1977, task SETJY). The primary calibrator is used for the bandpass corrections as well (task BPASS). The time variable phase and amplitude calibration is done using nearby, secondary calibrators which are unresolved for the arrays used (CALIB). The names and fluxes of these secondary calibrators are given in Table 2 for each observing run. Note that in some cases different array configurations required the choice of different calibrators for an individual galaxy. The uncertainty of the flux calibration ( $\sim 5\%$ ) dominates all measurements of HI flux densities derived in the remainder of this paper.

In those cases where the target galaxy is close in velocity to H I emission from our Galaxy, each calibrator observation (primary and secondary) is split into two parts to form a pair of observations, one part having the velocity shifted by typically  $+300 \text{ km s}^{-1}$  and the other by  $-300 \text{ km s}^{-1}$  to avoid contamination by Galactic emission (the exact velocity offset depends on correlator configuration and systemic velocity of the object). This information is also listed in Table 2 (last column).

#### 3.2. Flagging of bad visibilities

The  $uv$ -data are inspected by eye for each configuration and bad data points due to either interference or cross-talk between antennae are removed (tasks TVFLG, UVFLG), after which the data are calibrated (CALIB, CLCAL). In some cases, to ensure proper calibration, solar interference on the shortest baselines had to be removed from the calibrator observations by deleting the affected baselines (in these cases short spacing information was still available from observations in other array configurations). We note though that most of the D-array observations were deliberately obtained during nighttime and were thus not affected by solar interference. After final editing, all data are combined to form a single dataset which was subsequently used for mapping (task DBCON).

<sup>7</sup> The Astronomical Image Processing System (AIPS) has been developed by the NRAO.

### 3.3. Continuum subtraction

In order to separate continuum from line emission we first determine the line-free channels in our observation and subsequently subtract the continuum emission in the  $uv$ -plane by fitting a first order polynomial to the line-free channels (task UVLIN). In a few cases, given the limitations of the current VLA correlator, only very few channels ( $\sim 5$ ) of line-free emission were available (but even in those cases the continuum subtraction worked satisfactorily). The line free channels were also used to create continuum maps of our galaxies. The quality of these continuum maps varies significantly from galaxy to galaxy (depending on the number of line-free channels). In general these maps have limited sensitivity and are therefore not presented here. For high sensitivity radio continuum images of the SINGS galaxies the reader is referred to Braun et al. (2007).

### 3.4. Mapping/Data cubes

After calibration and editing, datacubes are produced using the task IMAGR. For each galaxy, one data cube is calculated with natural weighting to obtain maps at the highest surface brightness sensitivity (hereafter referred to ‘NA cubes/maps’). A second cube is produced using the ROBUST weighting scheme (Briggs 1995) for every galaxy (‘RO cubes/maps’). With this scheme a data cube can be created with the sensitivity approaching that of natural weighting, but with a well-behaved synthesized beam at a resolution closer to that of uniform weighting ( $\sim 6''$ ). After experimenting with various ROBUST parameters we used a common parameter (ROBUST=0.5) for all galaxies. We typically cleaned down to a flux level of 2.5 times the noise level (no clean boxes were used).

Table 3 summarizes the final mapping parameters of the data cubes:

- column 1:** galaxy name
- column 2:** weighting scheme used. NA: Natural, RO: Robust=0.5 weighting
- column 3/4:** major and minor axis of synthesized beam in arcseconds
- column 5:** position angle of synthesized beam in degrees (measured north to east)
- column 6:** noise in one channel map in mJy beam<sup>-1</sup>
- column 7:** image size in pixels
- column 8:** pixel size in arcseconds
- column 9:** number of channels in final data cube
- column 10:** channel width in km s<sup>-1</sup>.

Throughout the paper we give the noise in mJy beam<sup>-1</sup>. The noise in Kelvin can be calculated using the following equation:

$$T_B[K] = 6.07 \times 10^5 \times S[\text{Jy beam}^{-1}] / (\text{FWHM}_{\text{maj}}['' ] \times \text{FWHM}_{\text{min}}['' ]) \quad (1)$$

where  $\text{FWHM}_{\text{maj}}$  and  $\text{FWHM}_{\text{min}}$  are the major and minor axis of the beam in arcsec.

### 3.5. Flux densities

Obtaining the correct H I flux of each channel and hence the global H I profiles of our targets is not straightforward. As first pointed out by Jörsäter & van Moorsel (1995), fully cleaned maps do not exist and any cleaned map consists of the sum of two maps: one containing the restored clean components and the other the residual map. In the former, the unit is Jansky per clean beam area, and in the latter Jansky per dirty beam area. Usually, fluxes are determined on the combined map, assuming that the clean beam is the correct one for the entire map. In reality, the flux is calculated correctly only for the cleaned fraction of the map; for the residual map the flux is overestimated by a factor  $\epsilon = \Omega_{\text{dirty}} / \Omega_{\text{clean}}$  where  $\Omega_{\text{dirty}}$  and  $\Omega_{\text{clean}}$  are the dirty and clean beam sizes, respectively. This becomes an issue for extended objects, especially in the case of combined array data, like our THINGS datasets. For a full discussion on this topic see Jörsäter & van Moorsel (1995) and Walter & Brinks (1999). Following their prescriptions, the real flux of a channel map is given by:

$$G = \frac{D \times C}{D - R} \quad (2)$$

where  $C$  is the cleaned flux, and  $R$  and  $D$  are the ‘erroneous’ residual flux and the ‘erroneous’ dirty flux over the same area of a channel map, respectively. The AIPS task IMAGR allows one to correctly scale the residual image (i.e., the division by  $\epsilon$ ) so that the correct flux is obtained in the fully restored map. We have carefully compared the IMAGR results (using the parameters IMAGRPRM(5)=1, IMAGRPRM(6)=50, IMAGRPRM(7)=50, which determine the half-width of the box used to determine the dirty beam area) to the analytical expression given above and conclude that IMAGR correctly scales the residual maps.

We stress that this flux correction works only for those areas that contain real emission (defined by the master cube discussed below). It is important to note that the noise outside the regions containing emission is artificially decreased in the rescaled cubes as the fluxes in the residual map (which represent only noise in the areas that do not contain emission) have been scaled down using this technique.

In summary, there are two different sets of cubes that can be used for future analysis:

- ‘standard’ cube: this is the standard output from IMAGR with no flux correction which has uniform noise properties. This cube is used for all analysis that requires data selection that is based on the noise in the cubes.
- blanked, flux ‘rescaled’ cube: this cube contains only the regions with emission (the blanking procedure is described in the next sub-section), i.e. it does not contain regions with no emission (noise). The HI fluxes in these channel maps are correct and these cubes have been used in the creation of the moment maps described in the following.

### 3.6. Blanking the data cubes

To separate real emission from noise, we consider only those regions for further analysis which show emission in three consecutive channels above a set level ( $2\sigma$ ) in standard cubes that have been convolved to  $30''$  resolution.

These areas of genuine emission are stored as masks in a master cube. Using this cube as reference when calculating maps of the total HI surface brightness, velocity, and velocity dispersion has the advantage that the same regions are included when inspecting cubes at different resolutions and with different signal-to-noise ratios.

In the next step, we blank the areas that contain noise in our residual-rescaled data cubes (Sec. 3.5) using these master cubes (using the task `BLANK`). This way we make sure that only regions of genuine emission are considered. The moment maps were calculated using the task `XMOM`, by using all pixels in the blanked data cubes. As a last step, we correct the integrated HI map for primary beam attenuation using the task `PBCOR` (note that primary beam correction has no effect on the first and second moment maps).

### 3.7. HI Spectra and HI Masses

To create global HI profiles (spectra) for each individual galaxy we calculated the HI flux in each channel map in the residual flux scaled NA data cube (after blanking and correction for primary beam attenuation) for each galaxy and plot the resulting spectra in Fig. 1. The HI spectra show a wealth of properties: the dwarfs show narrow and faint emission (given their low dynamical masses and low HI contents); their spectra can be approximated by Gaussian functions. The spirals on the other hand show broad and bright line emission. Some profiles show the typical double-horned profile indicative of flat rotation curves. The individual HI spectra of the THINGS sample are given in Fig. 1 and Table 4 (only one example galaxy is printed here, the tables for all other galaxies are available in the online version of the Journal). These spectra were also used to determine the central velocity of the individual galaxies that are listed in Table 5. This central value was obtained by taking the average velocity of those velocities corresponding to the 20% peak level on each side of the spectrum. Table 5 also lists the velocity widths at 50% and 20% of the peak level. A typical uncertainty for the both central velocities and the velocity widths is the width of one channel (as summarized in Tab. 2).

The total HI fluxes in units of  $\text{Jy km s}^{-1}$  and  $M_{\odot}$  are listed in Table 5 and their errors are dominated by uncertainties in the flux calibration (see Sec. 3.1). The HI masses have been calculated from the total fluxes using:

$$M_{\text{HI}}[M_{\odot}] = 2.36 \times 10^5 D^2 \times \sum_i S_i \Delta v \quad (3)$$

where  $\sum_i (S_i \Delta v)$  is the summation over the total emission in each channel in units of  $\text{Jy km s}^{-1}$  and  $D$  is the distance to the source in Mpc. This assumes that the HI is optically thin. If there were significant self-absorption, this would cause the derived HI masses to be underestimated. As Zwaan et al. (1997) argue that the flux correction due to self absorption is around 10% (in a statistical sample) and given the fact that most of our objects are seen at low inclinations, we did not attempt to correct for any (unknown) optical depth effects.

Although our data have not been corrected for potentially missing short spacings we note that our D-array observations are sensitive to emission up to spatial scales of  $15'$ . For comparison, we also summarize single dish

fluxes (compiled from various measurements available in the literature by Paturel et al. 2003) in Table 5 (column 4). We also compare our fluxes to the study by Fisher & Tully 1981 as there is a significant overlap between our sample and their study. A comparison shows that our fluxes are broadly in agreement with the published ones. As the single dish fluxes from Paturel et al. 2003 have been compiled from a variety of sources, we consider this agreement satisfactory. The only cases where our fluxes are considerably lower (by a factor 2 or more) than the single dish measurements are those galaxies which are more extended than our primary beam (i.e. the area mapped by us). In Tab. 5 we also compare our central velocities and velocity widths to those obtained by Fisher & Tully (1981) and find excellent agreement between the two studies.

## 4. THINGS DATA PRODUCTS

In the following we present the HI data cubes (channel maps), the integrated HI maps (moment 0), the velocity fields (moment 1) and the dispersion maps (moment 2) for each of the THINGS galaxies. All these THINGS data products (natural and robust weighting) are made publicly available at <http://www.mpia.de/THINGS>.

### 4.1. Channel maps

Every even-numbered figure (Figs 2, 4, ...68) shows the channel maps for each of the THINGS targets. To save space, not every single channel map is shown (see figure caption for details). In order to show the noise structure in the individual channels, the non-blanked (and non-rescaled) cubes are shown. To emphasize extended structure, the channel maps derived from the NA data cubes are presented; the greyscale represents the HI intensity on a linear scale (given in the caption). The central velocities for each channel map are given in the top right corner and the channel width is given in the caption. In general, a lot of complex fine-scale structure is visible in the individual channel maps; most of this information is lost when adding the channel maps together to create the integrated HI maps (moment 0). The following page shows the moment maps created from the data cubes (as discussed in the following).

### 4.2. Integrated HI maps

The integrated HI maps (based on the NA data) are shown in the top left panel of every odd-numbered figure (Figs. 3, 5, ...69). For each galaxy we show the same area as in the corresponding channel maps. The integrated HI maps have been created from the blanked data cubes by integrating:

$$I_{\text{HI}} = \sum_i S_i \times \Delta v, \quad (4)$$

where  $i$  denotes the  $i$ -th channel,  $S_i$  is the emission in one channel map in  $\text{Jy beam}^{-1}$  and  $\Delta v$  is the velocity width of one channel. The resulting map has subsequently been corrected for primary beam attenuation. The units of the integrated HI map are  $\text{Jy beam}^{-1} \text{ km s}^{-1}$  which can be converted to column densities  $N_{\text{HI}}$  (in units of  $\text{cm}^{-2}$ ) using:

$$N_{\text{HI}} = 1.823 \times 10^{18} \times \sum_i T_{\text{B},i} \Delta v, \quad (5)$$

where  $T_{B,i} \Delta v$  is the velocity integrated surface brightness temperature in units of  $\text{K km s}^{-1}$  (see Eq. 1).

The HI is shown on a linear scale, and the range of HI intensities shown is given in the respective figure caption for reference. The beamsize is indicated in the lower left corner (see Table 3). Even though a lot of the fine structure seen in the channel maps is lost, these images still reveal detailed structure, mostly in the form of spiral arms and HI holes. In the top right panel of each figure we show an optical image of the same area for comparison (taken from the Digitized Sky Survey, plotted on a logarithmic scale).

#### 4.3. Velocity fields

The bottom left corner of the odd-numbered figures (Fig. 3, 5, ...69) shows the velocity field of each galaxy. The velocity field (first moment) was calculated from the blanked NA data cube by evaluating:

$$\langle v \rangle = \frac{\sum_i S_i \times v}{\sum_i S_i}, \quad (6)$$

i.e. the intensity-weighted average of the velocities. In the adopted colour scheme dark colour represents redshifted (receding) emission whereas lighter colour indicates blue-shifted (approaching) emission (both with respect to the systemic velocity). The thick black contour indicates the systemic velocity (given in the figure caption). The black and white contours thus show the approaching and receding iso-velocity contours at a fixed velocity interval (the interval is given in the figure captions). We note that the velocity fields presented here are created by applying equation 6 to all of the information present in the (blanked) data cubes (i.e., including material that may not be directly associated with the bulk of the galaxy's disk). Therefore, they can only give some first indication of the overall kinematics in the individual systems and should be treated with caution when attempting a detailed kinematical analysis. de Blok et al. (2008), Oh et al. (2008) and Trachternach et al. (2008) discuss in detail the various methods that need to be employed for a proper kinematical analysis of the THINGS galaxies.

#### 4.4. Velocity Dispersion maps

Finally, in the bottom right corner of the odd-numbered figures (Fig. 3, 5, ...69) we present the velocity dispersion (second moment) map for each galaxy calculated from:

$$\sigma = \sqrt{\frac{\sum_i S_i \times (v - \langle v \rangle)^2}{\sum_i S_i}}, \quad (7)$$

again based on the NA weighted data. Contours indicate iso-dispersion values (numbers are given in the respective figure captions) for the individual galaxies. Again we stress that all emission in the (blanked) data cubes was used to create the maps - in the case of tidal material in the field (which is usually located at velocities that are quite different from those in the galaxy's disk) this will lead to high apparent velocity dispersion

(second moment) values in the map which have no immediate physical meaning. For quiescent regions, the velocity dispersion is a measure of the turbulence of the ISM; however a more sophisticated analysis is needed to constrain the true velocity dispersions of the different phases along individual lines of sight.

## 5. SUMMARY

In this paper we have described the observations and data products of the THINGS project – “The HI Nearby Galaxy Survey”. THINGS is a large observational project executed at the NRAO Very Large Array (VLA) to obtain 21-cm HI observations of the highest quality (spatial resolution  $\sim 6''$ , velocity resolution  $\leq 5.2 \text{ km s}^{-1}$ ) of nearby galaxies. A key characteristic of the THINGS dataset is the homogeneous sensitivity as well as spatial and velocity resolution of the HI data which is at the limit of what can be achieved with the VLA for a significant sample of galaxies. The sample includes 34 objects at distances  $2 \lesssim D \lesssim 15 \text{ Mpc}$  (resulting in linear resolutions of  $\sim 100$  to  $500 \text{ pc}$ ). The objects cover a wide range of star formation rates ( $\sim 10^{-3}$  to  $6 M_{\odot} \text{ yr}^{-1}$ ), total HI masses  $M_{\text{HI}}$  ( $0.01$  to  $14 \times 10^9 M_{\odot}$ ), absolute luminosities  $M_{\text{B}}$  ( $-11.5$  to  $-21.7 \text{ mag}$ ) and metallicities ( $7.5$  to  $9.2$  in units of  $12 + \log(\text{O}/\text{H})$ ).

We have presented a detailed description of the sample selection, the observational requirements, and the setup of the individual observations. We have described the data reduction procedures in detail and presented an atlas of the THINGS data products. This atlas contains channel maps for each galaxy as well as the integrated HI (moment 0), velocity (moment 1) and velocity dispersion maps (moment 2). These THINGS data products enable investigations of key characteristics of the interstellar medium related to galaxy morphology, star formation and mass distribution across the Hubble sequence. The THINGS data products (cubes and moment maps) are available at <http://www.mpia.de/THINGS>. Accompanying THINGS papers address issues such as the small-scale structure of the ISM, the (dark) matter distribution in THINGS galaxies, and the processes leading to star formation.

E.B. gratefully acknowledges financial support through an EU Marie Curie International Reintegration Grant (Contract No. MIRG-CT-6-2005-013556). The work of W.J.G.d.B. is based upon research supported by the South African Research Chairs Initiative of the Department of Science and Technology and National Research Foundation. F.B. acknowledges support from the Deutsche Forschungsgemeinschaft (DFG) Priority Program 1177. The National Radio Astronomy Observatory is a facility of the National Science Foundation operated under cooperative agreement by Associated Universities, Inc. We have made use of the Extragalactic Database (NED), which is operated by the Jet Propulsion Laboratory, California Institute of Technology, under contract with the National Aeronautics and Space Administration. This research has also made use of NASA's Astrophysics Data System (ADS). We acknowledge the usage of the HyperLeda database (<http://leda.univ-lyon1.fr>).

## REFERENCES

- Begeman et al. 1987, PhD Thesis, University of Groningen
- Bigiel, F., Leroy, A., Walter, F., Brinks, E., de Blok, W.J.G., Madore, B., Thornley, M.D., 2008, AJ, in press
- Bosma, 1981a, AJ, 86, 1791
- Bosma, 1981b, AJ, 86, 1825
- Braun, R. 1995, A&AS, 114, 409
- Braun, R., 2007, A&A, 461, 455
- Briggs, D. 1995, Ph.D. thesis, New Mexico Institute of Mining and Technology
- Brinks, E. & Bajaja, E. 1986, A&A, 169, 14
- de Blok, W. J. G. & Walter, F. 2000, ApJL, 537, L95
- de Blok, W. J. G., McGaugh, S. S., Bosma, A., & Rubin, V. C. 2001a, ApJL, 552, L23
- de Blok, W. J. G., McGaugh, S. S., & Rubin, V. C. 2001b, AJ, 122, 2396
- de Blok, W. J. G., Walter, F., Brinks, E., Trachternach, C., Oh, S.-H., Kennicutt, R.C., 2008, AJ, in press
- Fisher, J. R., & Tully, R. B. 1981, ApJS, 47, 139
- Kamphuis, J., Sancisi, R., & van der Hulst, T. 1991, A&A, 244, L29
- Kennicutt, R. C., et al. 2003, PASP, 115, 928
- Kim, S., Dopita, M. A., Staveley-Smith, L., Bessell, M. S. 1999, AJ, 118, 2797
- Lee, J., 2007, PhD Thesis, University of Arizona
- Leroy, A., Walter, F., Brinks, E., Bigiel, F., de Blok, W. J. G., Madore, B., Thornlet, M.D., 2008, AJ, in press
- Moustakas, J., 2007, PhD Thesis, University of Arizona
- Oh, S.-H., de Blok, W. J. G., Walter, F., Brinks, E., Kennicutt, R. C., 2008, AJ, in press
- Ott, J., Walter, F., Brinks, E., Van Dyk, S. D., Dirsch, B., & Klein, U. 2001, AJ, 122, 3070
- Paturel, G., Theureau, G., Bottinelli, L., Gouguenheim, L., Coudreau-Durand, N., Hallet, N., Petit, C., 2003 A&A 412, 57
- Puche, D., Westpfahl, D., Brinks, E., & Roy, J. 1992, AJ, 103, 1841
- Rich, J., de Blok, W. J. G., Brinks, E., Walter, F., Bagetakos, I., Kennicutt, R.C., 2008, AJ, in press
- Staveley-Smith, L., Sault, R. J., Hatzidimitriou, D., Kesteven, M. J., & McConnell, D. 1997, MNRAS, 289, 225
- Swaters, R., A., van Albada, T.S., van der Hulst, J.M., Sancisi, R., 2002, A&A, 390, 829
- Tamburro, D., Rix, H.-W., Walter, F., Brinks, E., de Blok, W. J. G., Mac Low, M., 2008, AJ, in press
- Trachternach, C., de Blok, W.J.G., Walter, F., Brinks, E., Kennicutt, R. C., 2008, AJ, in press
- Usero, A., Brinks, E., et al., 2009, AJ, in prep.
- van de Hulst, H.C. 1945, Nederlandsch Tijdschrift voor Natuurkunde, 11, 210
- Verheijen, M. A. W., & Sancisi, R. 2001, A&A, 370, 765
- Walter, F., & Brinks, E. 1999, AJ, 118, 273
- Walter, F., & Brinks, E. 2001, AJ, 121, 3026
- Walter, F., Weiss, A., Martin, C., & Scoville, N. 2002, AJ, 123, 225
- Westpfahl, D. J., Coleman, P. H., Alexander, J., & Tongue, T. 1999, AJ, 117, 868
- Zwaan, M. A., Briggs, F. H., Sprayberry, D., Sorar, E., 1997, ApJ 490, 173
- Zwaan, M., Ryan-Weber, E., Walter, F., Brinks, E., de Blok, W. J. G., Kennicutt, R. C., 2008, AJ, in press

TABLE 1  
 PROPERTIES OF THINGS SAMPLE GALAXIES.

1	2	3	4	5	6	7	8	9	10	11	12	13	14
Galaxy	alt. name	RA(2000.0) hh mm ss.s	Dec(2000.0) dd mm ss.s	$D$ Mpc	$\log(D_{25})$ $\log(0.1')$	$m_B$ mag	$M_B$ mag	Incl °	P.A. °	Metal. 12+log(O/H)	SFR $M_\odot \text{ yr}^{-1}$	Type —	Notes —
NGC 628	M 74, UGC 1149	01 36 41.8	+15 47 00	7.3 [K04]	1.99	9.35	-19.97	7	20 [T08]	8.33 [M08]	1.21 [L08]	5	
NGC 925	UGC 1913	02 27 16.5 [T08]	+33 34 44	9.2 [F01]	2.03	9.77	-20.04	66	287 [dB08]	8.24 [M08]	1.09 [L08]	7	
NGC 1569	UGC 3056	04 30 49.0	+64 50 53	2.0 [K04]	1.60	8.33	-18.12	63	112 [M05]	8.16 [S89]	0.06 [K98]	10	
NGC 2366	UGC 2366	07 28 53.4 [O08]	+69 12 51	3.4 [H01]	1.64	10.51	-17.17	64	40 [O08]	7.96 [S89]	—	10	B
NGC 2403	UGC 3918	07 36 51.1 [T08]	+65 36 03	3.2 [F01]	2.20	8.11	-19.43	63	124 [dB08]	8.31 [M08]	0.85 [L08]	6	B
Ho II	UGC 4305	08 19 05.0	+70 43 12	3.4 [K04]	1.82	10.78	-16.87	41	177 [P92]	7.68 [M08]	0.07 [L08]	10	W
M81 DwA		08 23 56.0	+71 01 45	3.6 [K04]	1.1*	16.26	-11.49	23	49 [B06]	—	—	10	
DDO 53	UGC 4459	08 34 07.2	+66 10 54	3.6 [K04]	0.89	14.31	-13.45	31	132 [B06]	7.77 [M08]	0.008 [L08]	10	
NGC 2841	UGC 4966	09 22 02.6 [T08]	+50 58 35	14.1 [M01]	1.84	9.54	-21.21	74	153 [dB08]	8.52 [M08]	0.20 [K03]	3	
NGC 2903	UGC 5079	09 32 10.1 [T08]	+21 30 04	8.9 [D00]	2.07	8.82	-20.93	65	204 [dB08]	9.12 [Z94]	—	4	W
Ho I	UGC 5139	09 40 32.3	+71 10 56	3.8 [K04]	1.52	13.12	-14.80	12	50 [O01]	7.54 [M08]	0.006 [L08]	10	
NGC 2976	UGC 5221	09 47 15.3 [T08]	+67 55 00	3.6 [K02]	1.86	9.98	-17.78	65	335 [dB08]	8.30 [M08]	0.10 [L08]	5	
NGC 3031	M 81, UGC 5318	09 55 33.1 [T08]	+69 03 55	3.6 [F01]	2.33	7.07	-20.73	59	330 [dB08]	8.41 [M08]	1.06 [L08]	2	B
NGC 3077	UGC 5398	10 03 19.1	+68 44 02	3.8 [K04]	1.73	10.16	-17.75	46	45	8.64 [S94]	0.09 [K98]	10	
M81 DwB	UGC 5423	10 05 30.6	+70 21 52	5.3 [K04]	1.05	14.39	-14.23	44	321	7.85 [M08]	0.005 [L08]	10	
NGC 3184	UGC 5557	10 18 17.0	+41 25 28	11.1 [L02]	1.87	10.31	-19.92	16	179 [T08]	8.48 [M08]	1.43 [L08]	6	W
NGC 3198	UGC 5572	10 19 55.0 [T08]	+45 32 59	13.8 [F01]	1.81	9.95	-20.75	72	215 [dB08]	8.32 [M08]	0.85 [K03]	5	
IC 2574	UGC 5666	10 28 27.7 [O08]	+68 24 59	4.0 [K02]	2.11	9.91	-18.11	53	56 [O08]	7.94 [M08]	0.12 [L08]	9	
NGC 3351	M 95, UGC 5850	10 43 57.7	+11 42 14	10.1 [K04]	1.86	10.13	-19.88	41	192 [T08]	8.60 [M08]	0.71 [L08]	3	
NGC 3521	UGC 6150	11 05 48.6 [T08]	-00 02 09	10.7 [vflow]	1.92	9.21	-20.94	73	340 [dB08]	8.36 [M08]	3.34 [L08]	4	
NGC 3621		11 18 16.5 [T08]	-32 48 51	6.6 [F01]	1.99	9.06	-20.05	65	345 [dB08]	8.24 [M08]	2.09 [L08]	7	
NGC 3627	M 66, UGC 6346	11 20 15.0 [T08]	+12 59 30	9.3 [F01]	2.01	9.09	-20.74	62	173 [dB08]	8.43 [M08]	2.44 [L08]	3	
NGC 4214	UGC 7278	12 15 39.2	+36 19 37	2.9 [K04]	1.83	9.91	-17.43	44	65	8.34 [S89]	0.05 [K98]	10	W
NGC 4449	UGC 7592	12 28 11.9	+44 05 40	4.2 [K04]	1.67	8.98	-19.14	60	230 [H98]	8.32 [S89]	—	10	W
NGC 4736	M 94, UGC 7996	12 50 53.0 [T08]	+41 07 13	4.7 [K04]	1.89	8.54	-19.80	41	296 [dB08]	8.31 [M08]	0.43 [L08]	2	B
DDO 154	UGC 8024	12 54 05.9 [T08]	+27 09 10	4.3 [K04]	1.29	13.94	-14.23	66	230 [dB08]	7.54 [M08]	0.004 [L08]	10	
NGC 4826	M 64, UGC 8062	12 56 43.6 [T08]	+21 41 00	7.5 [K04]	2.02	8.74	-20.63	65	121 [dB08]	8.59 [M08]	0.82 [L08]	2	B
NGC 5055	M 63, UGC 8334	13 15 49.2 [T08]	+42 01 45	10.1 [vflow]	2.07	8.90	-21.12	59	102 [dB08]	8.42 [M08]	2.42 [L08]	4	
NGC 5194	M 51a, UGC 8493	13 29 52.7	+47 11 43	8.0 [K04]	1.89	8.48	-21.04	42	172 [T08]	8.54 [M08]	6.05 [L08]	4	
NGC 5236	M 83	13 37 00.9	-29 51 57	4.5 [K04]	2.19	7.48	-20.77	24	225 [T93]	9.16 [Z94]	2.52 [K98]	5	
NGC 5457	M 101, UGC 8981	14 03 12.6	+54 20 57	7.4 [K04]	2.38	8.29	-21.05	18	39 [B81]	8.52 [Z94]	2.49 [K98]	6	B
NGC 6946	UGC 11597	20 34 52.2 [T08]	+60 09 14	5.9 [K04]	2.06	8.24	-20.61	33	243 [dB08]	8.40 [M08]	4.76 [L08]	6	
NGC 7331	UGC 12113	22 37 04.1 [T08]	+34 24 57	14.7 [F01]	1.96	9.17	-21.67	76	168 [dB08]	8.36 [M08]	4.20 [K03]	3	
NGC 7793		23 57 49.7 [T08]	-32 35 28	3.9 [K04]	2.02	9.17	-18.79	50	290 [dB08]	8.22 [M08]	0.51 [L08]	7	B

NOTE. — Comments on columns:

column 1: galaxy name

column 2: alternative names (UGC and Messier catalogs)

column 3/4: Coordinates in J2000.0. No entry: coordinates taken from NED; T08: Trachternach et al. 2008

column 5: distances in Mpc. vflow: distances calculated from NED using Hubble flow distances (corrected for Virgo infall); dB08: de Blok et al. 2008, O08: Oh et al. 2008, K02: Karachentsev et al. 2002, K04: Karachentsev et al. 2004, H01: Hunter et al. 2001, F01: Freedman et al. 2001, L02: Leonard et al. 2002, M01: Macri et al. 2001, D00: Drozdovsky & Karachentsev 2000

column 6: optical size (taken from LEDA, LEDA.UNIV-LYON.FR); K04: Karachentsev et al. 2004; Note: Holmberg diameter is given for M81 dwA

column 7: apparent blue magnitude, corrected for Galactic foreground extinction and extinction internal to the galaxy from LEDA; B06: Begum et al. 2006

column 8: absolute B magnitude derived from columns 7 and 4

column 9/10: Inclination and position angle; No entry: taken from LEDA, dB08: de Blok et al. 2008, B06: Begum et al. 2006, O01: Ott et al. 2001, P92: Puche et al. 1992, O08: Oh et al. 2008, M05: Mühlle et al. 2005, T08: Tamburro et al. 2008, H98: Hunter et al. 1998, T93: Tilanus & Allen 1993, B81: Bosma et al. 1981

column 11: metallicities. M08: Moustakas et al. 2008, S89: Skillman et al. 1989, Z94: Zaritzky et al. 1994, S94: Storch et al. 1994

column 12: Star formation rates. Derived from fluxes published in the literature and corrected for our adopted distances: L08: Lee et al. 2008, K98: Kennicutt 1998, K03: Kennicutt et al. 2003

column 13: Morphological type from LEDA

column 14: Notes: W: WHISP target (e.g. Swaters et al. 2002), B: target studied by Braun (1995).



TABLE 2  
SUMMARY OF THINGS OBSERVING SETUPS.

1	2	3	4	5	6	7	8	9	10	11	12	13	14	15	16	17	18
Name	Conf.	Project	Date yy-mm-dd	Start	End	Dur.	cal.	Flux Jy	RA hh mm ss	DEC dd mm ss	mode	BW MHz	chan #	$\Delta V$ km s <sup>-1</sup>	equ.	Vhel1 km s <sup>-1</sup>	Vhel2 km s <sup>-1</sup>
NGC 628	B	AW605	2005-04-02	16 45	00 15	7 00	0202+149	3.578±0.003	01 34 01.00	15 31 55.0	2AD	1.56	128	2.6	1950	655.353	...
NGC 628	C	AW605	2004-02-22	20 45	23 00	2 00	0202+149	3.745±0.003	01 34 01.00	15 31 55.0	2AD	1.56	128	2.6	1950	655.353	...
NGC 628	D	AW605	2004-07-05	16 30	18 15	1 15	0202+149	3.717±0.006	01 34 01.00	15 31 55.0	2AD	1.56	128	2.6	1950	655.353	...
NGC 925	B	AW605	2004-01-08	22 45	05 45	6 00	0234+285	2.075±0.008	02 24 16.90	33 21 19.0	2AD	1.56	128	2.6	1950	565.0	...
NGC 925	C	AW430	1996-04-27	22 30	01 30	2 15	0234+285	2.288±0.007	02 24 16.90	33 21 19.0	2AD	1.56	128	2.6	1950	565.0	...
NGC 925	C	AW430	1996-04-28	23 30	01 15	2 15	0234+285	2.301±0.006	02 24 16.90	33 21 19.0	2AD	1.56	128	2.6	1950	565.0	...
NGC 925	D	AW436	1996-08-30	14 45	15 30	0 30	0234+285	2.266±0.005	02 24 16.90	33 21 19.0	2AD	1.56	128	2.6	1950	565.0	...
NGC 1569	B	AW605	2003-11-10	05 00	12 30	6 00	0404+768	5.507±0.003	04 26 06.00	64 44 18.0	2AD	1.56	128	2.6	1950	-90.0	...
NGC 1569	C	AW325	1993-06-29	11 45	19 15	5 00	0614+607	1.223±0.001	04 26 06.00	64 44 18.0	2AD	1.56	128	2.6	1950	-90.0	...
NGC 1569	D	AW325	1992-09-06	08 00	12 00	2 30	0614+607	1.181±0.004	04 26 06.00	64 44 18.0	2AD	1.56	128	2.6	1950	-90.0	...
NGC 2366	B	AW605	2003-12-03	06 00	13 30	5 30	0614+607	1.120±0.001	07 28 54.86	69 12 56.6	2AD	1.56	128	2.6	2000	100.0	...
NGC 2366	C	AW605	2004-02-23	02 00	07 45	2 00	0614+607	1.166±0.001	07 28 54.86	69 12 56.6	2AD	1.56	128	2.6	2000	100.0	...
NGC 2366	D	AW605	2004-07-02	17 30	20 00	1 30	0614+607	1.151±0.003	07 28 54.86	69 12 56.6	2AD	1.56	128	2.6	2000	100.0	...
NGC 2403	B	AW605	2003-12-10	05 30	13 00	6 00	0831+557	8.111±0.011	07 32 01.20	65 42 57.0	4	1.56	64	5.2	1950	252.536	4.986
NGC 2403	C	AW605	2004-02-22	23 15	02 00	2 00	0831+557	8.146±0.020	07 32 01.20	65 42 57.0	4	1.56	64	5.2	1950	252.536	4.986
NGC 2403	D	AW605	2004-07-05	18 15	20 15	1 15	0831+557	8.206±0.009	07 32 01.20	65 42 57.0	4	1.56	64	5.2	1950	252.536	4.986
HoII	B	AP196	1990-08-10	15 30	23 30	5 30	0859+681	0.614±0.002	08 14 06.00	70 52 00.0	2AD	1.56	128	2.6	1950	190.0	...
HoII	C	AP196	1990-12-02	10 00	16 00	2 15	0836+710	3.727±0.004	08 14 06.00	70 52 00.0	2AD	1.56	128	2.6	1950	190.0	...
HoII	D	AP196	1991-03-07	05 15	10 15	1 45	0836+710	3.729±0.007	08 14 06.00	70 52 00.0	2AD	1.56	128	2.6	1950	190.0	...
M81 dwA	B	AW605	2003-12-16	06 00	13 30	5 45	0921+622	1.091±0.002	08 23 56.00	71 01 45.0	2AD	0.78	128	1.3	2000	113.0	...
M81 dwA	C	AT285	2002-11-03	10 30	13 45	2 15	0841+708	3.324±0.002	08 23 56.00	71 01 45.0	2AD	0.78	128	1.3	2000	113.0	...
M81 dwA	D	AH752	2001-12-10	07 00	11 00	3 15	0841+708	3.330±0.007	08 23 56.00	71 01 45.0	2AD	0.78	128	1.3	2000	113.0	...
DDO 53	B	AW605	2003-12-22	06 15	13 30	6 00	0834+555	8.122±0.014	08 34 08.77	66 11 32.0	2AD	1.56	128	2.6	2000	20.0	...
DDO 53	C	AW605	2004-02-23	02 00	07 45	2 00	0834+555	8.155±0.011	08 34 08.77	66 11 32.0	2AD	1.56	128	2.6	2000	20.0	...
DDO 53	D	AW605	2004-07-09	19 00	21 30	1 30	0834+555	8.235±0.013	08 34 08.77	66 11 32.0	2AD	1.56	128	2.6	2000	20.0	...
NGC 2841	B	AW605	2003-12-30	06 15	13 30	3 00	0834+555	8.074±0.024	09 22 02.00	50 58 35.0	4	1.56	64	5.2	2000	1011.049	762.246
NGC 2841	B	AW605	2003-12-30	06 15	13 30	3 00	0834+555	8.060±0.030	09 22 02.00	50 58 35.0	4	1.56	64	5.2	2000	513.855	265.874
NGC 2841	B	AW605	2005-05-22	21 15	01 00	1 15	0834+555	8.047±0.025	09 22 02.00	50 58 35.0	4	1.56	64	5.2	2000	1011.049	762.246
NGC 2841	B	AW605	2005-05-22	21 15	01 00	1 15	0834+555	8.043±0.005	09 22 02.00	50 58 35.0	4	1.56	64	5.2	2000	513.855	265.874
NGC 2841	B	AW605	2005-05-23	21 15	01 00	1 15	0834+555	8.047±0.025	09 22 02.00	50 58 35.0	4	1.56	64	5.2	2000	1011.049	762.246
NGC 2841	B	AW605	2005-05-23	21 15	01 00	1 15	0834+555	8.043±0.005	09 22 02.00	50 58 35.0	4	1.56	64	5.2	2000	513.855	265.874
NGC 2841	C	AW605	2004-02-29	03 15	10 30	3 00	0834+555	8.132±0.014	09 22 02.00	50 58 35.0	4	1.56	64	5.2	2000	1011.049	762.246
NGC 2841	C	AW605	2004-02-29	03 15	10 30	3 00	0834+555	8.131±0.014	09 22 02.00	50 58 35.0	4	1.56	64	5.2	2000	513.855	265.874
NGC 2841	D	AW605	2004-07-05	20 15	00 15	1 30	0834+555	8.145±0.023	09 22 02.00	50 58 35.0	4	1.56	64	5.2	2000	1011.049	762.246
NGC 2841	D	AW605	2004-07-05	20 15	00 15	1 30	0834+555	8.223±0.013	09 22 02.00	50 58 35.0	4	1.56	64	5.2	2000	513.855	265.874
NGC 2903	B	AW605	2005-04-16	22 30	05 30	6 00	0854+201	1.347±0.013	09 32 10.00	21 30 02.0	4	1.56	64	5.2	2000	680.179	431.923
NGC 2903	C	AW605	2004-04-27	22 30	08 00	2 30	0854+201	1.534±0.003	09 32 10.00	21 30 02.0	4	1.56	64	5.2	2000	680.179	431.923
NGC 2903	D	AW605	2004-07-02	21 30	03 00	1 15	0842+185	1.187±0.003	09 32 10.00	21 30 02.0	4	1.56	64	5.2	2000	680.179	431.923
HoI	B	AP196	1990-07-23	20 45	04 30	6 00	0917+624	1.209±0.003	09 36 00.00	71 24 47.0	2AD	1.56	128	2.6	1950	190.0	...
HoI	C	AP196	1990-12-02	10 00	16 00	2 15	0836+710	3.727±0.004	09 36 00.00	71 24 47.0	2AD	1.56	128	2.6	1950	190.0	...
HoI	D	AP196	1991-03-07	05 15	10 15	1 45	0836+710	3.729±0.007	09 36 00.00	71 24 47.0	2AD	1.56	128	2.6	1950	190.0	...
NGC 2976	B	AB1038	2002-08-23	15 00	03 00	10 30	0921+622	1.152±0.004	09 47 15.30	67 55 00.0	4AC	1.56	64	5.2	2000	3.0	...
NGC 2976	C	AB1038	2002-12-16	07 30	11 30	03 15	0921+622	1.112±0.003	09 47 15.30	67 55 00.0	4AC	1.56	64	5.2	2000	3.0	...
NGC 2976	D	AB1038	2003-05-10	02 30	04 15	01 30	0921+622	1.203±0.009	09 47 15.30	67 55 00.0	4AC	1.56	64	5.2	2000	3.0	...

THINGS

The HI

Nearby Gal

SP

SP

SP

SP

SP

SP

SP

SP

TABLE 2  
 SUMMARY OF THINGS OBSERVING SETUPS.

1	2	3	4	5	6	7	8	9	10	11	12	13	14	15	16	17	18
Name	Conf.	Project	Date	Start	End	Dur.	cal.	Flux	RA	DEC	mode	BW	chan	$\Delta V$	equ.	Vhel1	Vhel2
			yy-mm-dd					Jy	hh mm ss	dd mm ss		MHz	#	km s <sup>-1</sup>		km s <sup>-1</sup>	km s <sup>-1</sup>
NGC 3031	B	AW343	1993-02-28	02 30	10 30	2 45	0917+624	1.106±0.002	09 50 49.00	69 24 20.0	2AD	1.56	128	2.6	1950	40.0	...
NGC 3031	B	AW343	1993-02-28	02 30	10 30	2 45	0917+624	1.097±0.002	09 52 07.00	69 12 00.0	2AD	1.56	128	2.6	1950	-125.0	...
NGC 3031	B	AW343	1993-03-05	03 30	09 00	2 00	0917+624	1.052±0.007	09 50 49.00	69 24 20.0	2AD	1.56	128	2.6	1950	40.0	...
NGC 3031	B	AW343	1993-03-05	03 30	09 00	2 00	0917+624	1.050±0.007	09 52 07.00	69 12 00.0	2AD	1.56	128	2.6	1950	-125.0	...
NGC 3031	B	AW343	1993-03-06	01 30	10 30	3 15	0917+624	1.041±0.002	09 50 49.00	69 24 20.0	2AD	1.56	128	2.6	1950	40.0	...
NGC 3031	B	AW343	1993-03-06	01 30	10 30	3 15	0917+624	1.035±0.002	09 52 07.00	69 12 00.0	2AD	1.56	128	2.6	1950	-125.0	...
NGC 3031	C	AW326	1993-07-03	16 45	05 00	3 45	0836+710	3.585±0.004	09 50 49.00	69 24 20.0	2AD	1.56	128	2.6	1950	40.0	...
NGC 3031	C	AW326	1993-07-03	16 45	05 00	3 45	0836+710	3.568±0.004	09 52 07.00	69 12 00.0	2AD	1.56	128	2.6	1950	-125.0	...
NGC 3031	C	AW326	1993-07-04	16 45	05 00	3 45	0836+710	3.592±0.005	09 50 49.00	69 24 20.0	2AD	1.56	128	2.6	1950	40.0	...
NGC 3031	C	AW326	1993-07-04	16 45	05 00	3 45	0836+710	3.580±0.004	09 52 07.00	69 12 00.0	2AD	1.56	128	2.6	1950	-125.0	...
NGC 3031	D	AW326	1992-08-23	13 45	22 30	3 00	0836+710	3.684±0.009	09 50 49.00	69 24 20.0	2AD	1.56	128	2.6	1950	40.0	...
NGC 3031	D	AW326	1992-08-23	13 45	22 30	3 00	0836+710	3.681±0.010	09 52 07.00	69 12 00.0	2AD	1.56	128	2.6	1950	-125.0	...
NGC 3077	B	AP217	1992-01-09	06 00	14 00	6 00	0917+624	1.060±0.002	09 59 21.50	68 58 32.0	2AD	1.56	128	2.6	1950	-20.0	...
NGC 3077	C	AP217	1992-04-27	23 15	07 00	2 15	0917+624	1.147±0.004	09 59 21.50	68 58 32.0	2AD	1.56	128	2.6	1950	-20.0	...
NGC 3077	D	AP217	1992-09-03	13 15	19 15	1 45	0917+624	1.054±0.009	09 59 21.50	68 58 32.0	2AD	1.56	128	2.6	1950	-20.0	...
M81 dwB	B	AW605	2005-04-29	22 45	06 00	6 15	0921+622	0.854±0.003	10 05 30.60	70 21 52.0	2AD	1.56	128	2.6	2000	350.0	...
M81 dwB	C	AT285	2002-11-03	13 45	17 15	2 15	0841+708	3.348±0.007	10 05 30.60	70 21 52.0	2AD	1.56	128	2.6	2000	350.0	...
M81 dwB	D	AW605	2004-07-09	19 00	21 00	1 30	0841+708	3.304±0.011	10 05 30.60	70 21 52.0	2AD	1.56	128	2.6	2000	350.0	...
NGC 3184	B	AW555	2001-05-25	22 00	05 45	6 00	1013+347	0.461	10 18 16.90	41 25 28.0	2AD	1.56	128	2.6	2000	592.0	...
NGC 3184	B	AW605	2004-01-07	06 30	13 15	6 00	1006+349	3.157±0.007	10 18 16.90	41 25 28.0	2AD	1.56	128	2.6	2000	592.0	...
NGC 3184	C	AW588	2005-04-07	10 30	18 00	6 00	0958+324	1.558±0.003	10 18 16.90	41 25 28.0	2AD	1.56	128	2.6	2000	592.0	...
NGC 3184	D	AW605	2004-07-02	23 30	01 15	1 30	0958+324	1.704±0.006	10 18 16.90	41 25 28.0	2AD	1.56	128	2.6	2000	592.0	...
NGC 3198	B	AW605	2005-04-26	23 30	07 15	6 45	1035+564	1.771±0.004	10 19 54.90	45 32 59.0	4	1.56	64	5.2	2000	549.178	782.087
NGC 3198	C	AT285	2002-11-16	12 30	13 00	0 15	1006+349	3.142±0.008	10 19 54.90	45 32 59.0	4	1.56	64	5.2	2000	549.178	782.087
NGC 3198	C	AT285	2002-11-19	11 15	12 30	0 45	1006+349	3.155±0.006	10 19 54.90	45 32 59.0	4	1.56	64	5.2	2000	549.178	782.087
NGC 3198	C	AT285	2003-01-07	10 30	13 45	2 15	1006+349	3.182±0.004	10 19 54.90	45 32 59.0	4	1.56	64	5.2	2000	549.178	782.087
NGC 3198	D	AT285	2003-03-27	06 30	06 45	0 15	1006+349	3.171±0.007	10 19 54.90	45 32 59.0	4	1.56	64	5.2	2000	549.178	782.087
NGC 3198	D	AT285	2003-04-28	04 15	04 30	0 15	1006+349	3.170±0.008	10 19 54.90	45 32 59.0	4	1.56	64	5.2	2000	549.178	782.087
NGC 3198	D	AW605	2004-07-09	21 30	23 00	1 30	1035+564	1.750±0.006	10 19 54.90	45 32 59.0	4	1.56	64	5.2	2000	549.178	782.087
IC 2574	B	AP217	1992-01-18	05 30	13 15	5 30	1031+567	1.811±0.002	10 24 48.00	68 40 00.0	2AD	1.56	128	2.6	1950	38.0	...
IC 2574	B	AP217	1992-01-19	05 30	13 15	5 30	1031+567	1.811±0.002	10 24 48.00	68 40 00.0	2AD	1.56	128	2.6	1950	38.0	...
IC 2574	C	AP217	1992-04-27	23 15	07 00	2 15	1031+567	1.815±0.004	10 24 48.00	68 40 00.0	2AD	1.56	128	2.6	1950	38.0	...
IC 2574	D	TEST03	1991-03-03	08 30	13 30	2 30	0945+664	2.217±0.003	10 24 48.00	68 40 00.0	2AD	1.56	128	2.6	1950	38.0	...
IC 2574	D	AP217	1992-09-03	13 15	19 15	1 45	1031+567	1.802±0.005	10 24 48.00	68 40 00.0	2AD	1.56	128	2.6	1950	38.0	...
NGC 3351	B	AW605	2004-01-06	08 00	15 00	6 00	1120+143	2.398±0.007	10 43 57.99	11 42 14.3	4	1.56	64	5.2	2000	681.601	893.980
NGC 3351	C	AT285	2002-11-10	12 45	16 00	1 45	1042+120	3.227±0.008	10 43 57.99	11 42 14.3	4	1.56	64	5.2	2000	681.601	893.980
NGC 3351	D	AW605	2004-07-09	23 00	01 00	1 30	1120+143	2.408±0.007	10 43 57.99	11 42 14.3	4	1.56	64	5.2	2000	681.601	893.980
NGC 3521	B	AW605	2005-04-01	03 00	09 45	3 00	1119-030	1.639±0.003	11 05 48.00	-00 02 15.0	4	1.56	64	5.2	2000	1178.464	929.385
NGC 3521	B	AW605	2005-04-01	03 00	09 45	3 00	1119-030	1.630±0.003	11 05 48.00	-00 02 15.0	4	1.56	64	5.2	2000	680.718	432.461
NGC 3521	B	AW605	2005-04-26	01 15	08 00	3 00	1119-030	1.642±0.004	11 05 48.00	-00 02 15.0	4	1.56	64	5.2	2000	1178.464	929.385
NGC 3521	B	AW605	2005-04-26	01 15	08 00	3 00	1119-030	1.630±0.003	11 05 48.00	-00 02 15.0	4	1.56	64	5.2	2000	680.718	432.461
NGC 3521	C	AW605	2004-03-04	05 15	10 30	2 00	1119-030	1.634±0.006	11 05 48.00	-00 02 15.0	4	1.56	64	5.2	2000	1178.464	929.385
NGC 3521	C	AW605	2004-03-04	05 15	10 30	2 00	1119-030	1.631±0.005	11 05 48.00	-00 02 15.0	4	1.56	64	5.2	2000	680.718	432.461
NGC 3521	DnC	AW605	2004-06-01	23 15	01 45	1 00	1119-030	1.653±0.003	11 05 48.00	-00 02 15.0	4	1.56	64	5.2	2000	1178.464	929.385
NGC 3521	DnC	AW605	2004-06-01	23 15	01 45	1 00	1119-030	1.637±0.006	11 05 48.00	-00 02 15.0	4	1.56	64	5.2	2000	680.718	432.461
NGC 3521	D	AW605	2004-07-09	21 00	00 45	1 30	1119-030	1.619±0.005	11 05 48.00	-00 02 15.0	4	1.56	64	5.2	2000	1178.464	929.385
NGC 3521	D	AW605	2004-07-09	21 00	00 45	1 30	1119-030	1.605±0.003	11 05 48.00	-00 02 15.0	4	1.56	64	5.2	2000	680.718	432.461
NGC 3621	BnA	AW605	2003-10-03	03 00	09 45	6 00	1120-251	1.749±0.008	11:18:16.20	-32 48 49.9	4	1.56	64	5.2	2000	633.047	845.357
NGC 3621	CnB	AT285	2002-09-22	16 15	20 15	3 00	1154-350	6.122±0.014	11:18:16.17	-32 48 49.9	4	1.56	64	5.2	2000	633.047	845.357
NGC 3621	DnC	AT285	2003-01-31	10 15	10 45	0 15	1154-350	6.165±0.014	11:18:16.17	-32 48 49.9	4	1.56	64	5.2	2000	633.047	845.357
NGC 3621	DnC	AW605	2004-06-04	00 00	04 00	1 15	1154-350	6.219±0.035	11:18:16.20	-32 48 49.9	4	1.56	64	5.2	2000	633.047	845.357

TABLE 2  
SUMMARY OF THINGS OBSERVING SETUPS.

1	2	3	4	5	6	7	8	9	10	11	12	13	14	15	16	17	18
Name	Conf.	Project	Date	Start	End	Dur.	cal.	Flux	RA	DEC	mode	BW	chan	$\Delta V$	equ.	Vhel1	Vhel2
			yy-mm-dd					Jy	hh mm ss	dd mm ss		MHz	#	km s <sup>-1</sup>		km s <sup>-1</sup>	km s <sup>-1</sup>
NGC 3627	B	AW605	2005-05-28	22 00	04 30	6 15	1120+143	2.393±0.009	11 20 15.02	12 59 29.5	4	1.56	64	5.2	2000	849.257	600.723
NGC 3627	C	AW605	2004-03-11	05 15	06 30	1 00	1120+143	2.385±0.010	11 20 15.02	12 59 29.5	4	1.56	64	5.2	2000	849.257	600.723
NGC 3627	C	AW605	2004-03-11	06 30	09 30	0 45	1120+143	2.394±0.006	11 20 15.02	12 59 29.5	4	1.56	64	5.2	2000	849.257	600.723
NGC 3627	DnC	AW605	2004-06-12	23 00	01 00	1 45	1120+143	2.386±0.005	11 20 15.02	12 59 29.5	4	1.56	64	5.2	2000	849.257	600.723
NGC 3627	D	AS750	2003-03-22	04 15	08 15	2 00	1120+143	2.370±0.002	11 20 15.02	12 59 29.5	4	1.56	64	5.2	2000	352.600	600.723
NGC 3627	D	AS750	2003-03-22	04 15	08 15	2 00	1120+143	2.370±0.002	11 20 15.02	12 59 29.5	4	1.56	64	5.2	2000	849.257	1098.203
NGC 4214	B	AM418	1994-06-30	23 00	06 00	5 45	1227+365	2.053±0.003	12 15 39.50	36 19 39.0	2AD	0.78	128	1.3	2000	291.0	...
NGC 4214	C	AM418	1993-08-09	20 15	00 45	4 00	1227+365	2.069±0.006	12 15 39.50	36 19 39.0	2AD	0.78	128	1.3	2000	291.0	...
NGC 4214	D	AM418	1994-01-27	08 30	11 00	2 15	1227+365	2.075±0.004	12 15 39.50	36 19 39.0	2AD	0.78	128	1.3	2000	291.0	...
NGC 4449	B	AH513	1994-09-05	15 15	03 00	9 00	1225+368	2.042±0.004	12 25 45.20	44 22 15.0	1A	3.125	64	5.2	1950	206.0	...
NGC 4449	C	AH359	1989-07-21	21 00	02 15	3 45	1225+368	2.166±0.028	12 25 45.20	44 22 15.0	1A	3.125	64	5.2	1950	206.0	...
NGC 4449	D	AH375	1989-11-10	13 30	18 45	4 30	1225+368	2.063±0.006	12 25 45.20	44 22 15.0	1A	3.125	64	5.2	1950	206.0	...
NGC 4736	B	AW605	2004-01-02	09 45	16 45	6 00	1227+365	2.075±0.010	12 50 53.06	41 07 13.7	4	1.56	64	5.2	2000	190.200	438.055
NGC 4736	C	AW605	2004-03-11	07 30	10 45	2 00	1227+365	2.063±0.005	12 50 53.06	41 07 13.7	4	1.56	64	5.2	2000	190.200	438.055
NGC 4736	D	AS750	2003-03-22	07 30	10 45	2 15	1227+365	2.041±0.009	12 50 53.06	41 07 13.7	4	1.56	64	5.2	2000	190.200	438.055
DDO 154	B	AW605	2005-05-06	01 45	09 15	6 15	1330+251	6.831±0.011	12 54 05.00	27 09 14.0	2AD	1.56	128	2.6	2000	375.0	...
DDO 154	C	AW605	2004-04-27	02 00	08 00	2 30	1330+251	6.846±0.007	12 54 05.00	27 09 14.0	2AD	1.56	128	2.6	2000	375.0	...
DDO 154	D	AW605	2004-07-05	00 10	02 10	1 30	1330+251	6.746±0.029	12 54 05.00	27 09 14.0	2AD	1.56	128	2.6	2000	375.0	...
NGC 4826	B	AW605	2005-03-18	05 45	12 45	6 15	1330+251	6.880±0.018	12 56 43.76	21 40 51.9	4	1.56	64	5.2	2000	283.200	531.200
NGC 4826	C	AW605	2004-02-23	08 00	10 00	1 45	1331+305	14.736	12 56 43.76	21 40 51.9	4	1.56	64	5.2	2000	283.200	531.200
NGC 4826	D	AS750	2004-02-23	11 45	14 00	1 45	1331+305	14.736	12 56 43.76	21 40 51.9	4	1.56	64	5.2	2000	283.200	531.200
NGC 5055	B	AW605	2004-01-05	09 30	16 30	6 00	1227+365	2.064±0.015	13 15 50.00	42 01 45.0	4	1.56	64	5.2	2000	626.134	377.968
NGC 5055	C	AW605	2004-04-27	22 30	08 00	2 30	1227+365	2.044±0.004	13 15 50.00	42 01 45.0	4	1.56	64	5.2	2000	626.134	377.968
NGC 5055	D	AW605	2004-07-02	21 30	03 00	1 30	1227+365	2.041±0.004	13 15 50.00	42 01 45.0	4	1.56	64	5.2	2000	626.134	377.968
NGC 5194	B	AW605	2005-03-05	06 00	13 15	6 15	1313+549	1.312±0.004	13 29 52.00	47 12 00.0	4	1.56	64	5.2	2000	587.102	339.000
NGC 5194	C	AW605	2004-04-26	03 15	08 00	2 15	1252+565	2.226±0.005	13 29 52.00	47 12 00.0	4	1.56	64	5.2	2000	587.102	339.000
NGC 5194	D	AW605	2004-07-10	00 45	02 30	1 15	1252+565	2.251±0.010	13 29 52.00	47 12 00.0	4	1.56	64	5.2	2000	587.102	339.000
NGC 5236	BnA	AP255	1993-02-01	08 30	15 30	6 00	1313-333	0.960±0.008	13 34 12.00	-29 37 00.0	2AD	1.56	128	2.6	1950	518.0	...
NGC 5236	BnA	AW605	2003-09-21	18 00	00 30	5 45	1313-333	0.960±0.008	13 34 12.00	-29 37 00.0	2AD	1.56	128	2.6	1950	518.0	...
NGC 5236	CnB	AP255	1993-05-26	02 15	07 00	3 45	1313-333	0.963±0.004	13 34 12.00	-29 37 00.0	2AD	1.56	128	2.6	1950	518.0	...
NGC 5236	DnC	AW605	2003-09-21	03 00	05 00	1 00	1313-333	1.148±0.004	13 34 12.00	-29 37 00.0	2AD	1.56	128	2.6	1950	518.0	...
NGC 5236	DnC	AP255	1993-10-23	17 15	19 45	2 00	1313-333	1.082±0.004	13 34 12.00	-29 37 00.0	2AD	1.56	128	2.6	1950	518.0	...
NGC 5457	B	AW605	2005-03-24	05 15	12 30	6 15	1400+621	4.333±0.012	14 03 12.00	54 21 00.0	4	1.56	64	5.2	2000	353.909	106.192
NGC 5457	C	AW605	2004-04-26	03 45	08 30	2 15	1400+621	4.307±0.007	14 03 12.00	54 21 00.0	4	1.56	64	5.2	2000	353.909	106.192
NGC 5457	D	AW605	2004-07-11	00 45	02 30	1 30	1400+621	4.272±0.009	14 03 12.00	54 21 00.0	4	1.56	64	5.2	2000	353.909	106.192
NGC 6946	B	AT258	2002-08-22	03 15	09 15	5 15	2022+616	1.912±0.004	20 34 52.00	60 09 00.0	2AB	1.56	256	1.3	2000	14.630	75.195
NGC 6946	B	AT258	2002-08-24	03 15	09 15	5 15	2022+616	1.913±0.004	20 34 52.00	60 09 00.0	2AB	1.56	256	1.3	2000	14.630	75.195
NGC 6946	C	AT258	2001-08-27	03 45	05 45	1 45	2022+616	2.016±0.004	20 34 52.00	60 09 00.0	2AB	1.56	256	1.3	2000	14.630	75.195
NGC 6946	D	AT258	2001-10-16	01 30	03 30	0 15	2022+616	1.990±0.004	20 34 52.00	60 09 00.0	2AB	1.56	256	1.3	2000	14.630	75.195
NGC 7331	B	AW605	2003-10-20	00 30	07 45	6 00	2236+284	1.427±0.003	22 37 04.09	34 24 56.3	4	1.56	64	5.2	2000	960.955	681.175
NGC 7331	B	AT220	1998-08-19	04 00	11 15	5 00	2236+284	1.082±0.002	22 37 04.09	34 24 56.3	1A	3.13	128	5.2	2000	821.0	...
NGC 7331	C	AT220	1998-11-27	22 30	02 15	2 15	2236+284	0.964±0.003	22 37 04.09	34 24 56.3	1A	3.13	128	5.2	2000	821.0	...
NGC 7331	D	AT220	1999-04-04	14 45	17 45	1 15	2236+284	0.966±0.005	22 37 04.09	34 24 56.3	1A	3.13	128	5.2	2000	821.0	...

TABLE 2  
SUMMARY OF THINGS OBSERVING SETUPS.

1	2	3	4	5	6	7	8	9	10	11	12	13	14	15	16	17	18
Name	Conf.	Project	Date yy-mm-dd	Start	End	Dur.	cal.	Flux Jy	RA hh mm ss	DEC dd mm ss	mode	BW MHz	chan #	$\Delta V$ km s <sup>-1</sup>	equ.	Vhel1 km s <sup>-1</sup>	Vhel2 km s <sup>-1</sup>
NGC 7793	BnA	AW605	2003-09-23	03 45	10 15	5 45	0025-260	8.550±0.044	23 57 49.00	-32 35 27.0	2AD	1.56	128	2.6	2000	230.0	...
NGC 7793	CnB	AW605	2004-02-03	21 00	23 30	2 00	0025-260	8.535±0.010	23 57 49.00	-32 35 27.0	2AD	1.56	128	2.6	2000	230.0	...
NGC 7793	DnC	AW605	2004-06-05	13 30	15 45	1 45	0025-260	8.527±0.012	23 57 49.00	-32 35 27.0	2AD	1.56	128	2.6	2000	230.0	...

NOTE. — *Comments on columns:*

*column 1:* galaxy name, *column 2:* VLA configuration used, *column 3:* program code (AW605: THINGS; others: archival data), *column 4:* observing date (local time: MST/MDT), *column 5/6:* start/end of observations (IAT), *column 7:* duration of observations (hours/minutes), *column 8/9:* name of phase calibrator and its flux density, *column 10/11:* coordinates of pointing centre of the array (equinox given in column 16), *column 12:* correlator mode, *column 13:* total bandwidth in MHz, *column 14:* number of channels per IF, *column 15:* channel width in km s<sup>-1</sup>, *column 16:* equinox, *column 17:* Barycentric (heliocentric) central velocities in km s<sup>-1</sup> (assuming the optical definition for the Doppler shift). In case two independent IFs were used, the central velocity of the second IF is also listed.

*Notes on Individual Galaxies:*

*NGC 1569:* Additional B-array observations in AW605 were observed in 1950 coordinates to facilitate combination.

*NGC 2976:* Observations done in mode 4AC; IF2 was employed at 25MHz to get quasi-continuum (which was not used for further analysis).

*NGC 3031:* Problems with continuum subtraction as HI emission fills almost all of the bandpass. Additional problems due to strong sidelobes from M 82.

*NGC 3184:* Archival B-array data do not have a usable bandpass calibrator (primary cal was observed in mode 2AC; data were taken in 2AD); flux of secondary was calculated 'by hand' and no bandpass correction was applied.

*NGC 3521:* C-array data were taken during snow; which resulted in low gains. Additional data were taken in DnC to make up for the loss in sensitivity.

*NGC 3621:* Observations were done doing three pointings along the major axis for the DnC observations. Only the central pointing has been used here for the final mapping.

*NGC 3627:* D-array data were observed over twice the range (using 2 × 2IFs) as compared to the B, C, and DnC-array data. Only the D-array IFs overlapping with the rest of the observations were used.

*NGC 4449:* 64 channels out of a total of 128 were selected in these archival observations (mode 1A; i.e. single polarisation only is available).

*NGC 6946:* Data were obtained in mode 2AB which implies only right hand circular polarisation is recorded. Also, no online Hanning smoothing was requested, this was applied off-line. D-array observations consist of mosaic; only the central pointing was used for the final mapping presented here.

*NGC 7331:* Only few channels available for continuum subtraction.

TABLE 2  
MAPPING/NOISE PARAMETERS OF THINGS GALAXIES

1	2	3	4	5	6	7	8	9	10
Name	Weighting	$B_{\text{maj}}$ "	$B_{\text{min}}$ "	BPA °	noise $\text{mJy beam}^{-1}$	size pixels	pixel "	channels	width $\text{km s}^{-1}$
NGC 628	NA	11.88	9.30	-70.3	0.60	1024	1.5	58	2.6
	RO	6.8	5.57	-61.4	0.66				
NGC 925	NA	5.94	5.71	30.6	0.57	1024	1.5	100	2.6
	RO	4.85	4.65	36.9	0.68				
NGC 1569	NA	7.71	7.04	16.5	0.81	1024	1.5	75	2.6
	RO	5.76	5.04	26.7	0.76				
NGC 2366	NA	13.10	11.85	-1.6	0.52	1024	1.5	66	2.6
	RO	6.96	5.94	20.2	0.61				
NGC 2403	NA	8.75	7.65	25.2	0.38	2048	1.0	61	5.2
	RO	6.01	5.17	18.1	0.45				
Ho II	NA	13.74	12.57	-43.0	0.92	1024	1.5	54	2.6
	RO	6.95	6.05	-32.8	1.06				
M81 dwA	NA	15.87	14.23	10.2	0.60	1024	1.5	46	1.3
	RO	7.79	6.27	4.4	0.69				
DDO 53	NA	11.75	9.53	-5.9	0.50	1024	1.5	41	2.6
	RO	6.34	5.67	2.6	0.53				
NGC 2841	NA	11.06	9.37	-12.3	0.35	1024	1.5	132	5.2
	RO	6.06	5.79	7.2	0.39				
NGC 2903	NA	15.27	13.32	-51.3	0.41	1024	1.5	87	5.2
	RO	8.66	6.43	-68.5	0.47				
Ho I	NA	14.66	12.73	-41.6	0.96	1024	1.5	36	2.6
	RO	7.78	6.03	-71.5	1.05				
NGC 2976	NA	7.41	6.42	71.8	0.36	1024	1.5	42	5.2
	RO	5.25	4.88	61.1	0.42				
NGC 3031	NA	12.91	12.41	79.9	0.66	2201	1.5	178	2.6
	RO	7.58	7.45	24.2	0.71				
NGC 3077	NA	14.31	13.24	60.5	0.75	1024	1.5	98	2.6
	RO	7.90	7.02	45.9	0.87				
M81 dwB	NA	12.45	10.56	-44.2	0.56	1024	1.5	34	2.6
	RO	7.05	5.84	-37.8	0.63				
NGC 3184	NA	7.51	6.93	85.4	0.36	1024	1.5	72	2.6
	RO	5.33	5.11	74.7	0.40				
NGC 3198	NA	13.01	11.56	-58.5	0.33	1024	1.5	72	5.2
	RO	7.64	5.62	-69.1	0.37				
IC 2574	NA	12.81	11.90	46.8	0.56	1024	1.5	83	2.6
	RO	5.93	5.48	-20.0	0.69				
NGC 3351	NA	9.94	7.15	24.1	0.35	1024	1.5	70	5.2
	RO	6.26	5.20	24.0	0.41				
NGC 3521	NA	14.14	11.15	-61.7	0.40	1024	1.5	109	5.2
	RO	8.19	6.41	-70.2	0.47				
NGC 3621	NA	15.95	10.24	3.6	0.69	1024	1.5	72	5.2
	RO	10.50	5.68	1.6	0.80				
NGC 3627	NA	10.60	8.85	-48.0	0.43	1024	1.5	92	5.2
	RO	5.67	5.45	-46.9	0.49				
NGC 4214	NA	14.69	13.87	-48.2	0.69	1024	1.5	98	1.3
	RO	7.41	6.35	-86.1	0.76				
NGC 4449	NA	21.21	20.28	-20.5	0.88	1024	1.5	45	5.2
	RO	13.74	12.50	-35.4	0.96				
NGC 4736	NA	10.22	9.07	-23.0	0.33	1024	1.5	68	5.2
	RO	5.96	5.55	25.1	0.38				
DDO 154	NA	14.09	12.62	-34.0	0.50	1024	1.5	57	2.6
	RO	7.94	6.27	-87.2	0.56				
NGC 4826	NA	12.18	9.35	-76.1	0.42	1024	1.5	75	5.2
	RO	7.26	5.68	-86.9	0.47				
NGC 5055	NA	10.06	8.66	-40.0	0.36	1024	1.5	87	5.2
	RO	5.78	5.26	33.3	0.41				
NGC 5194	NA	11.92	10.01	-86.0	0.39	1024	1.5	77	5.2
	RO	5.82	5.56	-68.0	0.44				
NGC 5236	NA	15.16	11.44	-3.0	0.83	2048	1.0	123	2.6
	RO	10.40	5.60	0.5	0.98				
NGC 5457	NA	10.82	10.17	-67.0	0.46	2048	1.0	69	5.2
	RO	7.49	6.07	-56.6	0.48				
NGC 6946	NA	6.04	5.61	6.6	0.55	1024	1.5	115	2.6
	RO	4.93	4.51	1.1	0.61				
NGC 7331	NA	6.13	5.61	34.3	0.44	1024	1.5	116	5.2
	RO	4.94	4.60	36.3	0.51				
NGC 7793	NA	15.60	10.85	10.7	0.92	1024	1.5	91	2.6
	RO	10.37	5.39	3.3	1.08				

NOTE. — Notes on columns:  
*column 1:* galaxy name  
*column 2:* weighting scheme used. NA: Natural, RO: Robust=0.5 weighting  
*column 3/4:* major and minor axis of synthesized beam in arcsec  
*column 5:* position angle of synthesized beam in degrees (measured north to east)  
*column 6:* noise in one channel map in  $\text{mJy beam}^{-1}$

TABLE 3  
 HI SPECTRUM OF M81 DWA BASED ON  
 THE BLANKED NATURAL WEIGHTED  
 CUBES (SEE THE ONLINE VERSION OF  
 THE JOURNAL FOR THE TABLES OF THE  
 OTHER THINGS TARGETS).

velocity $\text{km s}^{-1}$	HI flux density Jy
93.7	0.023
95.0	0.036
96.2	0.037
97.5	0.054
98.8	0.068
100.1	0.076
101.4	0.079
102.7	0.095
104.0	0.107
105.3	0.198
106.6	0.131
107.8	0.149
109.1	0.161
110.4	0.182
111.7	0.188
113.0	0.205
114.3	0.198
115.6	0.194
116.9	0.180
118.2	0.169
119.4	0.147
120.7	0.123
122.0	0.098
123.3	0.087
124.6	0.076
125.9	0.068
127.2	0.050
128.5	0.036
129.8	0.032
131.0	0.019

TABLE 4  
THINGS HI FLUXES, VELOCITIES, LINE-WIDTHS AND MASSES

1	2	3	4	5	6	7	8	9	10
name	$S_{\text{HI}}$ Jy km s <sup>-1</sup>	$M_{\text{HI}}$ 10 <sup>8</sup> $M_{\odot}$	$S_{\text{HI}}^{\text{Paturel}}$ Jy km s <sup>-1</sup>	$S_{\text{HI}}^{\text{Fisher\&Tully}}$ Jy km s <sup>-1</sup>	$v_{\text{cen}}$ km s <sup>-1</sup>	$v_{\text{cen}}^{\text{Fisher\&Tully}}$ km s <sup>-1</sup>	$W_{50}$ km s <sup>-1</sup>	$W_{20}$ km s <sup>-1</sup>	$W_{20}^{\text{Fisher\&Tully}}$ km s <sup>-1</sup>
NGC 628	302	38.0	252	381±17	659.1	659	56.4	75.4	74±5
NGC 925	232	45.8	197	301±14	552.5	554	207.1	222.6	224±8
NGC 1569	84.0	0.75	49.4	—	-85.6	—	100.8	123.8	—
NGC 2366	233	6.49	188	274±14	100.1	102	101.2	115.8	116±5
NGC 2403	1054	25.8	925	1458±47	133.1	132	240.6	254.7	247±20
Ho II	219	5.95	197	388±15	157.1	158	57.4	70.8	76±5
M81 dwA	4.1	0.12	—	—	112.0	—	24.7	36.6	—
DDDO 53	20.0	0.60	—	—	17.7	—	28.3	46.0	—
NGC 2841	183	85.8	125	—	635.2	—	587.3	607.7	—
NGC 2903	232	43.5	162	186±9.8	556.6	554	370.5	389.4	395±15
Ho I	40.1	1.39	36.1	42.4±2.6	140.4	141	27.9	41.4	46±5
NGC 2976	45.4	1.36	41.9	53.4±8.3	2.6	—	139.4	158.5	—
NGC 3031	1169	36.4	2177 <sup>+</sup>	—	-39.4	—	389.1	428.3	—
NGC 3077	256	8.81	361	—	-19.8	—	114.3	157.3	—
M81 dwB	3.8	0.25	—	—	346.4	—	44.9	58.5	—
NGC 3184	105	30.7	78.3	126±5.8	593.3	599	128.7	143.7	148±8
NGC 3198	227	101.7	146	206±12	661.2	660	298.0	313.2	322±7
IC 2574	387	14.8	438	499±17	48.6	38	109.0	130.8	117±10
NGC 3351	50.1	11.9	39.6	—	779.0	—	266.2	278.4	—
NGC 3521	297	80.2	199	281±40	798.2	804	440.5	467.7	466±10
NGC 3621	679	70.7	468	668±32	730.1	734	270.7	289.1	290±10
NGC 3627	40.6	8.18	40.0	60.6±5.1	717.3	737	351.6	389.4	382±15
NGC 4214	200	4.08	193	—	292.9	—	69.8	89.8	—
NGC 4449	263	11.0	101 <sup>+</sup>	—	202.7	—	116.2	163.5	—
NGC 4736	78.1	4.00	51.3	59.9±7.0	307.6	307	208.5	237.1	232±15
DDO 154	82.1	3.58	59.4	74.1±4.7	375.5	378	91.3	104.9	103±7
NGC 4826	41.5	5.48	45.1	56.3±15	407.9	414	304.0	321.6	311±20
NGC 5055	379	91.0	262	372±18	499.3	497	380.1	400.7	406±5
NGC 5194	169	25.4	141	202±14	456.2	467	162.8	191.4	195±10
NGC 5236	361	17.0	2454 <sup>+</sup>	—	510.0	—	200.8	273.8	—
NGC 5457	1102	141.7	1811 <sup>+</sup>	1572±42	226.5	231	169.6	199.0	200±7
NGC 6946	506	41.5	1336 <sup>+</sup>	—	43.3	—	221.4	239.7	—
NGC 7331	179	91.3	144	218±27	815.6	819	498.6	519.8	531±10
NGC 7793	246	8.88	197	271±13	227.2	231	176.5	191.1	194±7

NOTE. — Notes on columns:  
 Derived HI fluxes, masses and velocity widths.  
*Column 1:* Galaxy name,  
*Column 2:* THINGS HI flux. The total uncertainty is dominated by the accuracy of the flux calibration (of order 5%).  
*Column 3:* THINGS HI mass,  
*Column 4:* Single dish HI flux compiled from the literature by Paturel et al. (2003). Values with <sup>+</sup> indicate that galaxies are more extended than the area (primary beam) mapped by us.  
*Column 5:* Single dish HIFlux from Fisher & Tully 1981,  
*Column 6:* Velocity of the HI spectra, derived from the central velocity of the 20% level of the HI profile (column 9). A typical uncertainty is the width of one velocity channel (Tab. 2).  
*Column 7:* Heliocentric velocities from Fisher & Tully 1981,  
*Column 8:* Profile width at 50% of the peak intensity. A typical uncertainty is the width of one velocity channel (Tab. 2),  
*Column 9:* Profile width at 20% of the peak intensity. A typical uncertainty is the width of one velocity channel (Tab. 2),  
*Column 10:* Profile width at 20% of the peak intensity from Fisher & Tully 1981.

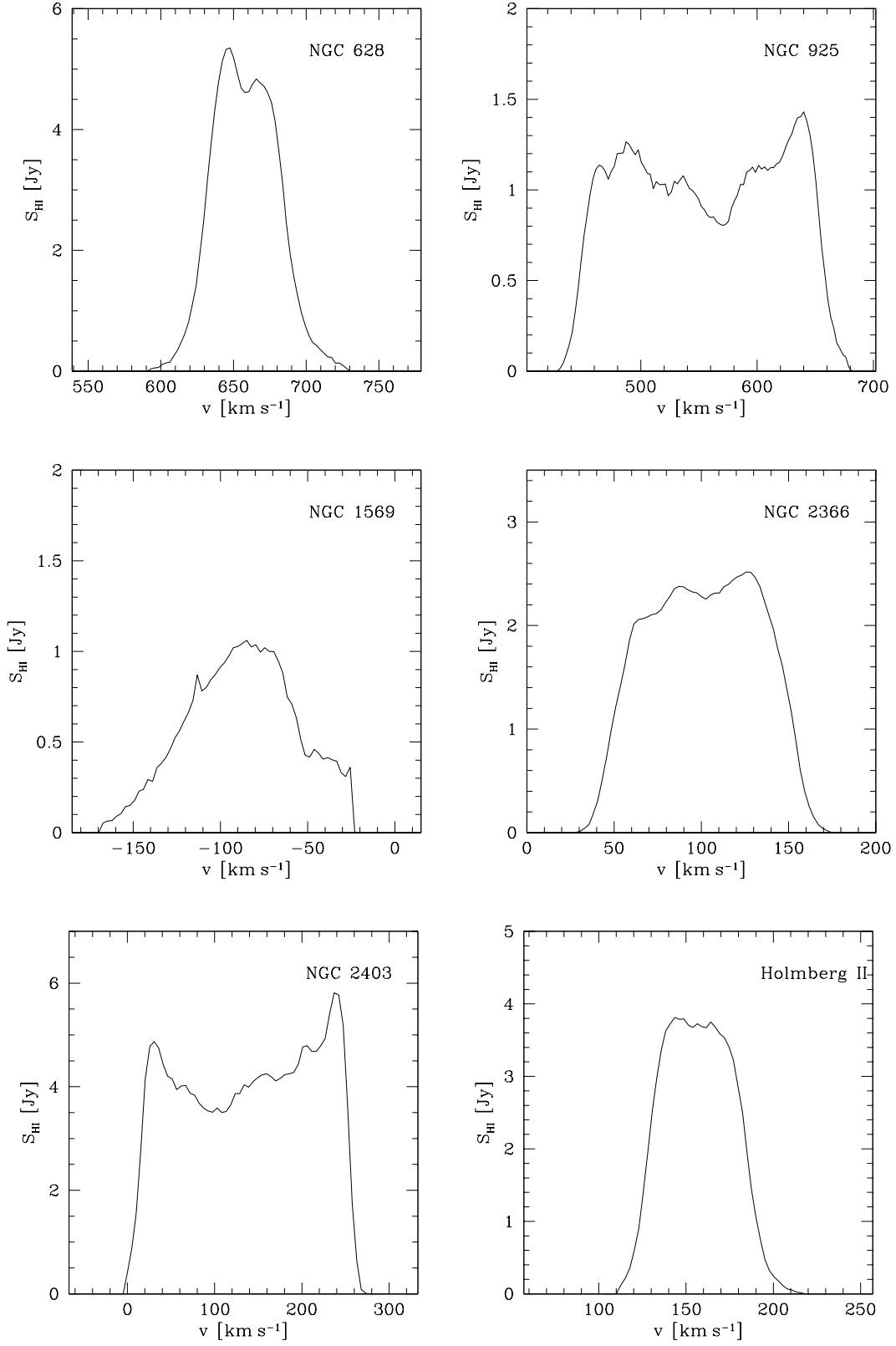


FIG. 1.— Global HI profiles for all THINGS galaxies.



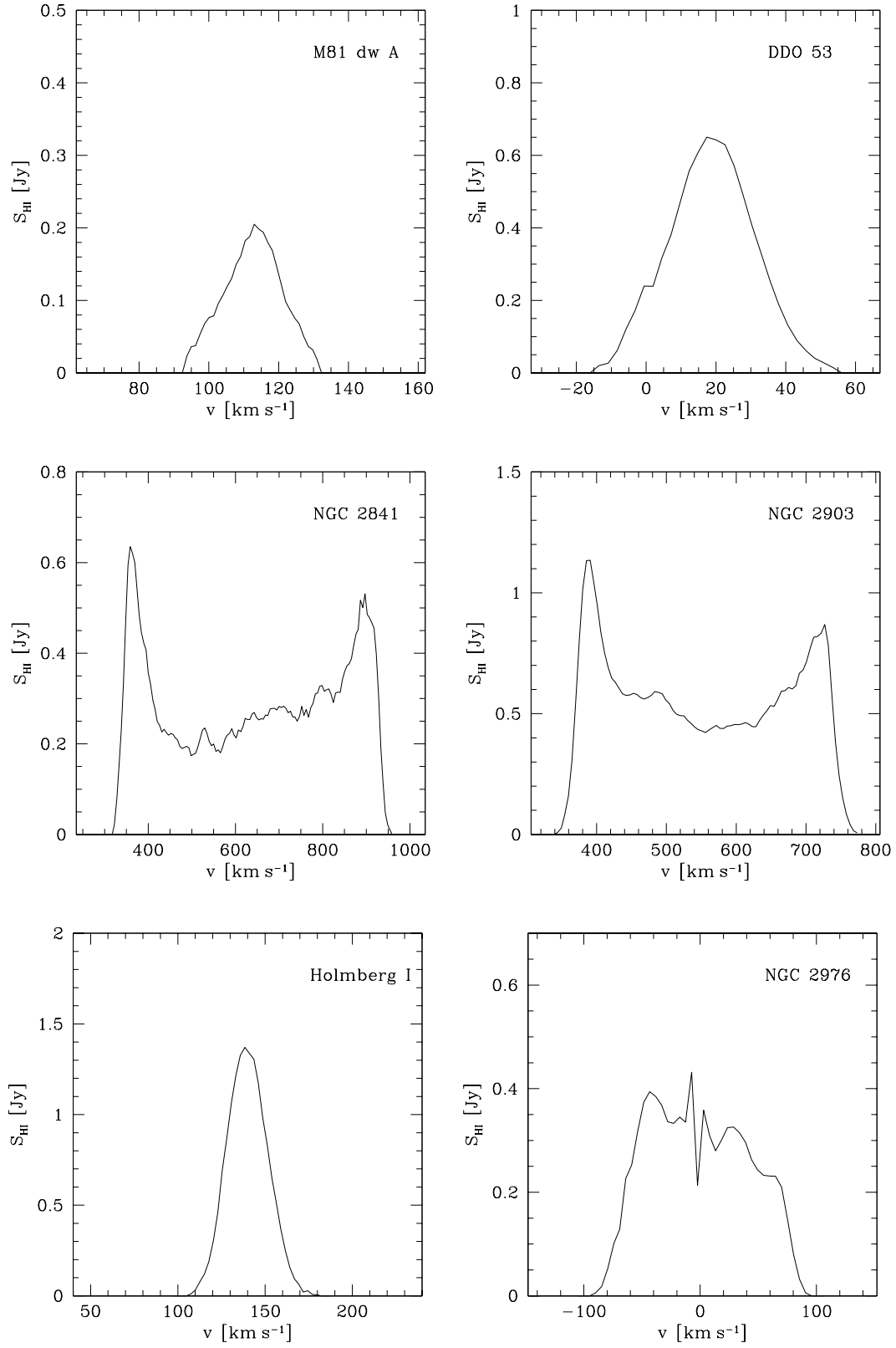


FIG. 1.— Global HI profiles for all THINGS galaxies (continued).

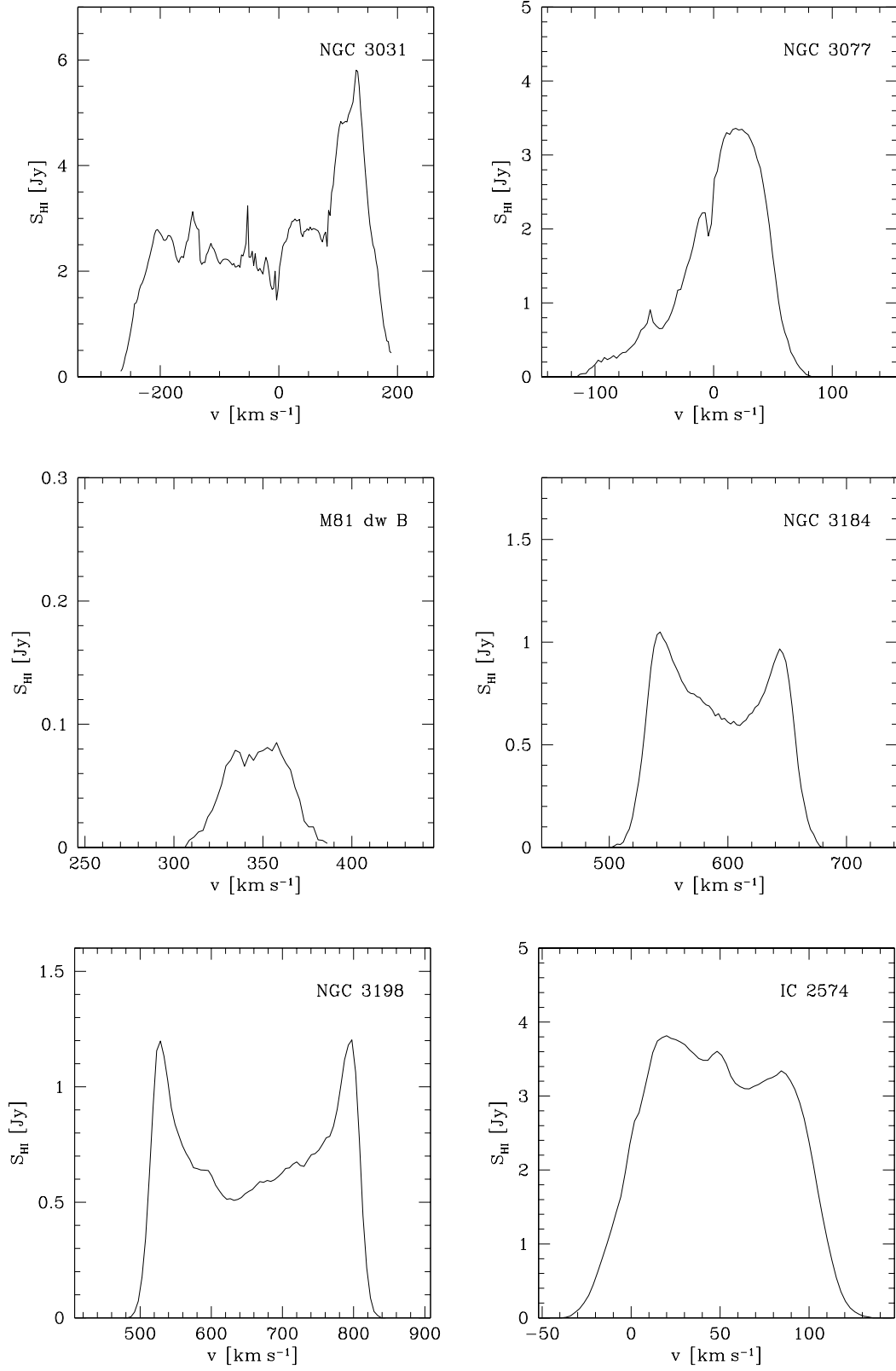


FIG. 1.— Global HI profiles for all THINGS galaxies (continued).

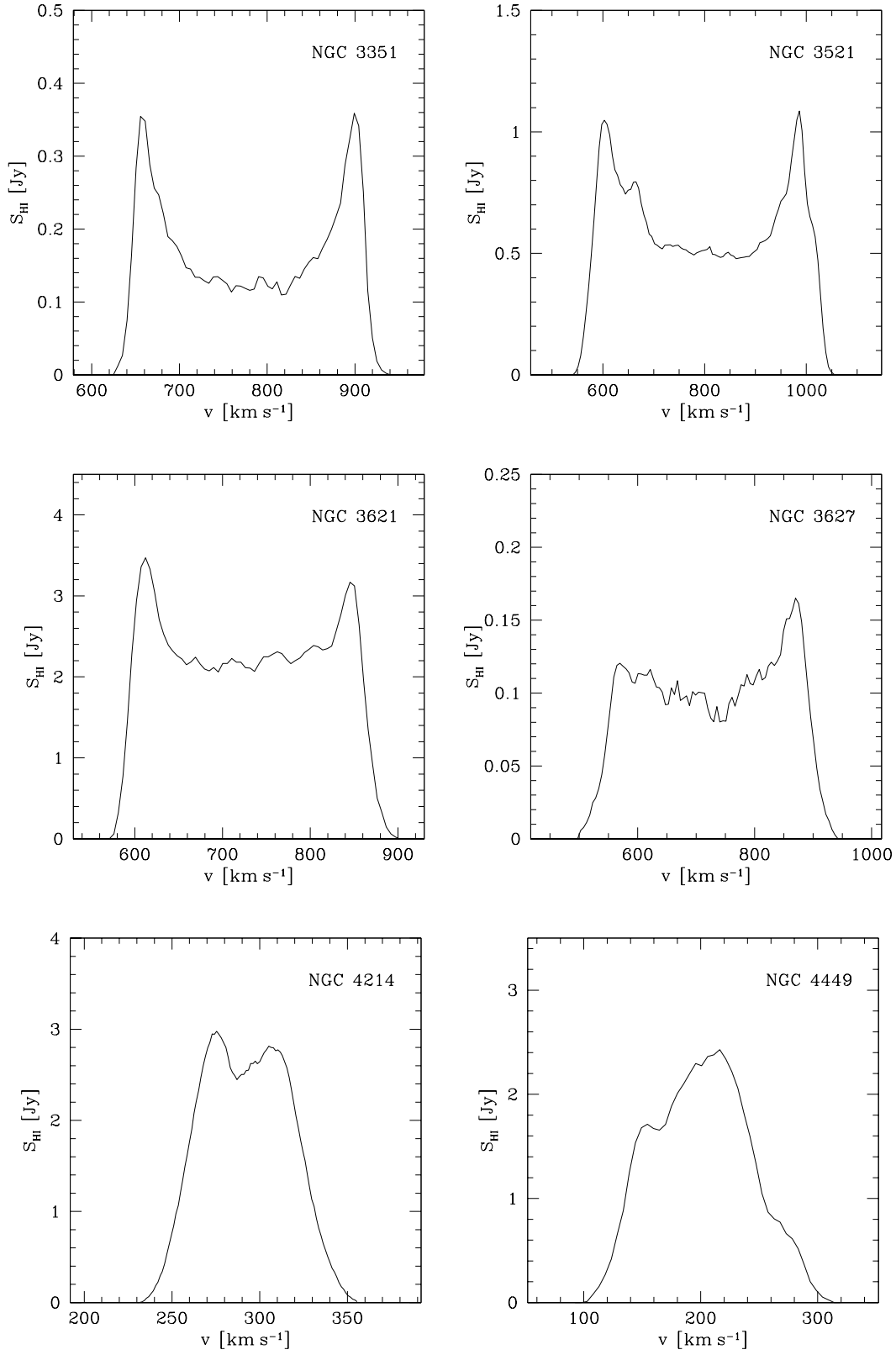


FIG. 1.— Global HI profiles for all THINGS galaxies (continued).

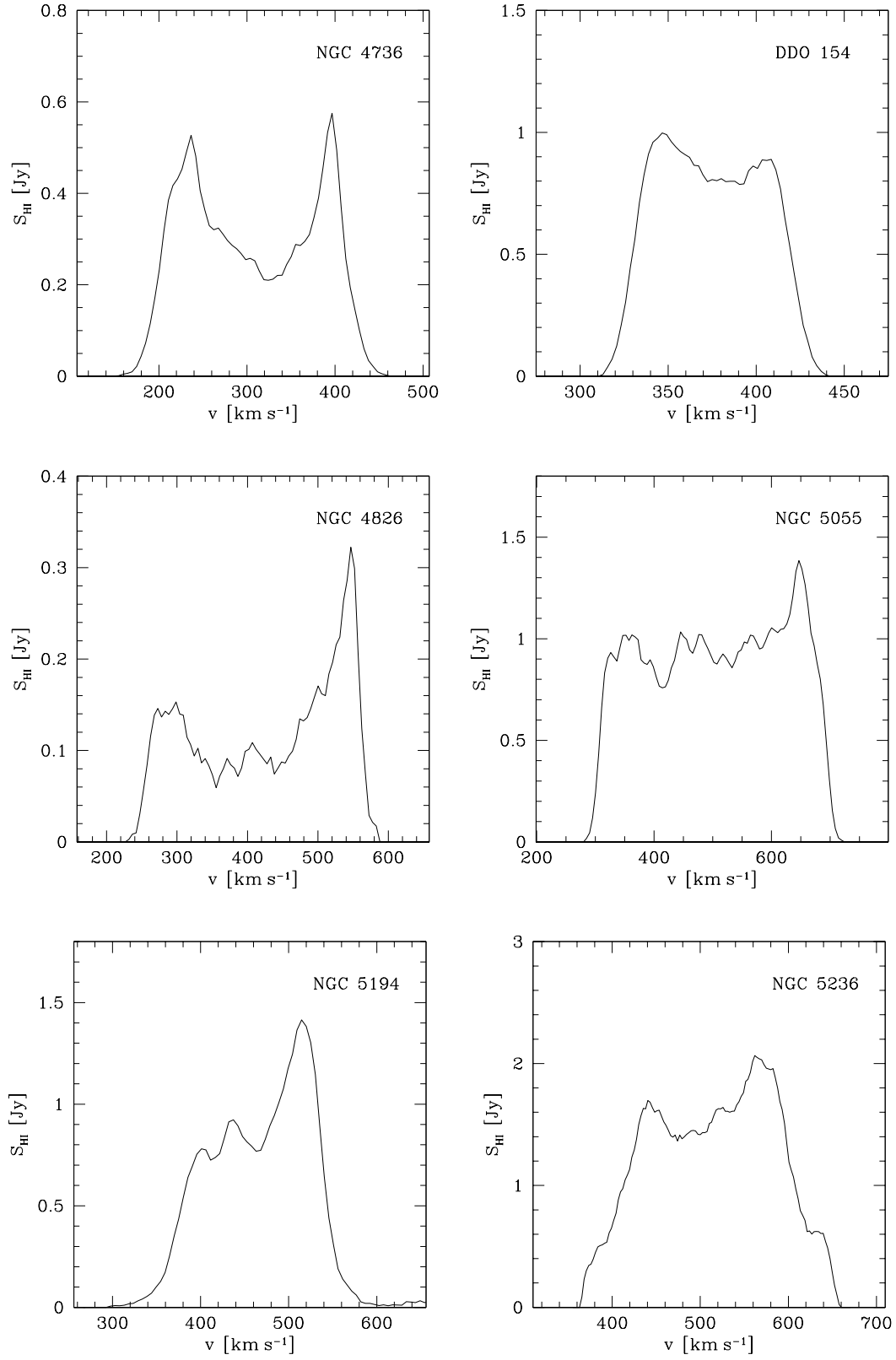


FIG. 1.— Global HI profiles for all THINGS galaxies (continued).

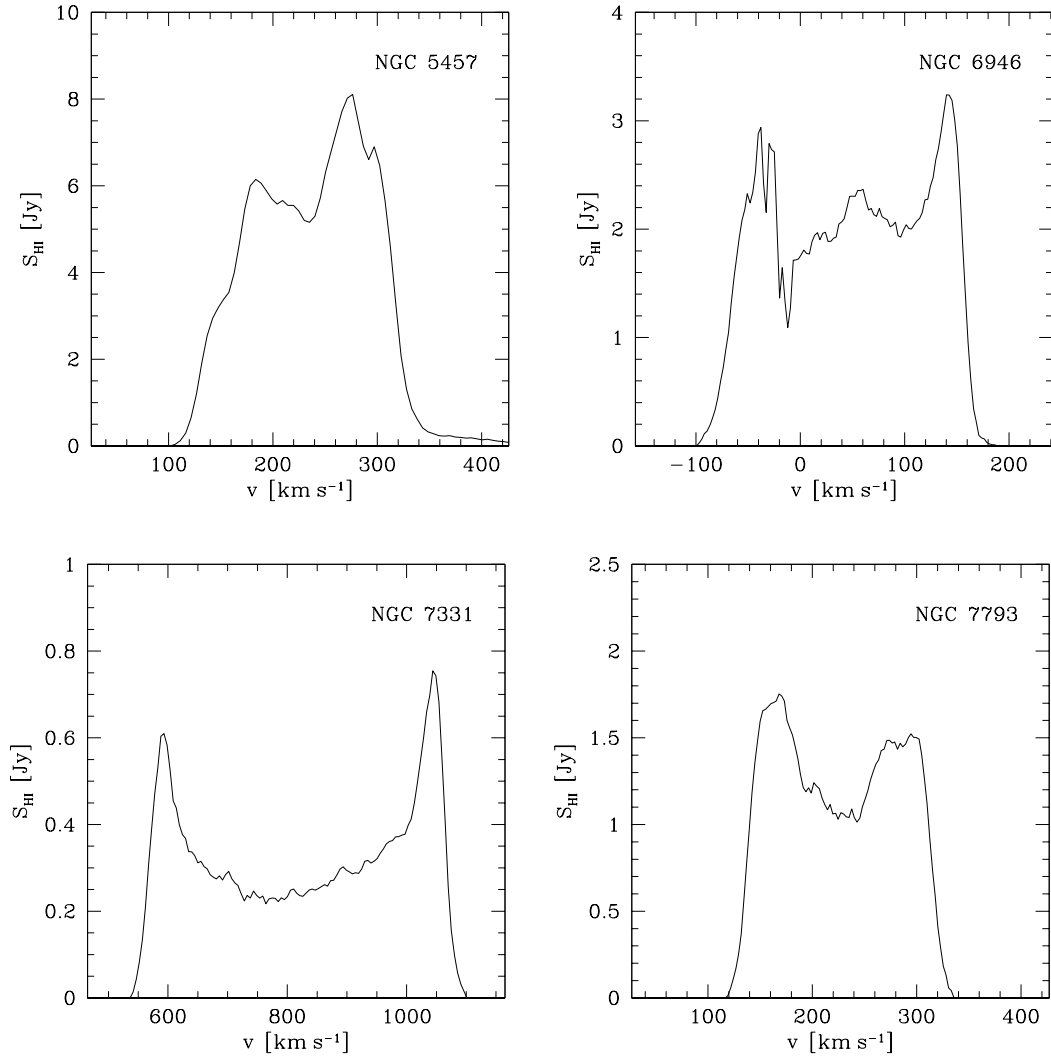


FIG. 1.— Global HI profiles for all THINGS galaxies (continued).

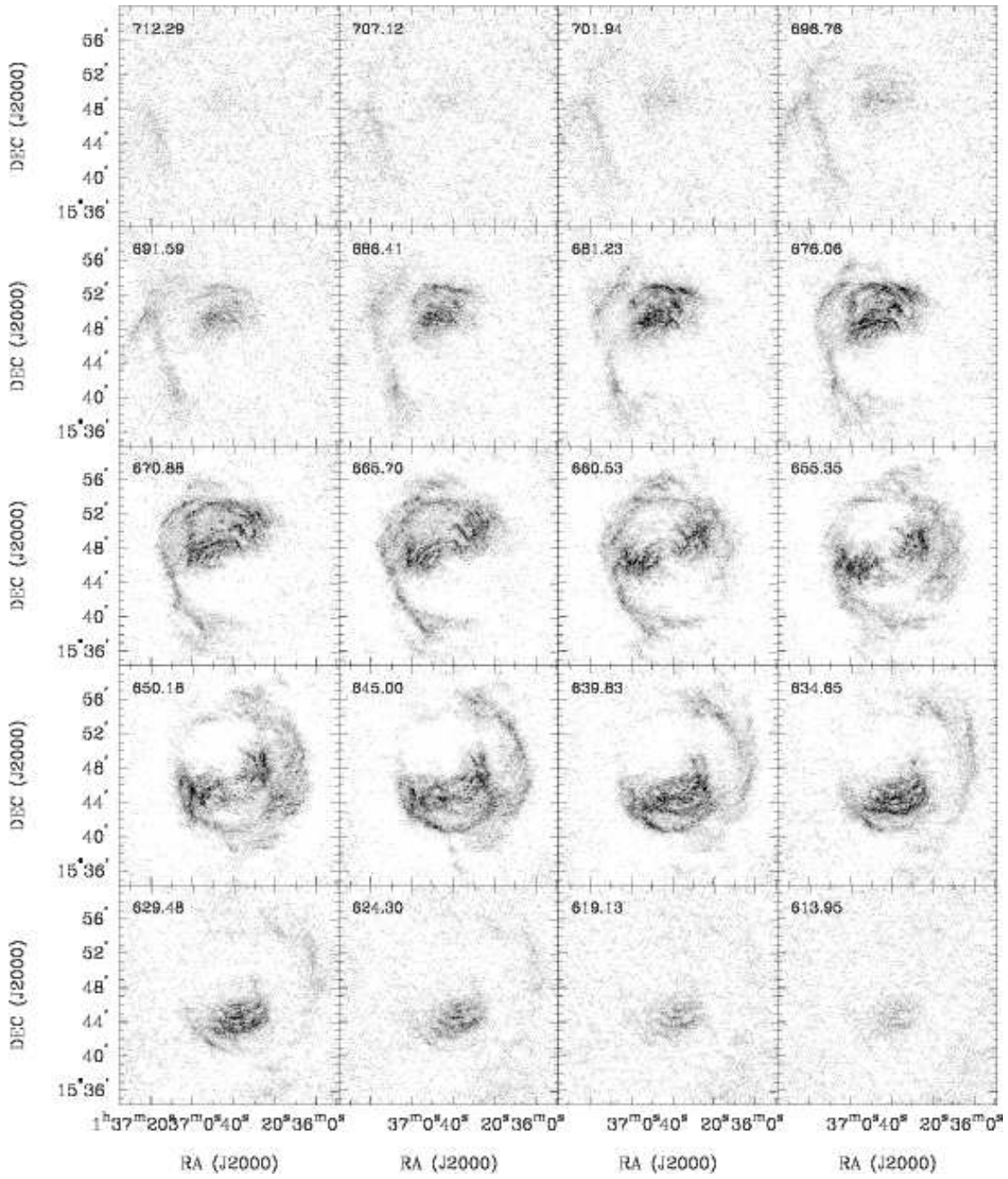


FIG. 2.— **NGC 628**: Channel maps based on the NA cube (greyscale range:  $-0.02$  to  $8 \text{ mJy beam}^{-1}$ ). Every second channel is shown (channel width:  $2.6 \text{ km s}^{-1}$ ). The area shown in each panel is identical to the area shown on the next figure

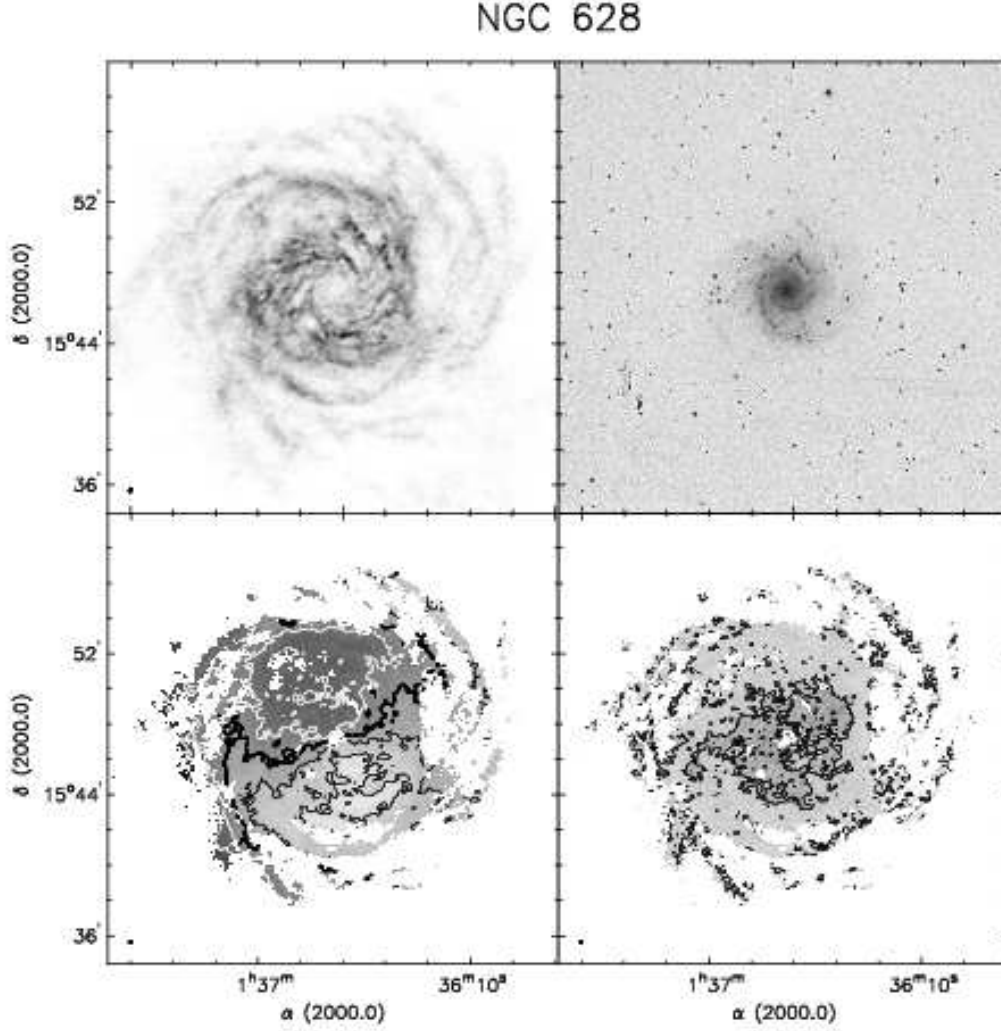


FIG. 3.— **NGC 628**. *Top left*: integrated HI map (moment 0). Greyscale range from 0–218  $\text{Jy km s}^{-1}$ . *Top right*: Optical image from the digitized sky survey (DSS). *Bottom left*: Velocity field (moment 1). Black contours (lighter greyscale) indicate approaching emission, white contours (darker greyscale) receding emission. The thick black contour is the systemic velocity ( $v_{\text{sys}}=659.1 \text{ km s}^{-1}$ ), the iso-velocity contours are spaced by  $\Delta v=12.5 \text{ km s}^{-1}$ . *Bottom right*: Velocity dispersion map (moment 2). Contours are plotted at 5, 10 and  $20 \text{ km s}^{-1}$ .

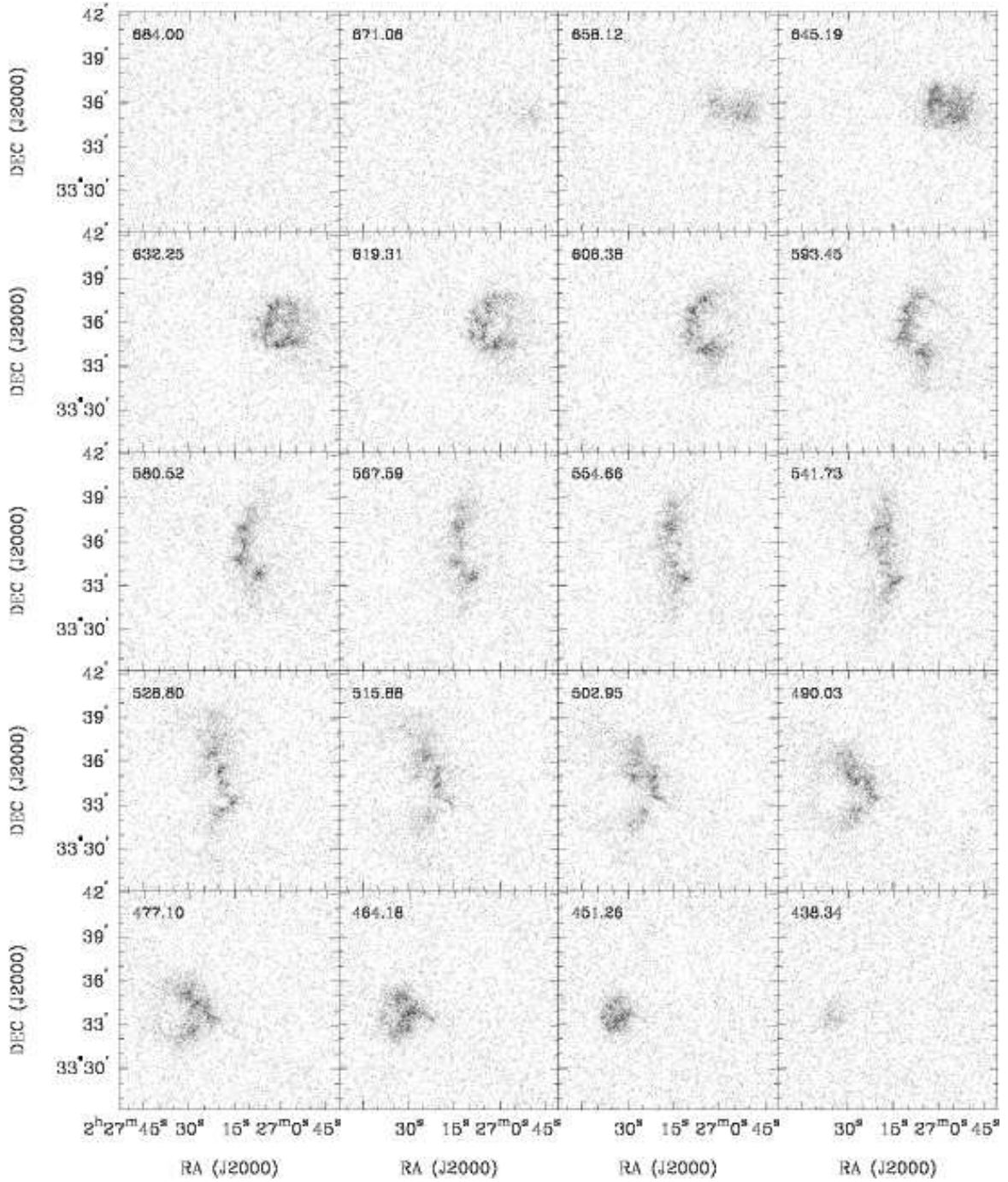


FIG. 4.— **NGC 925**: Channel maps based on the NA cube (greyscale range:  $-0.02$  to  $8 \text{ mJy beam}^{-1}$ ). Every fifth channel is shown (channel width:  $2.6 \text{ km s}^{-1}$ ). The area shown in each panel is identical to the area shown on the next figure



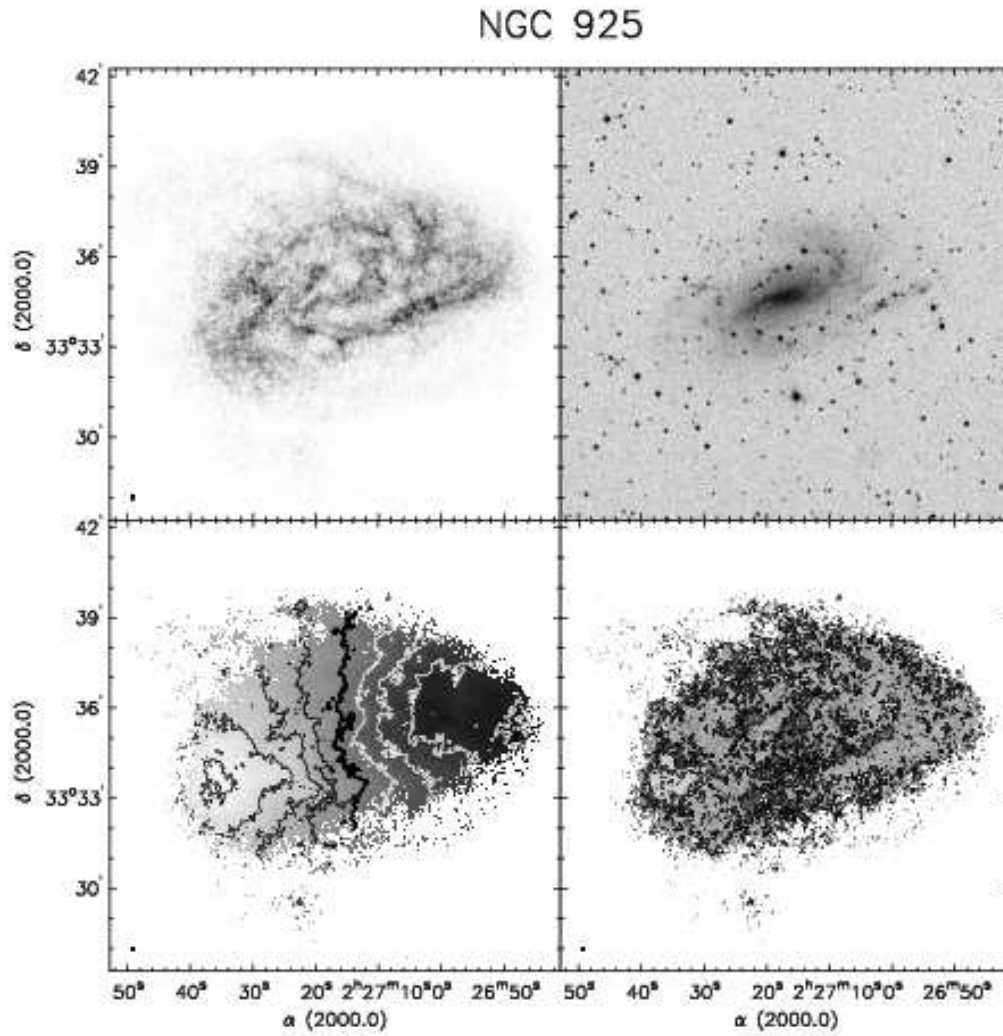


FIG. 5.— **NGC 925**. *Top left*: integrated HI map (moment 0). Greyscale range from 0–157  $\text{Jy km s}^{-1}$ . *Top right*: Optical image from the digitized sky survey (DSS). *Bottom left*: Velocity field (moment 1). Black contours (lighter greyscale) indicate approaching emission, white contours (darker greyscale) receding emission. The thick black contour is the systemic velocity ( $v_{\text{sys}}=552.5 \text{ km s}^{-1}$ ), the iso-velocity contours are spaced by  $\Delta v=25 \text{ km s}^{-1}$ . *Bottom right*: Velocity dispersion map (moment 2). Contours are plotted at 5, 10 and 20  $\text{km s}^{-1}$ .

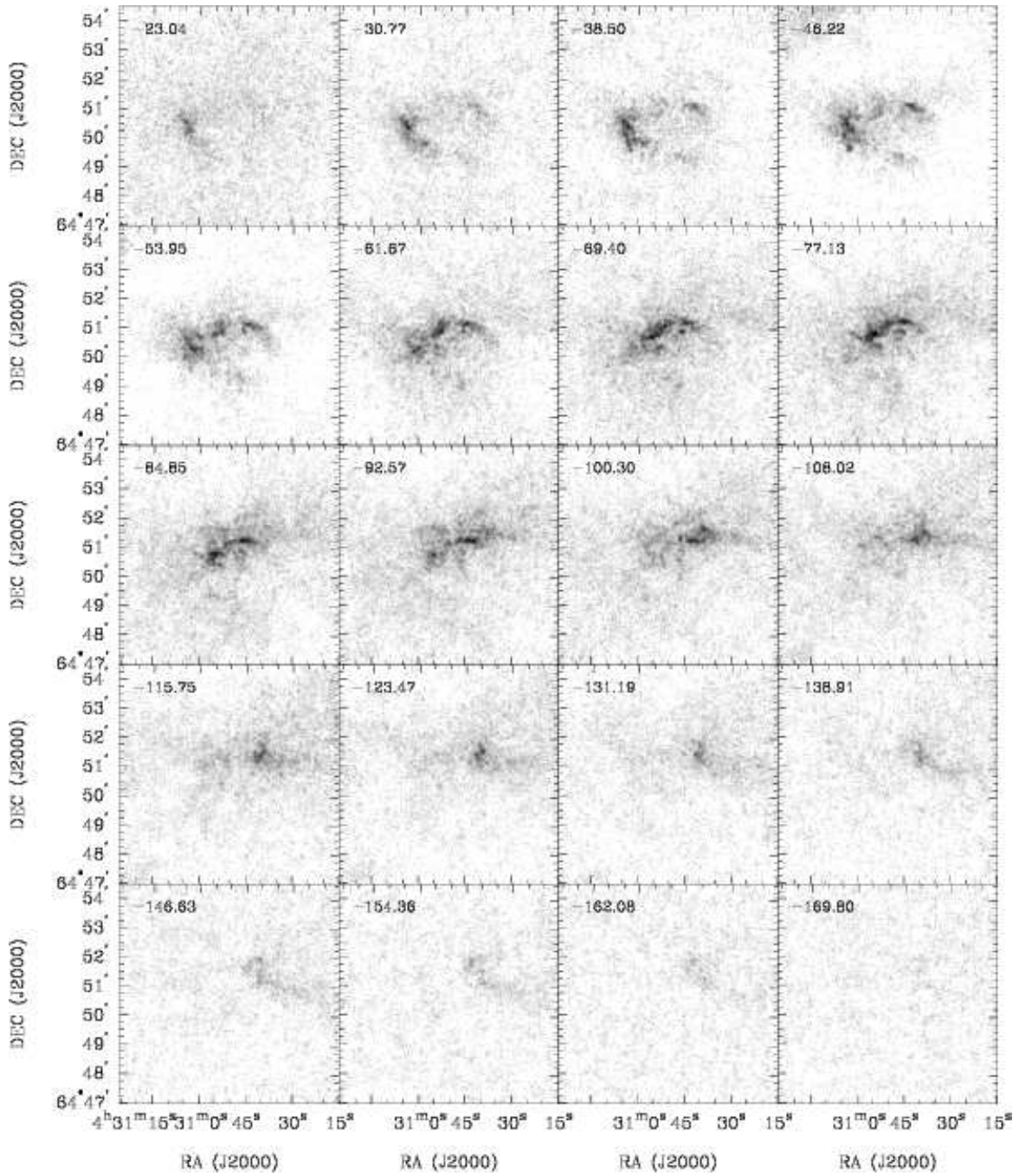


FIG. 6.— **NGC 1569**: Channel maps based on the NA cube (greyscale range:  $-0.02$  to  $10 \text{ mJy beam}^{-1}$ ). Every third channel is shown (channel width:  $2.6 \text{ km s}^{-1}$ ). The area shown in each panel is identical to the area shown on the next figure

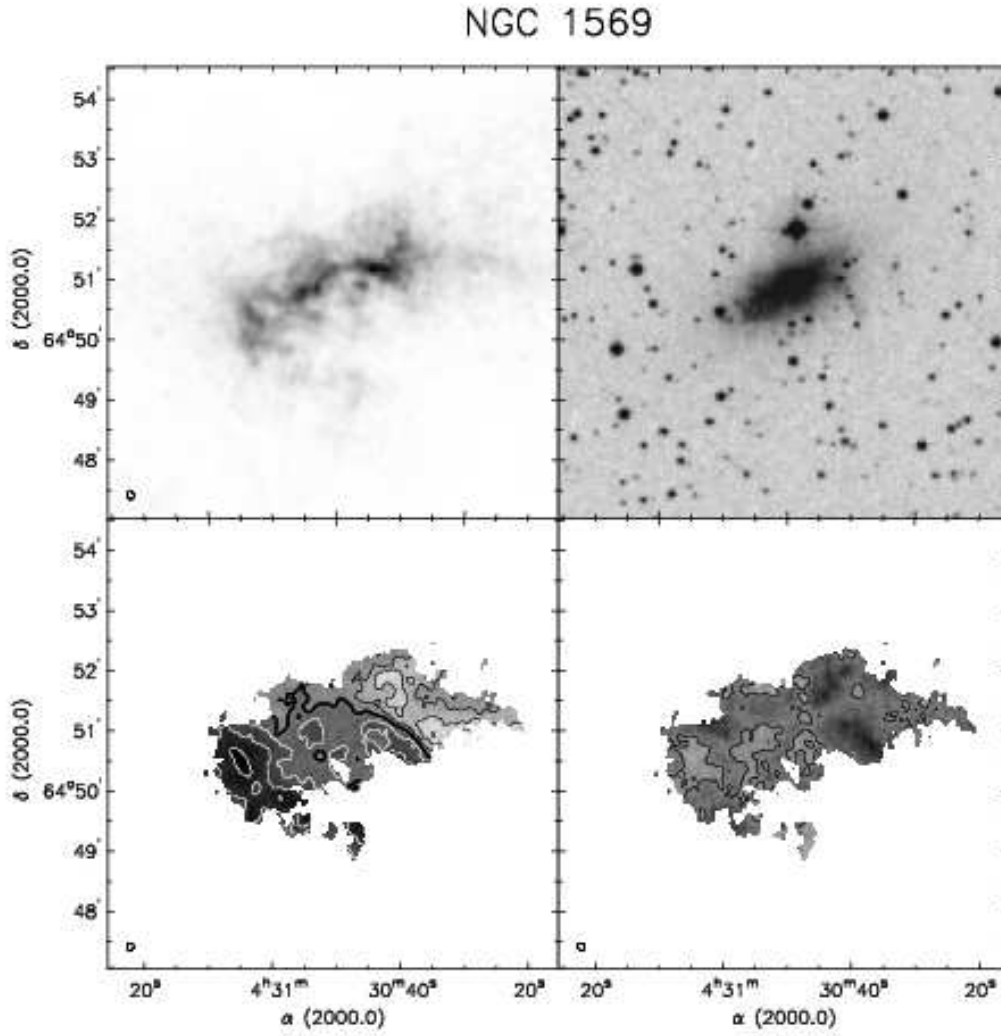


FIG. 7.— **NGC 1569**. *Top left*: integrated HI map (moment 0). Greyscale range from 0–426 Jy km s<sup>-1</sup>. *Top right*: Optical image from the digitized sky survey (DSS). *Bottom left*: Velocity field (moment 1). Black contours (lighter greyscale) indicate approaching emission, white contours (darker greyscale) receding emission. The thick black contour is the systemic velocity ( $v_{\text{sys}} = -85.57 \text{ km s}^{-1}$ ), the iso-velocity contours are spaced by  $\Delta v = 12.5 \text{ km s}^{-1}$ . *Bottom right*: Velocity dispersion map (moment 2). Contours are plotted at  $5 \text{ km s}^{-1}$ .



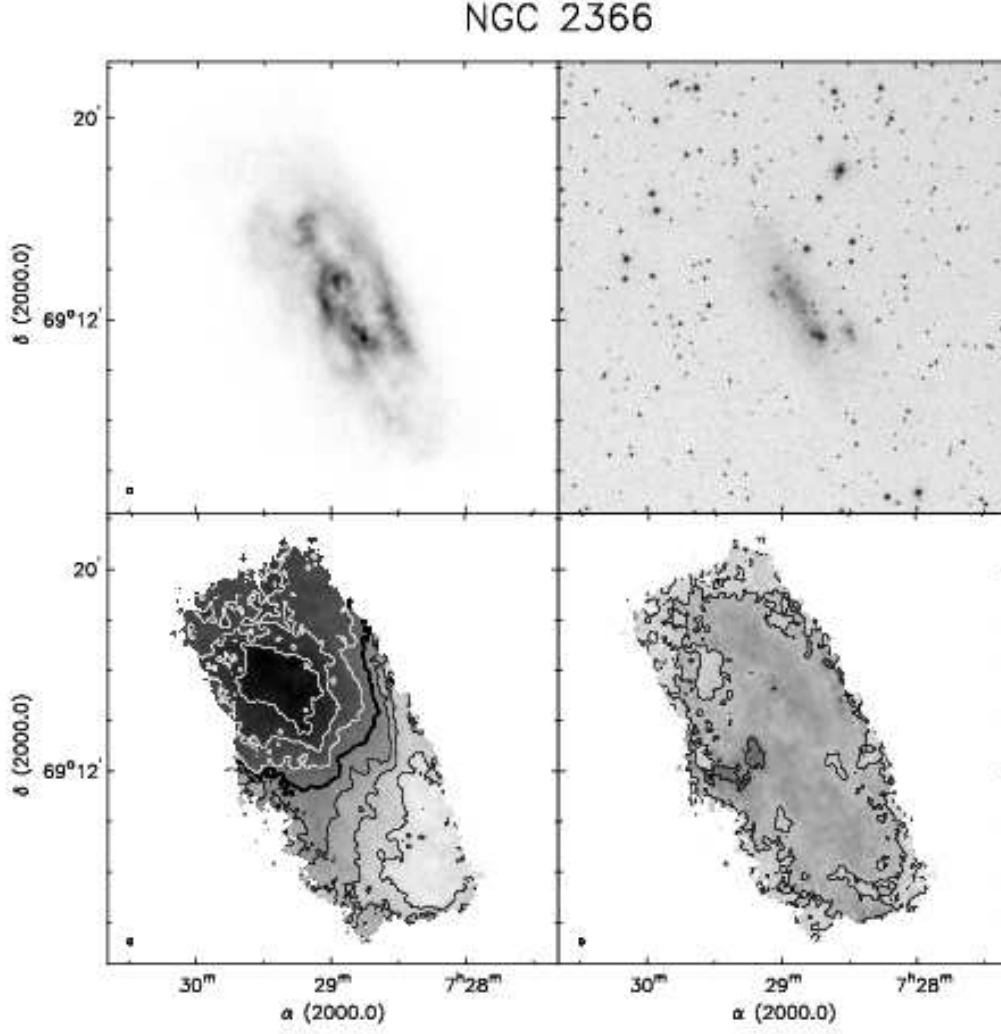


FIG. 9.— **NGC 2366**. *Top left*: integrated HI map (moment 0). Greyscale range from 0–1020  $\text{Jy km s}^{-1}$ . *Top right*: Optical image from the digitized sky survey (DSS). *Bottom left*: Velocity field (moment 1). Black contours (lighter greyscale) indicate approaching emission, white contours (darker greyscale) receding emission. The thick black contour is the systemic velocity ( $v_{\text{sys}}=100.1 \text{ km s}^{-1}$ ), the iso-velocity contours are spaced by  $\Delta v=12.5 \text{ km s}^{-1}$ . *Bottom right*: Velocity dispersion map (moment 2). Contours are plotted at 5, 10 and  $20 \text{ km s}^{-1}$ .

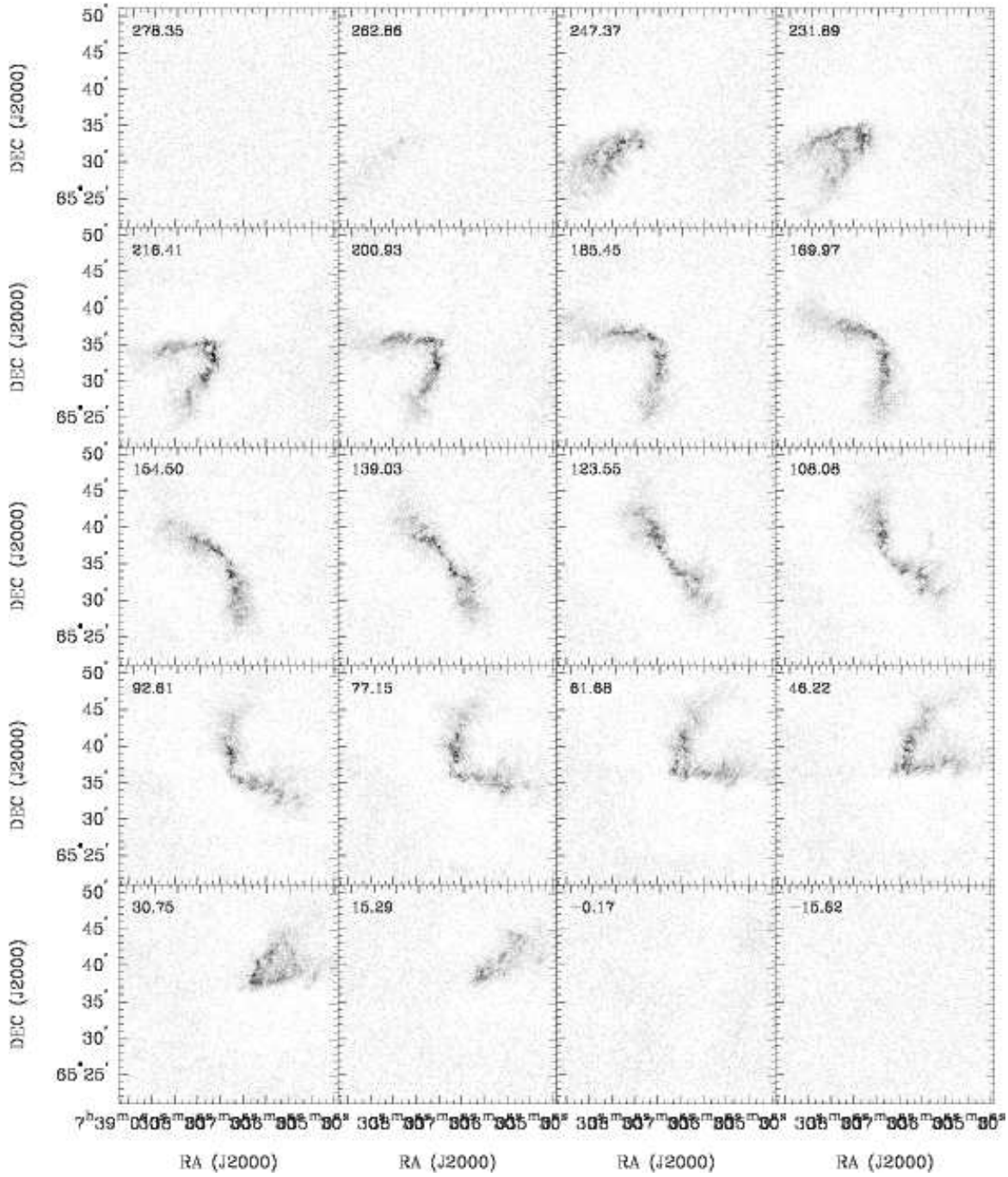


FIG. 10.— **NGC 2403**: Channel maps based on the NA cube (greyscale range:  $-0.02$  to  $10 \text{ mJy beam}^{-1}$ ). Every third channel is shown (channel width:  $5.2 \text{ km s}^{-1}$ ). The area shown in each panel is identical to the area shown on the next figure

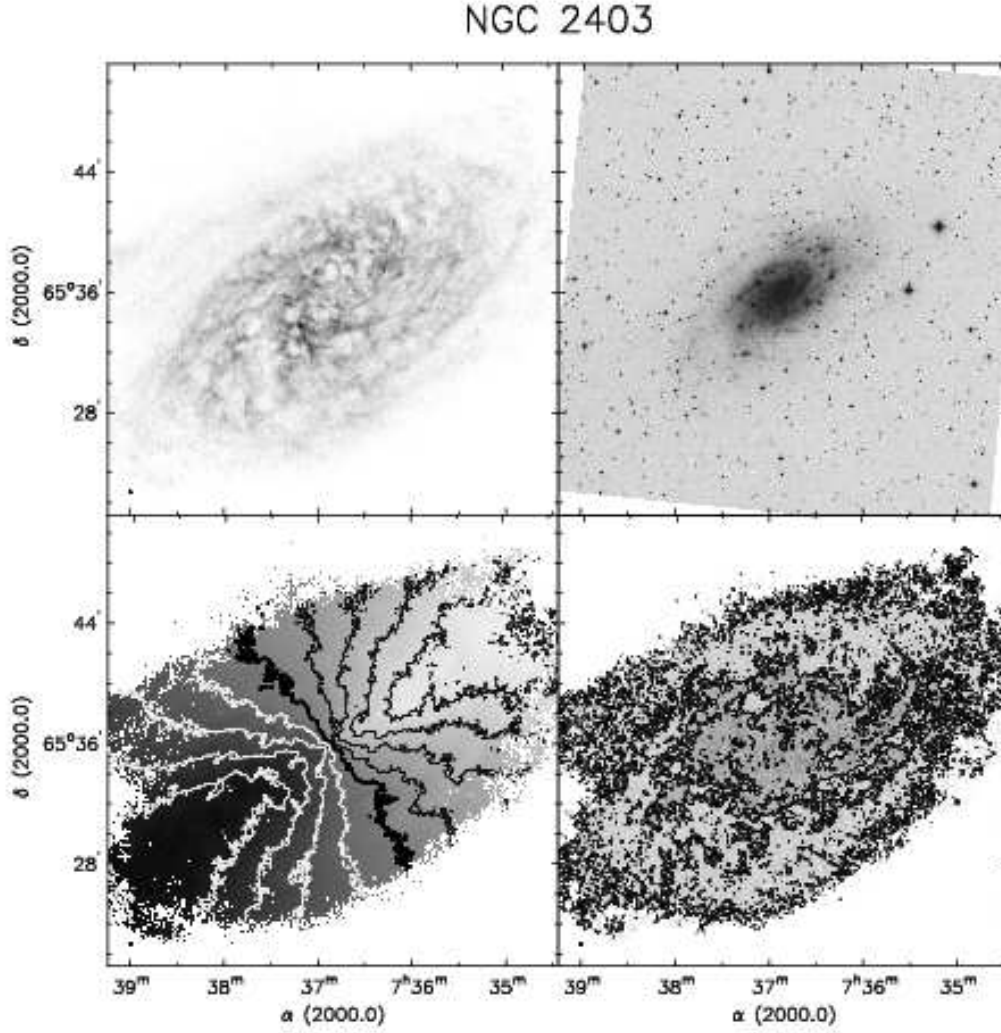


FIG. 11.— **NGC 2403**. *Top left*: integrated HI map (moment 0). Greyscale range from 0–357  $\text{Jy km s}^{-1}$ . *Top right*: Optical image from the digitized sky survey (DSS). *Bottom left*: Velocity field (moment 1). Black contours (lighter greyscale) indicate approaching emission, white contours (darker greyscale) receding emission. The thick black contour is the systemic velocity ( $v_{\text{sys}} = 133.1 \text{ km s}^{-1}$ ), the iso-velocity contours are spaced by  $\Delta v = 25 \text{ km s}^{-1}$ . *Bottom right*: Velocity dispersion map (moment 2). Contours are plotted at 5, 10 and 20  $\text{km s}^{-1}$ .

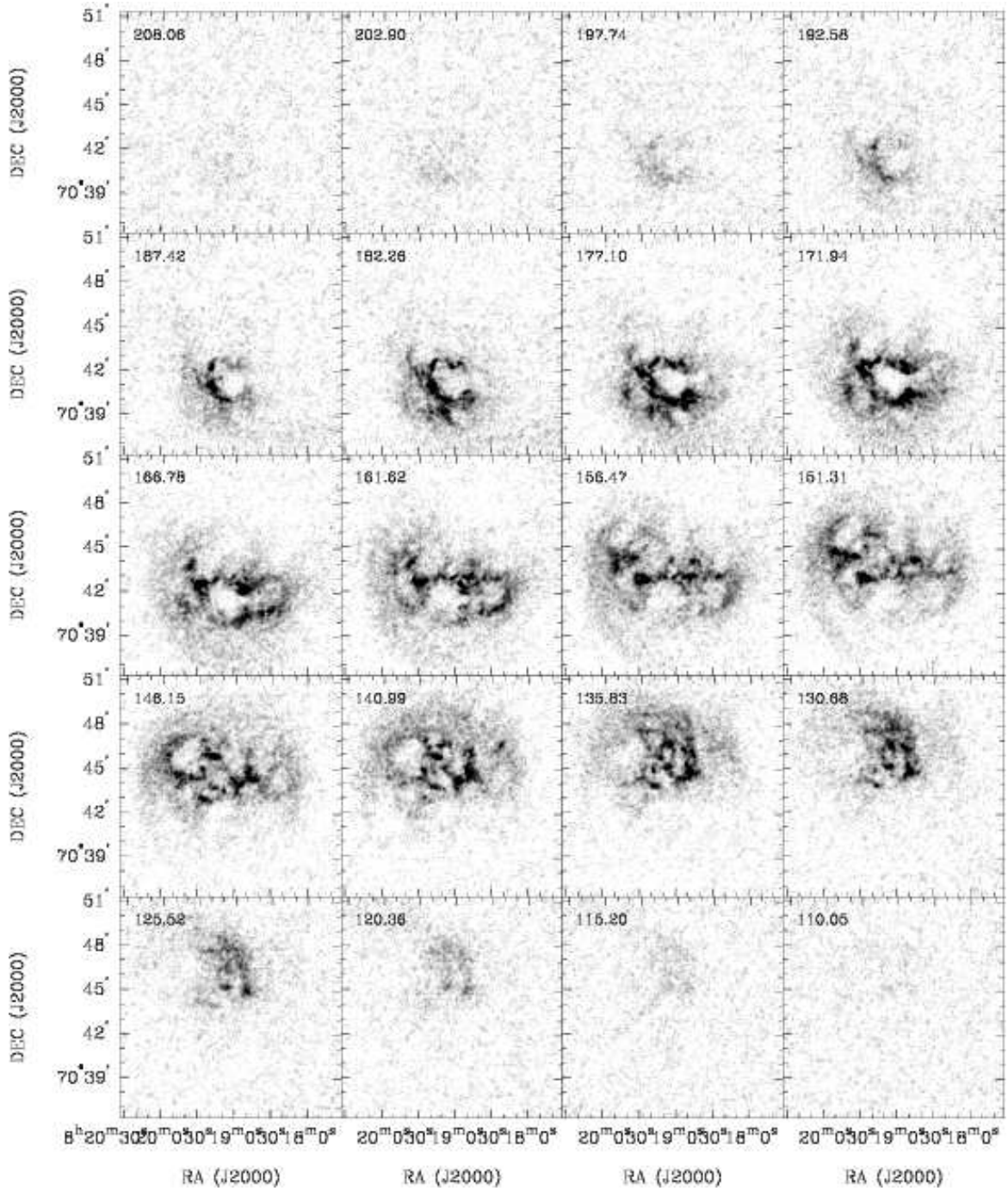


FIG. 12.— **Holmberg II**: Channel maps based on the NA cube (greyscale range:  $-0.02$  to  $13 \text{ mJy beam}^{-1}$ ). Every second channel is shown (channel width:  $2.6 \text{ km s}^{-1}$ ). The area shown in each panel is identical to the area shown on the next figure



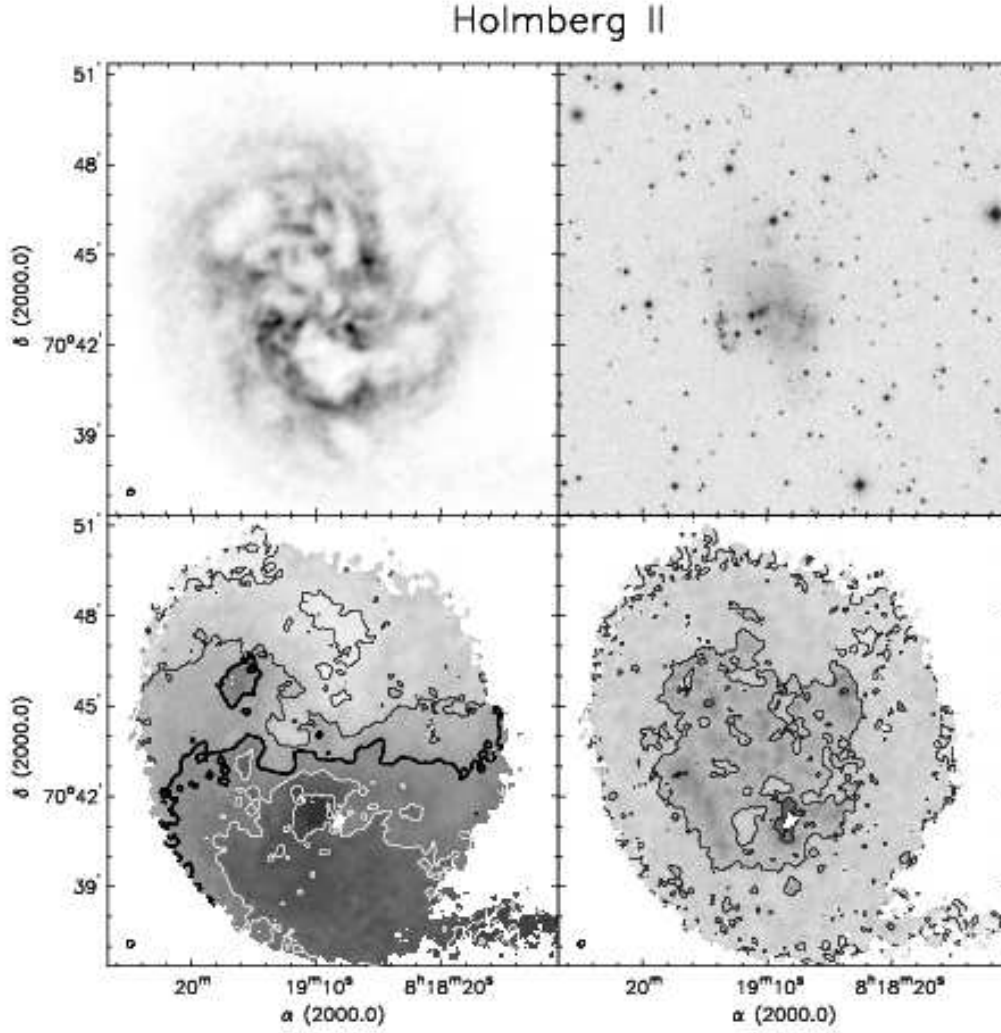


FIG. 13.— **Holmberg II**. *Top left*: integrated HI map (moment 0). Greyscale range from 0–599  $\text{Jy km s}^{-1}$ . *Top right*: Optical image from the digitized sky survey (DSS). *Bottom left*: Velocity field (moment 1). Black contours (lighter greyscale) indicate approaching emission, white contours (darker greyscale) receding emission. The thick black contour is the systemic velocity ( $v_{\text{sys}}=157.1 \text{ km s}^{-1}$ ), the iso-velocity contours are spaced by  $\Delta v=12.5 \text{ km s}^{-1}$ . *Bottom right*: Velocity dispersion map (moment 2). Contours are plotted at 5, 10 and  $20 \text{ km s}^{-1}$ .

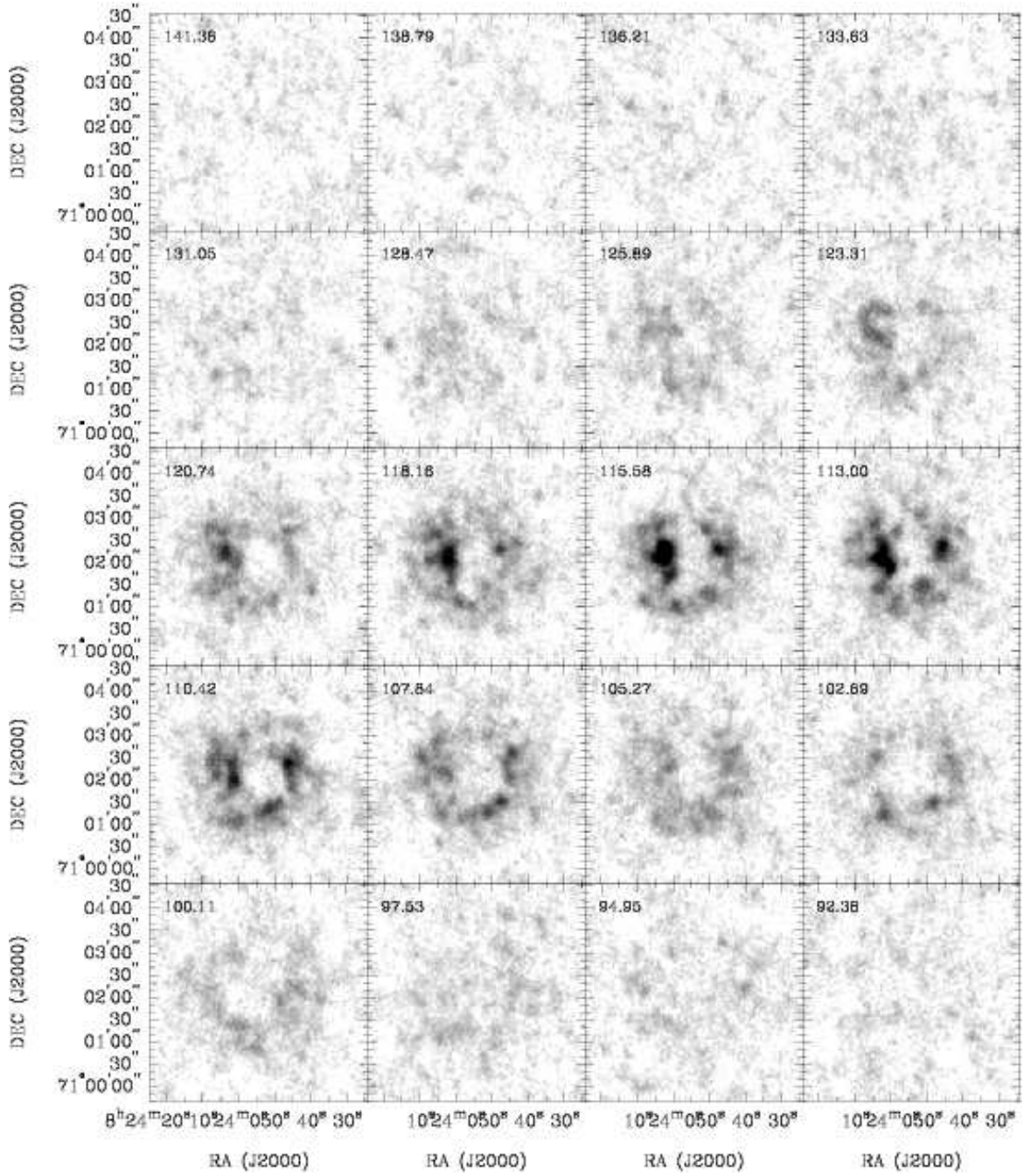


FIG. 14.— **M81 dwarf A**: Channel maps based on the NA cube (greyscale range:  $-0.2$  to  $8 \text{ mJy beam}^{-1}$ ). Every second channel is shown (channel width:  $1.3 \text{ km s}^{-1}$ ). The area shown in each panel is identical to the area shown on the next figure.

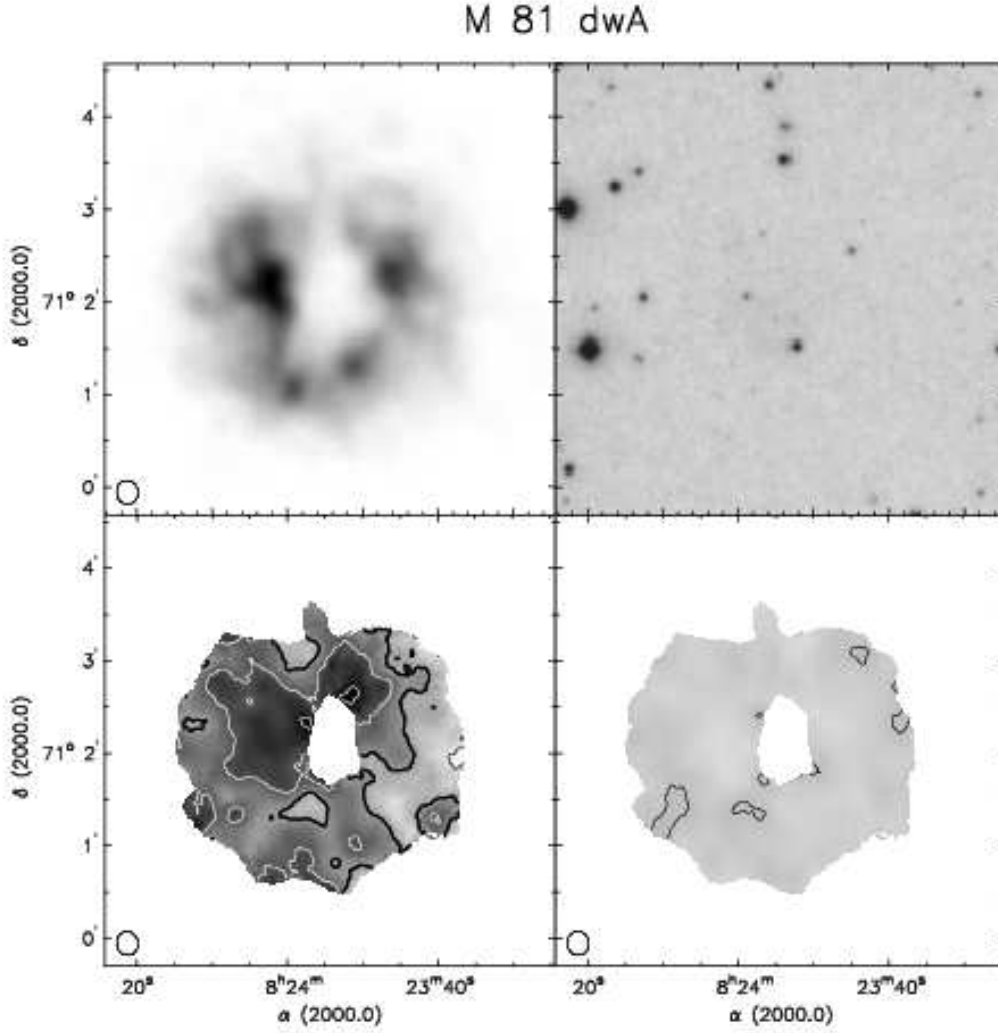


FIG. 15.— **M 81 dwarf A.** *Top left:* integrated HI map (moment 0). Greyscale range from 0–125  $\text{Jy km s}^{-1}$ . *Top right:* Optical image from the digitized sky survey (DSS). *Bottom left:* Velocity field (moment 1). Black contours (lighter greyscale) indicate approaching emission, white contours (darker greyscale) receding emission. The thick black contour is the systemic velocity ( $v_{\text{sys}}=110.76 \text{ km s}^{-1}$ ), the iso-velocity contours are spaced by  $\Delta v=3.1 \text{ km s}^{-1}$ . *Bottom right:* Velocity dispersion map (moment 2). A contour is plotted at  $5.0 \text{ km s}^{-1}$ .

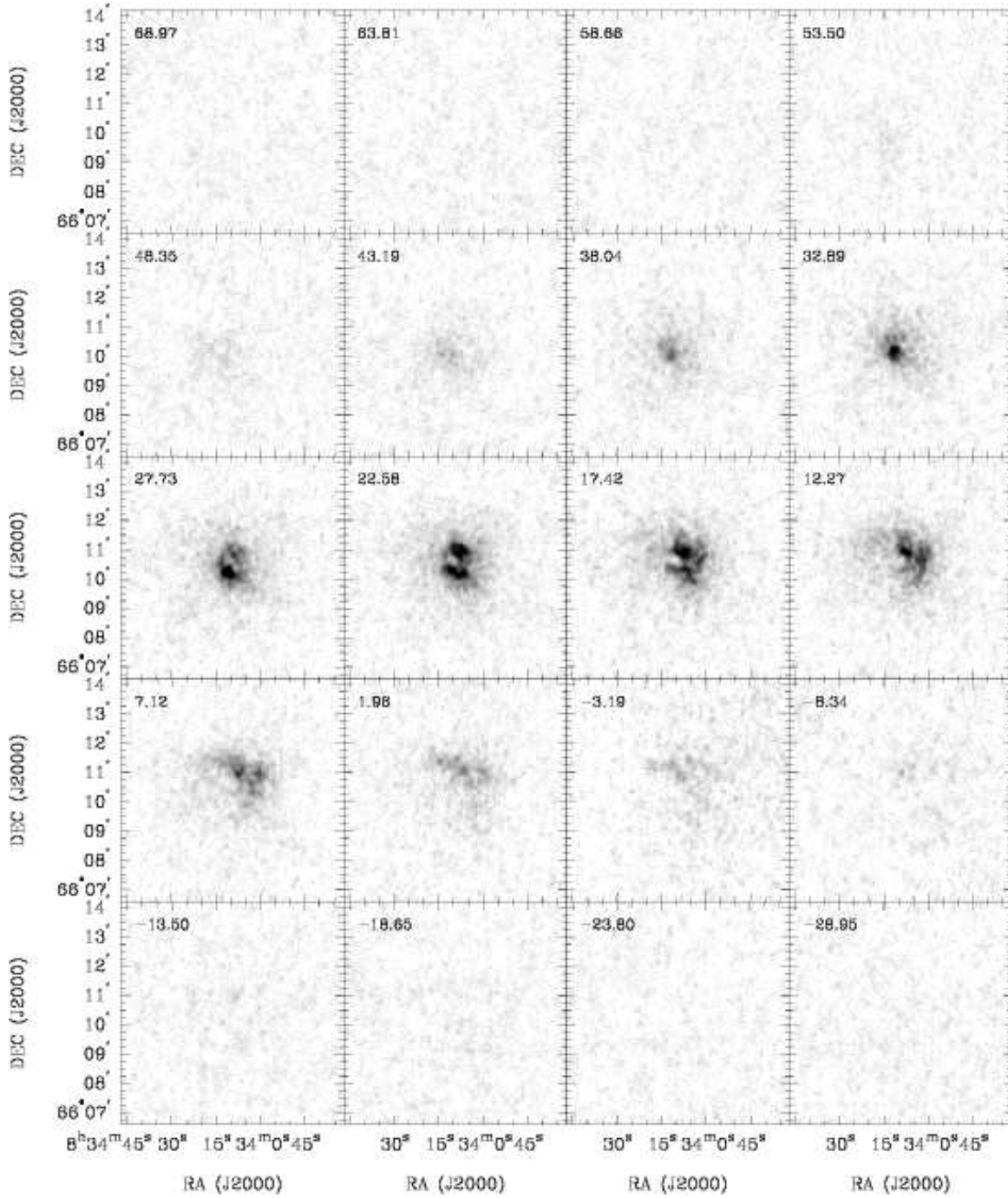


FIG. 16.— **DDO 53**: Channel maps based on the NA cube (greyscale range:  $-0.02$  to  $12 \text{ mJy beam}^{-1}$ ). Every second channel is shown (channel width:  $2.6 \text{ km s}^{-1}$ ). The area shown in each panel is identical to the area shown on the next figure

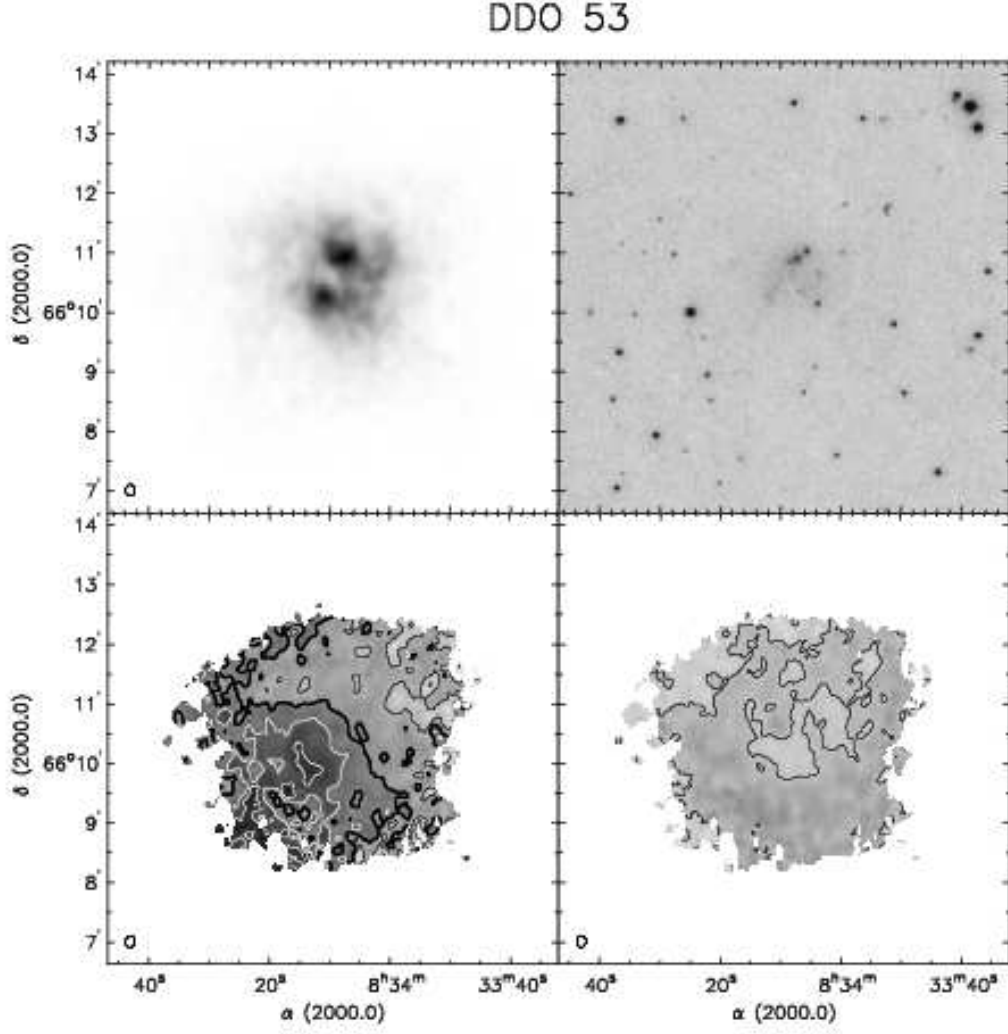


FIG. 17.— **DDO 53**. *Top left*: integrated HI map (moment 0). Greyscale range from 0–338  $\text{Jy km s}^{-1}$ . *Top right*: Optical image from the digitized sky survey (DSS). *Bottom left*: Velocity field (moment 1). Black contours (lighter greyscale) indicate approaching emission, white contours (darker greyscale) receding emission. The thick black contour is the systemic velocity ( $v_{\text{sys}}=17.71 \text{ km s}^{-1}$ ), the iso-velocity contours are spaced by  $\Delta v=6.25 \text{ km s}^{-1}$ . *Bottom right*: Velocity dispersion map (moment 2). A contour is plotted at  $5.0 \text{ km s}^{-1}$ .

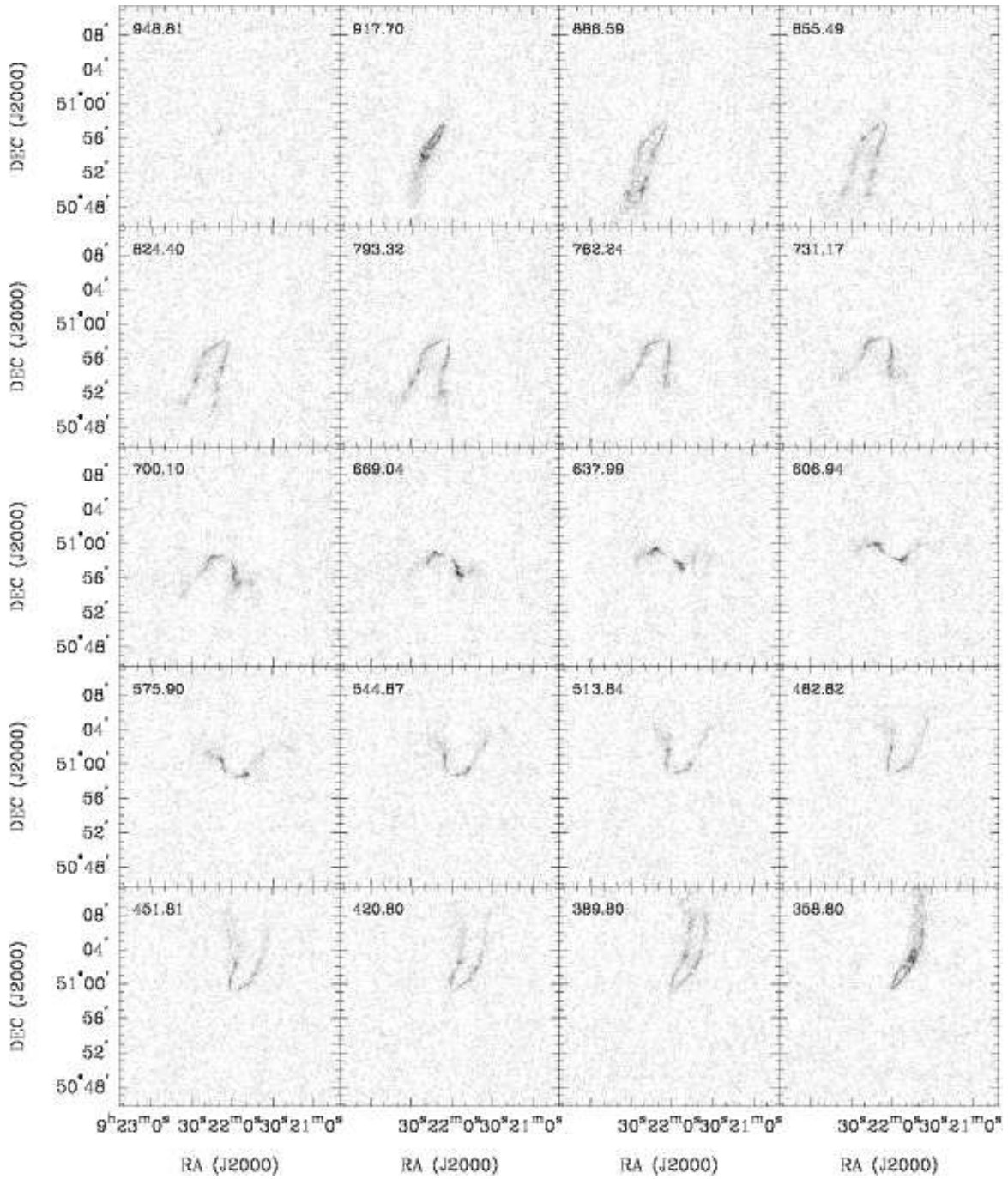


FIG. 18.— **NGC 2841**: Channel maps based on the NA cube (greyscale range:  $-0.02$  to  $7 \text{ mJy beam}^{-1}$ ). Every sixth channel is shown (channel width:  $5.2 \text{ km s}^{-1}$ ). The area shown in each panel is identical to the area shown on the next figure

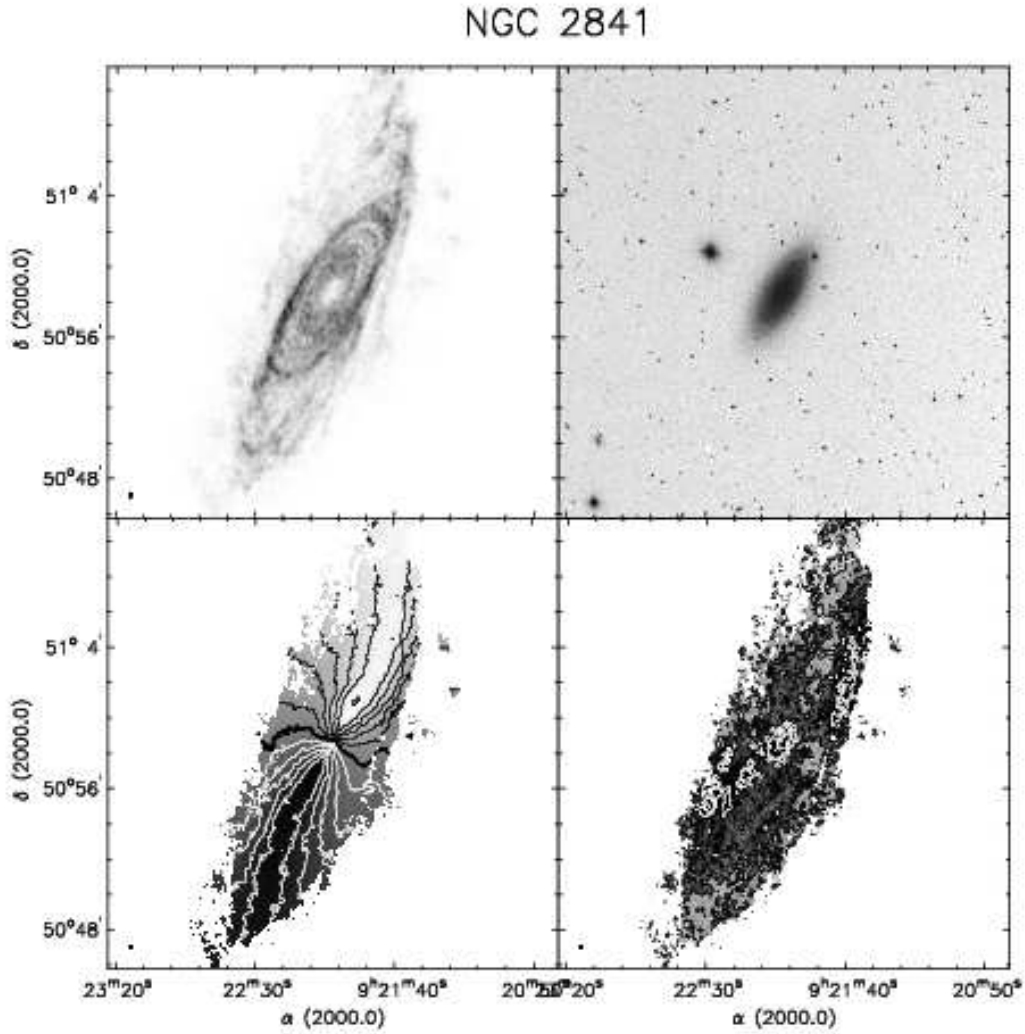


FIG. 19.— **NGC 2841**. *Top left*: integrated HI map (moment 0). Greyscale range from 0–203  $\text{Jy km s}^{-1}$ . *Top right*: Optical image from the digitized sky survey (DSS). *Bottom left*: Velocity field (moment 1). Black contours (lighter greyscale) indicate approaching emission, white contours (darker greyscale) receding emission. The thick black contour is the systemic velocity ( $v_{\text{sys}}=635.2 \text{ km s}^{-1}$ ), the iso-velocity contours are spaced by  $\Delta v=50 \text{ km s}^{-1}$ . *Bottom right*: Velocity dispersion map (moment 2). Contours are plotted at 5, 10 and  $20 \text{ km s}^{-1}$  (white contours: 50 and  $100 \text{ km s}^{-1}$ ).

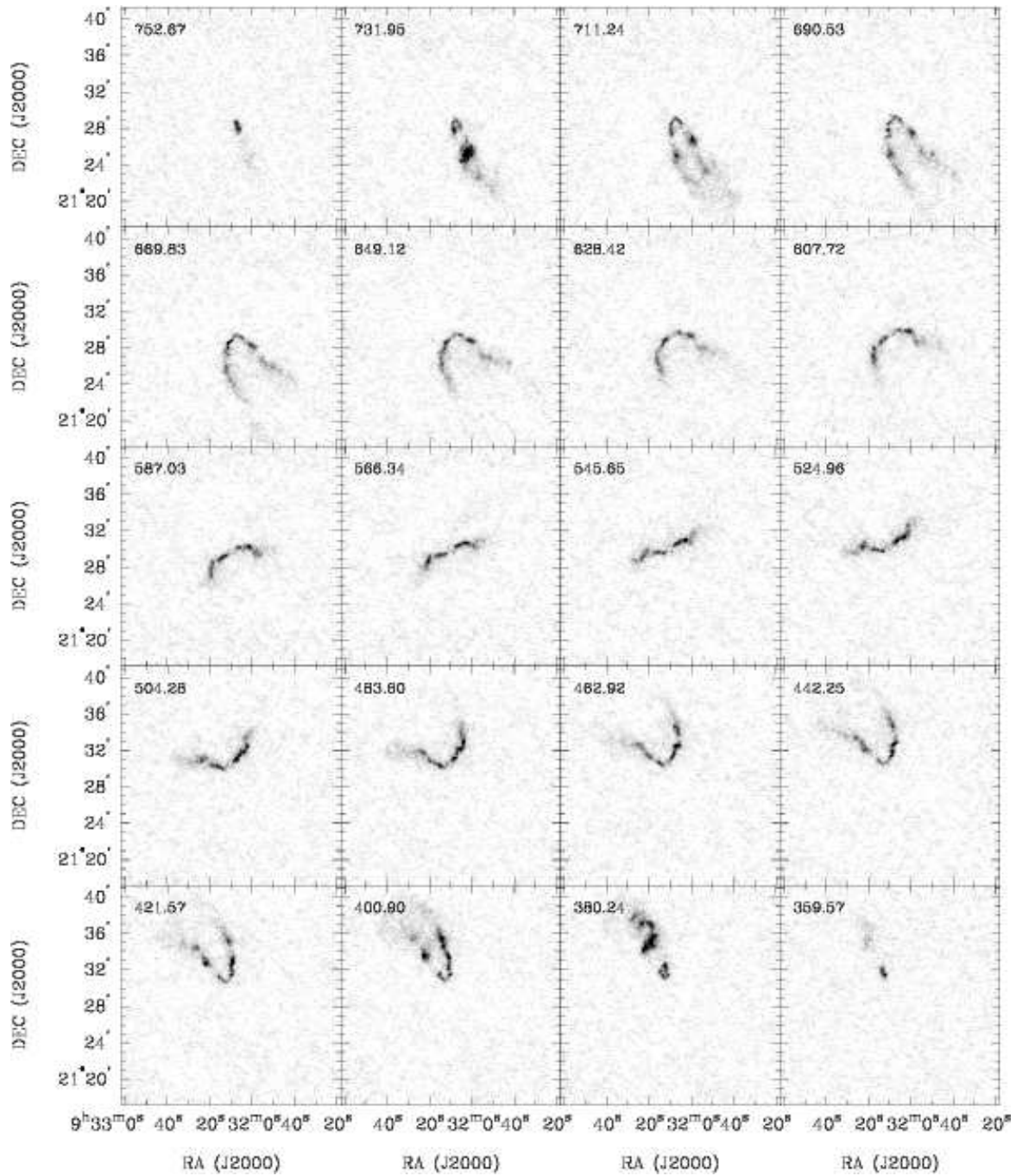


FIG. 20.— NGC 2903: Channel maps based on the NA cube (greyscale range:  $-0.02$  to  $10 \text{ mJy beam}^{-1}$ ). Every fourth channel is shown (channel width:  $5.2 \text{ km s}^{-1}$ ). The area shown in each panel is identical to the area shown on the next figure



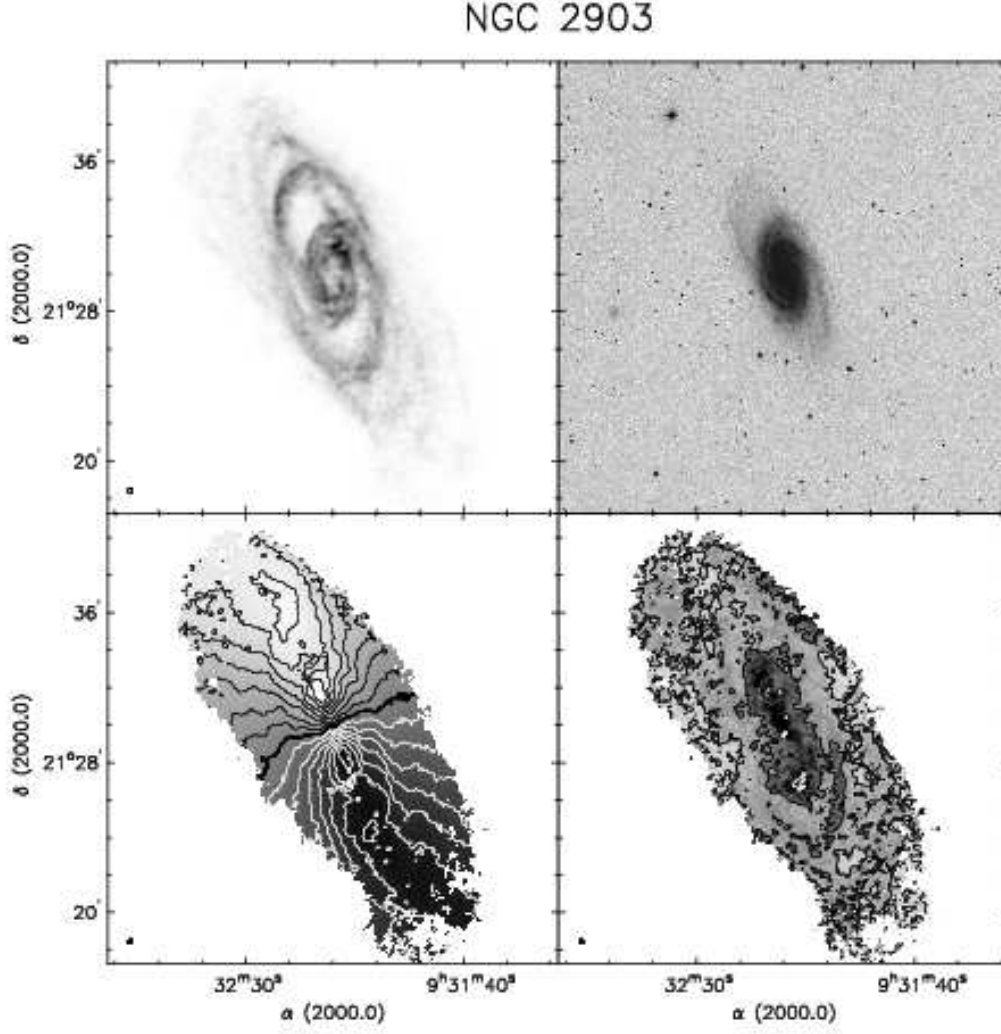


FIG. 21.— **NGC 2903**. *Top left*: integrated HI map (moment 0). Greyscale range from 0–577 Jy km s<sup>-1</sup>. *Top right*: Optical image from the digitized sky survey (DSS). *Bottom left*: Velocity field (moment 1). Black contours (lighter greyscale) indicate approaching emission, white contours (darker greyscale) receding emission. The thick black contour is the systemic velocity ( $v_{\text{sys}}=2.6$  km s<sup>-1</sup>), the iso-velocity contours are spaced by  $\Delta v=25$  km s<sup>-1</sup>. *Bottom right*: Velocity dispersion map (moment 2). Contours are plotted at 5, 10 and 20 km s<sup>-1</sup> (white contour: 50 km s<sup>-1</sup>).

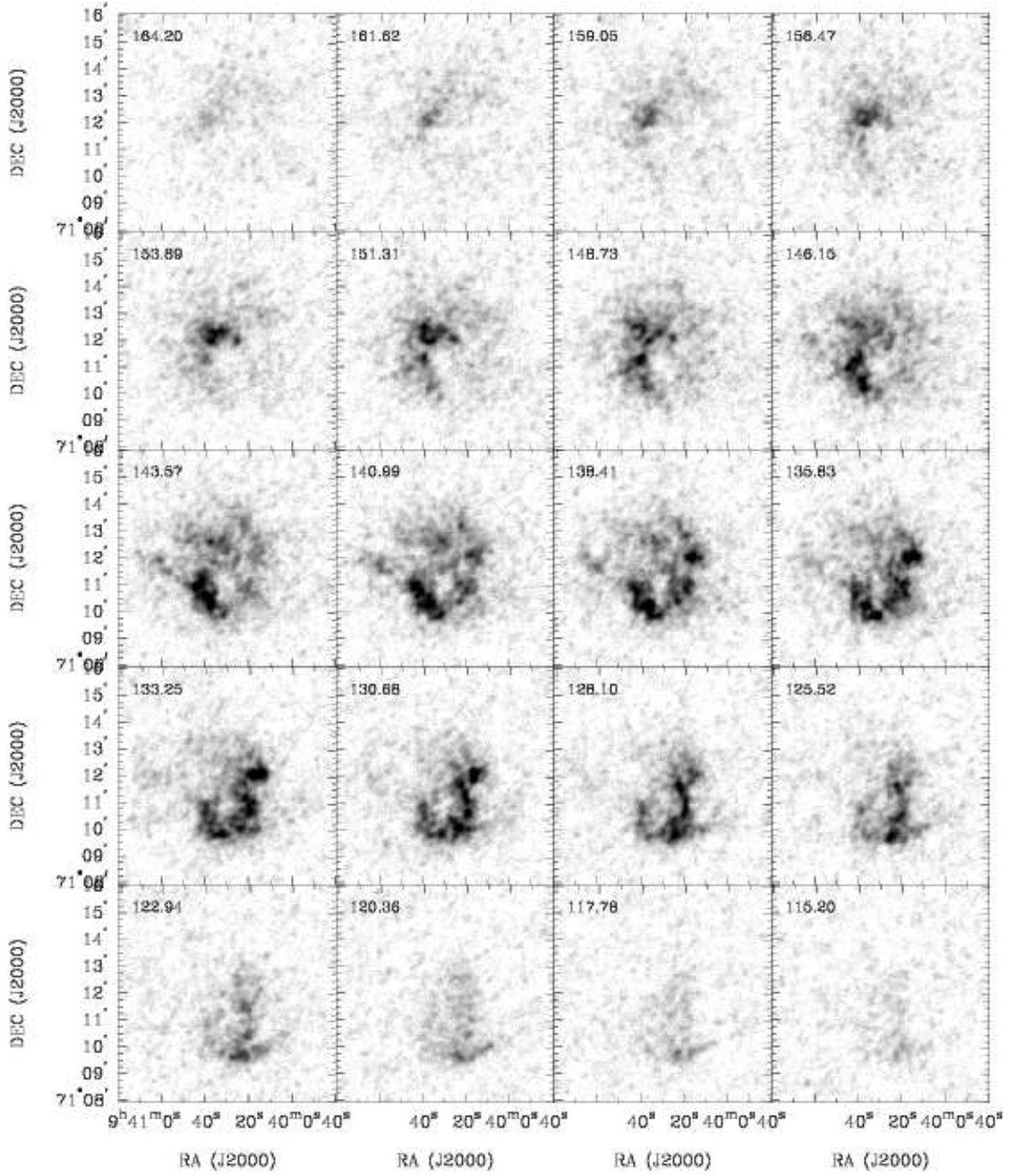


FIG. 22.— **Holmberg I**: Channel maps based on the NA cube (greyscale range:  $-0.02$  to  $15 \text{ mJy beam}^{-1}$ ). Every channel is shown (channel width:  $2.6 \text{ km s}^{-1}$ ). The area shown in each panel is identical to the area shown on the next figure

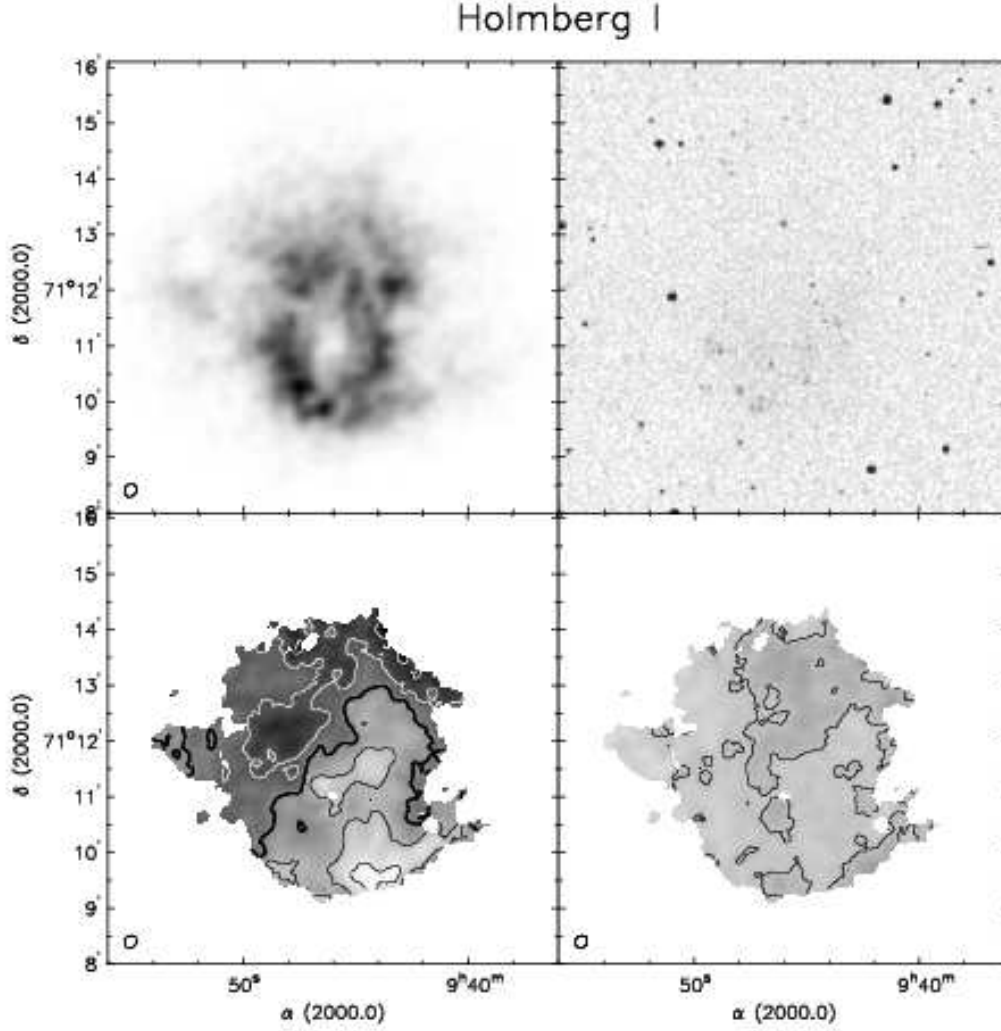


FIG. 23.— **Holmberg I**. *Top left*: integrated HI map (moment 0). Greyscale range from 0–382 Jy km s<sup>-1</sup>. *Top right*: Optical image from the digitized sky survey (DSS). *Bottom left*: Velocity field (moment 1). Black contours (lighter greyscale) indicate approaching emission, white contours (darker greyscale) receding emission. The thick black contour is the systemic velocity ( $v_{\text{sys}}=140.39$  km s<sup>-1</sup>), the iso-velocity contours are spaced by  $\Delta v=6.25$  km s<sup>-1</sup>. *Bottom right*: Velocity dispersion map (moment 2). A contour is plotted at 5.0 km s<sup>-1</sup>.

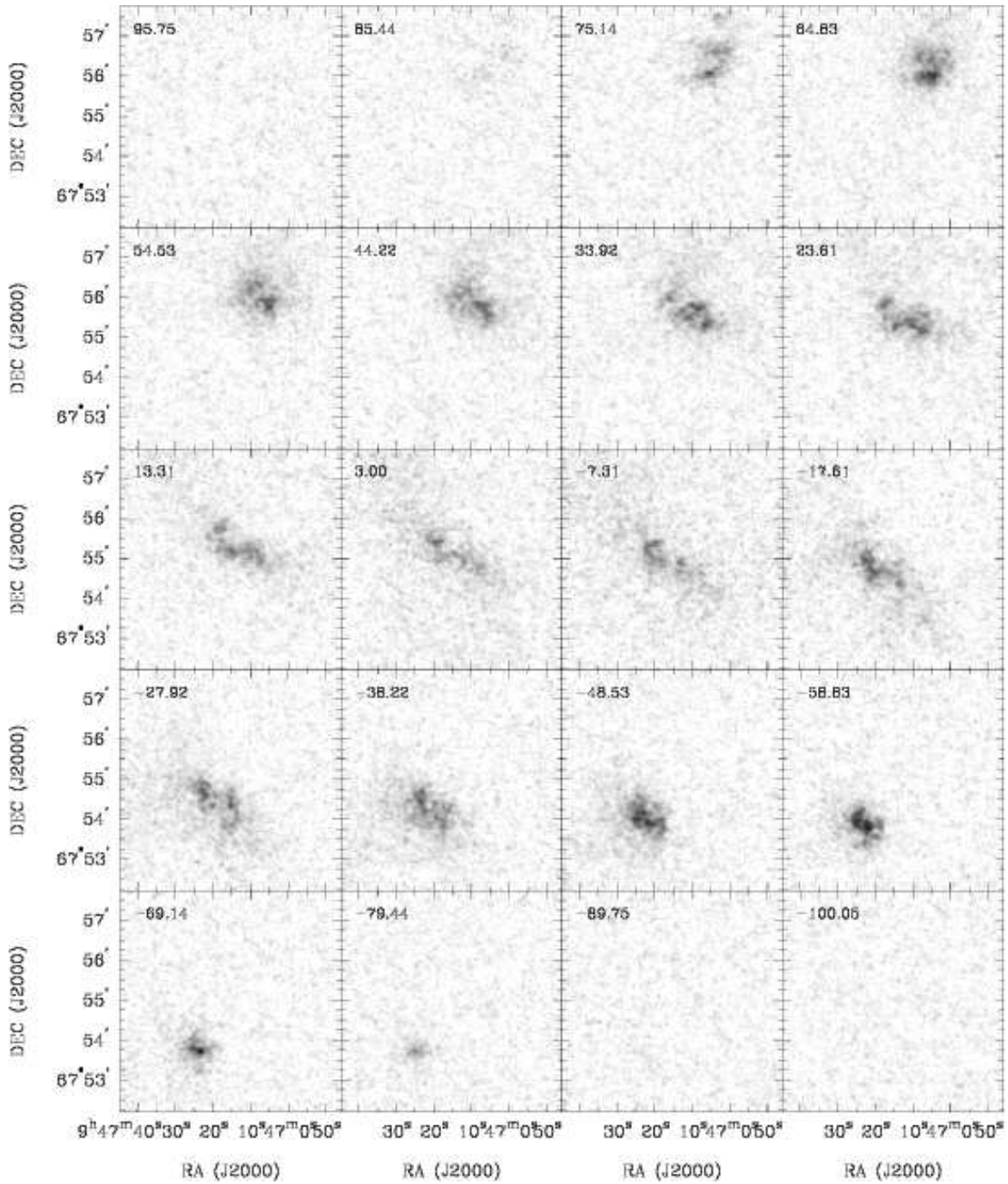


FIG. 24.— **NGC 2976**: Channel maps based on the NA cube (greyscale range:  $-0.02$  to  $8 \text{ mJy beam}^{-1}$ ). Every second channel is shown (channel width:  $5.2 \text{ km s}^{-1}$ ). The area shown in each panel is identical to the area shown on the next figure

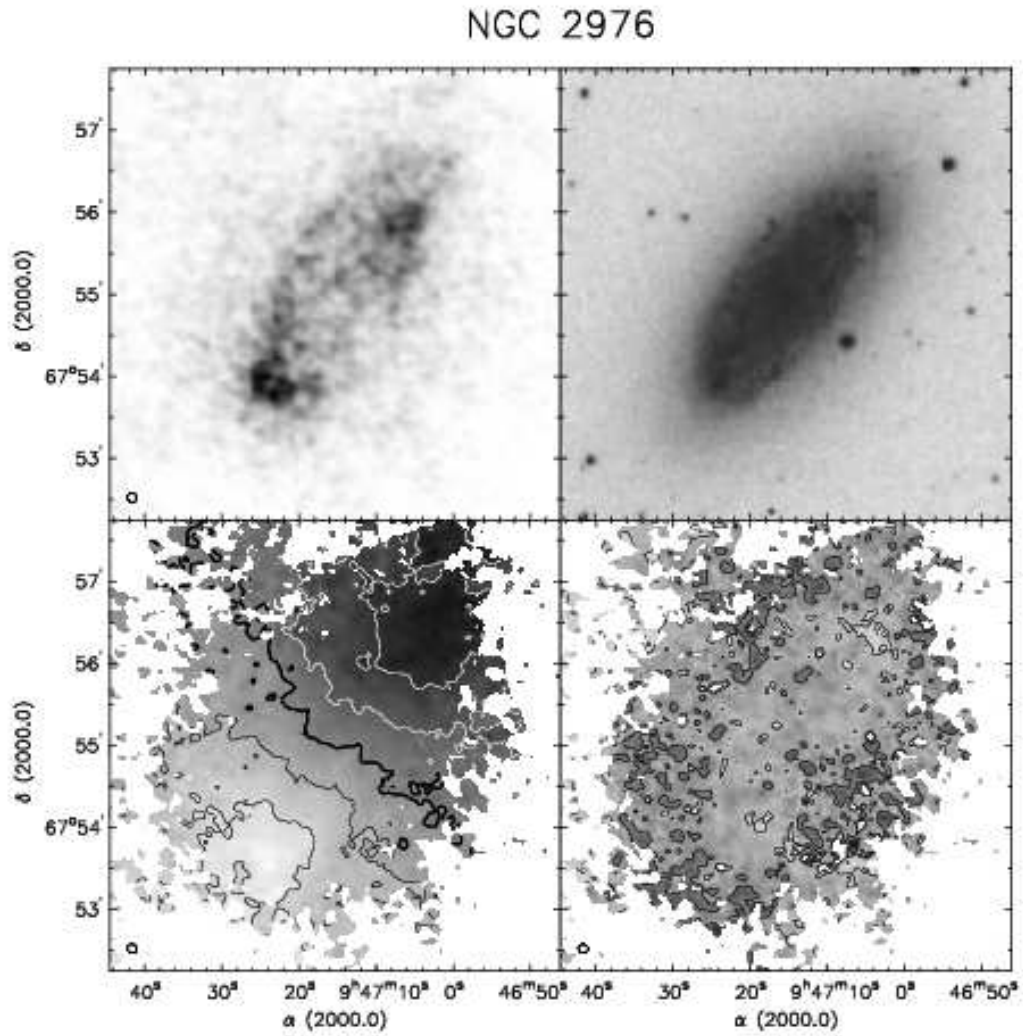


FIG. 25.— **NGC 2976**. *Top left*: integrated HI map (moment 0). Greyscale range from 0–192  $\text{Jy km s}^{-1}$ . *Top right*: Optical image from the digitized sky survey (DSS). *Bottom left*: Velocity field (moment 1). Black contours (lighter greyscale) indicate approaching emission, white contours (darker greyscale) receding emission. The thick black contour is the systemic velocity ( $v_{\text{sys}}=2.60 \text{ km s}^{-1}$ ), the iso-velocity contours are spaced by  $\Delta v=25 \text{ km s}^{-1}$ . *Bottom right*: Velocity dispersion map (moment 2). Contours are plotted at 5, 10  $\text{km s}^{-1}$ .

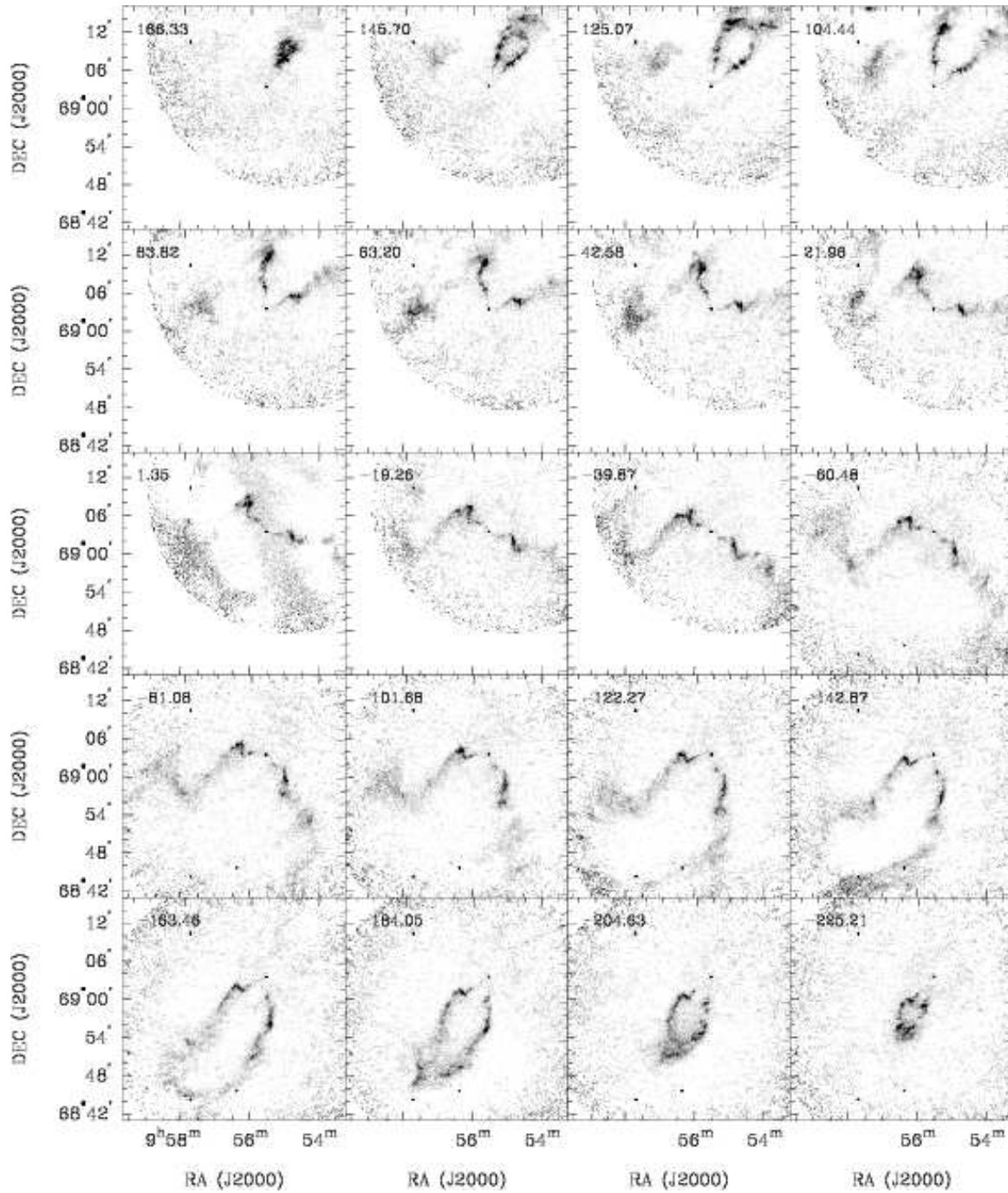


FIG. 26.— **NGC 3031**: Channel maps based on the NA cube (greyscale range:  $-0.02$  to  $10$  mJy beam<sup>-1</sup>). Every eighth channel is shown (channel width:  $2.6$  km s<sup>-1</sup>). The area shown in each panel is identical to the area shown on the next figure

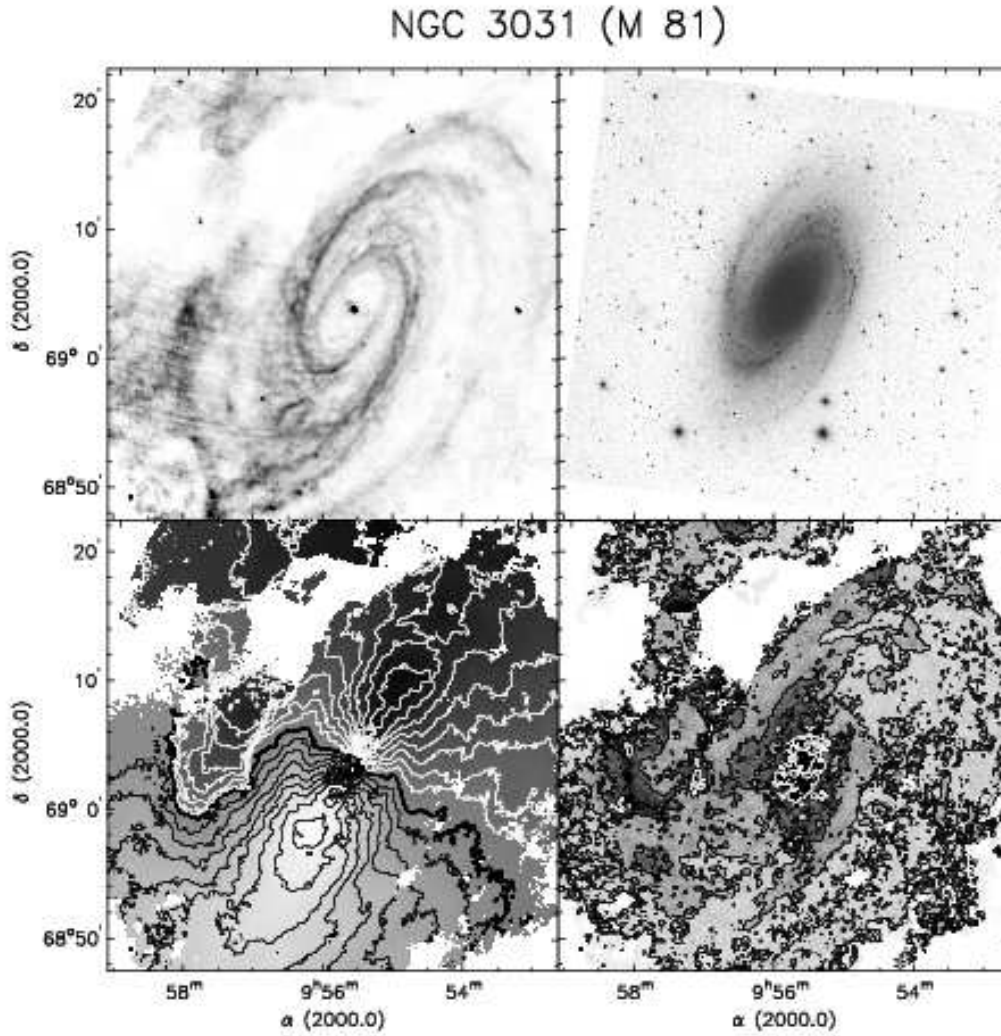


FIG. 27.— NGC 3031. *Top left*: integrated HI map (moment 0). Greyscale range from 0–700  $\text{Jy km s}^{-1}$ . Note that the continuum (point sources) have not been subtracted. *Top right*: Optical image from the digitized sky survey (DSS). *Bottom left*: Velocity field (moment 1). Black contours (lighter greyscale) indicate approaching emission, white contours (darker greyscale) receding emission. The thick black contour is the systemic velocity ( $v_{\text{sys}} = -39.4 \text{ km s}^{-1}$ ), the iso-velocity contours are spaced by  $\Delta v = 25 \text{ km s}^{-1}$ . *Bottom right*: Velocity dispersion map (moment 2). Contours are plotted at 5, 10 and 20  $\text{km s}^{-1}$  (white contours: 50 and 100  $\text{km s}^{-1}$ ).

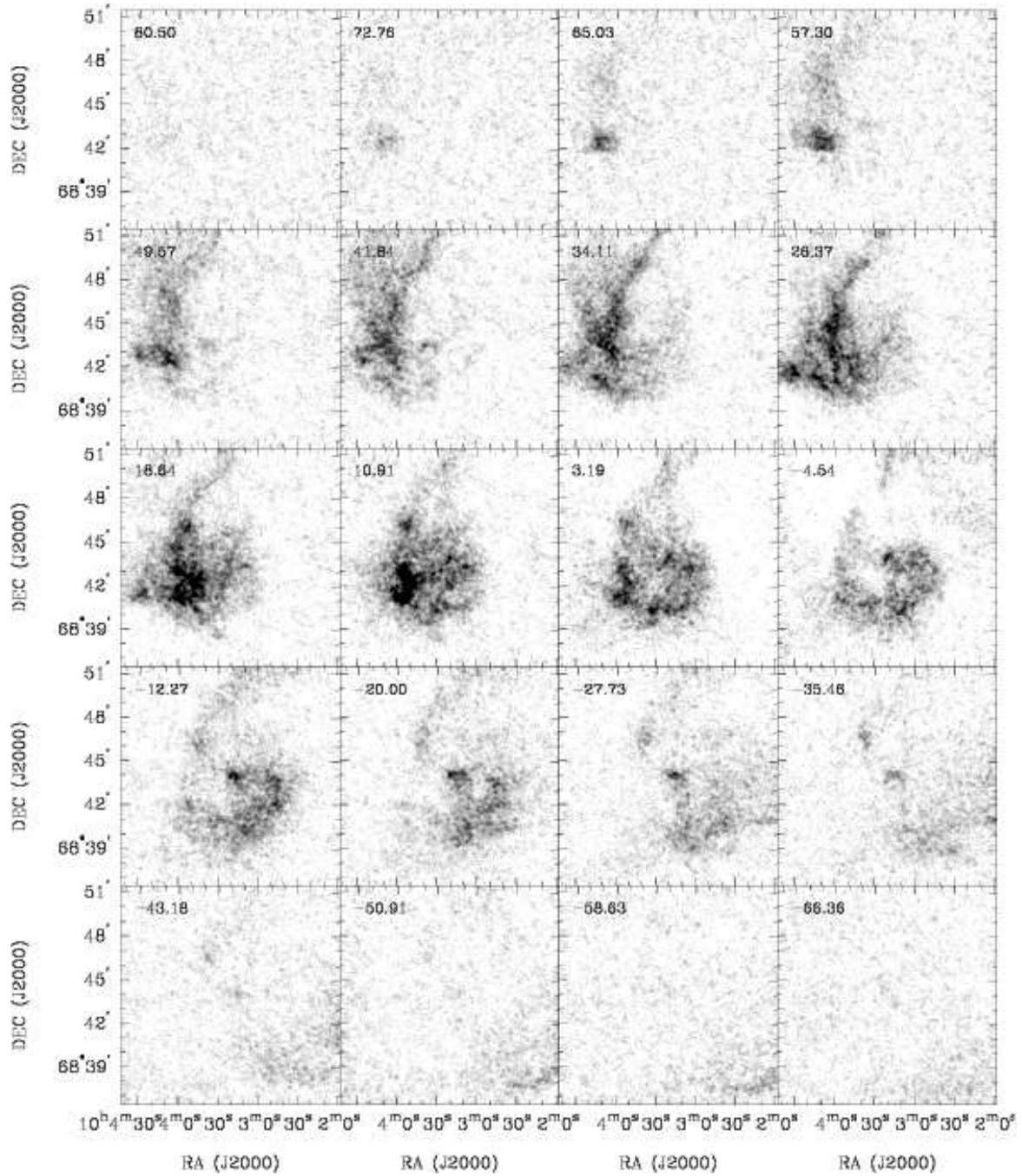


FIG. 28.— **NGC 3077**: Channel maps based on the NA cube (greyscale range:  $-0.02$  to  $10 \text{ mJy beam}^{-1}$ ). Every third channel is shown (channel width:  $2.6 \text{ km s}^{-1}$ ). The area shown in each panel is identical to the area shown on the next figure



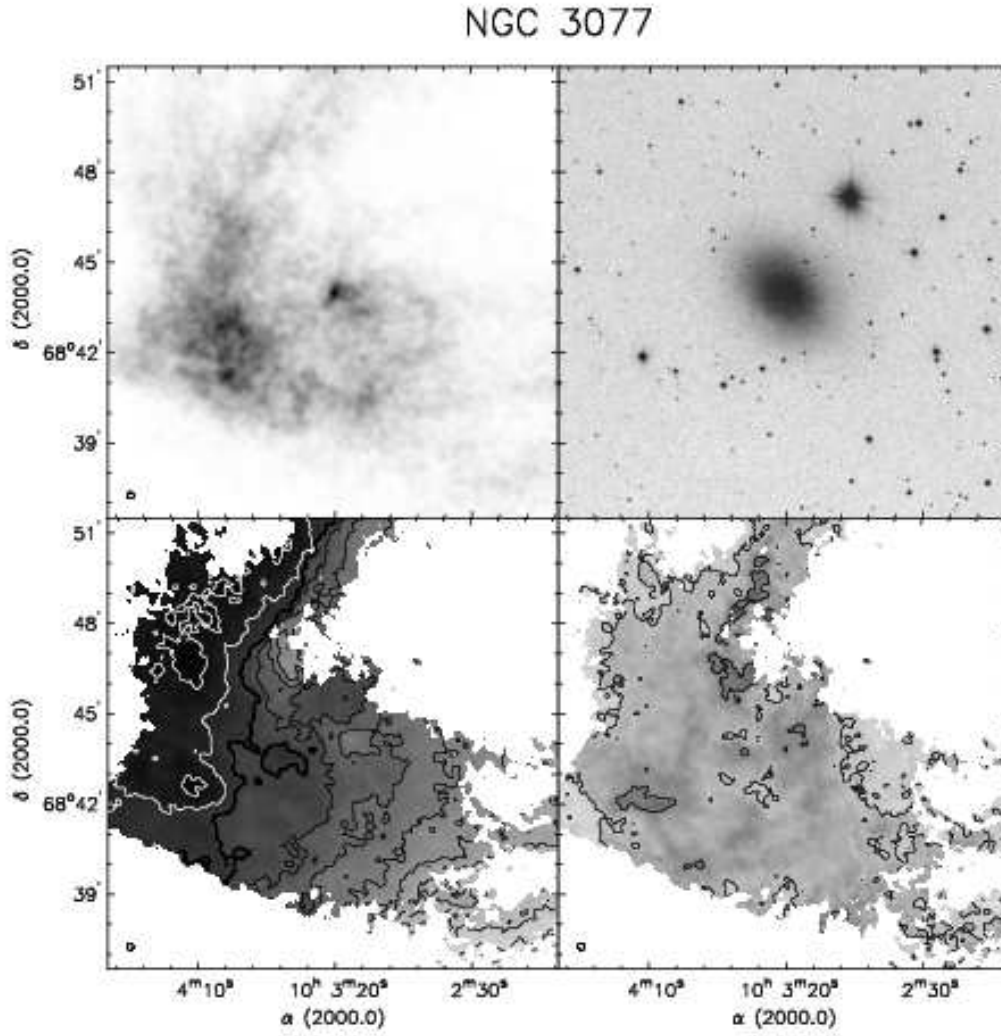


FIG. 29.— **NGC 3077**. *Top left*: integrated HI map (moment 0). Greyscale range from 0–529  $\text{Jy km s}^{-1}$ . *Top right*: Optical image from the digitized sky survey (DSS). *Bottom left*: Velocity field (moment 1). Black contours (lighter greyscale) indicate approaching emission, white contours (darker greyscale) receding emission. The thick black contour is the systemic velocity ( $v_{\text{sys}}=19.8 \text{ km s}^{-1}$ ), the iso-velocity contours are spaced by  $\Delta v=12.5 \text{ km s}^{-1}$ . *Bottom right*: Velocity dispersion map (moment 2). Contours are plotted at 5 and 10  $\text{km s}^{-1}$ .

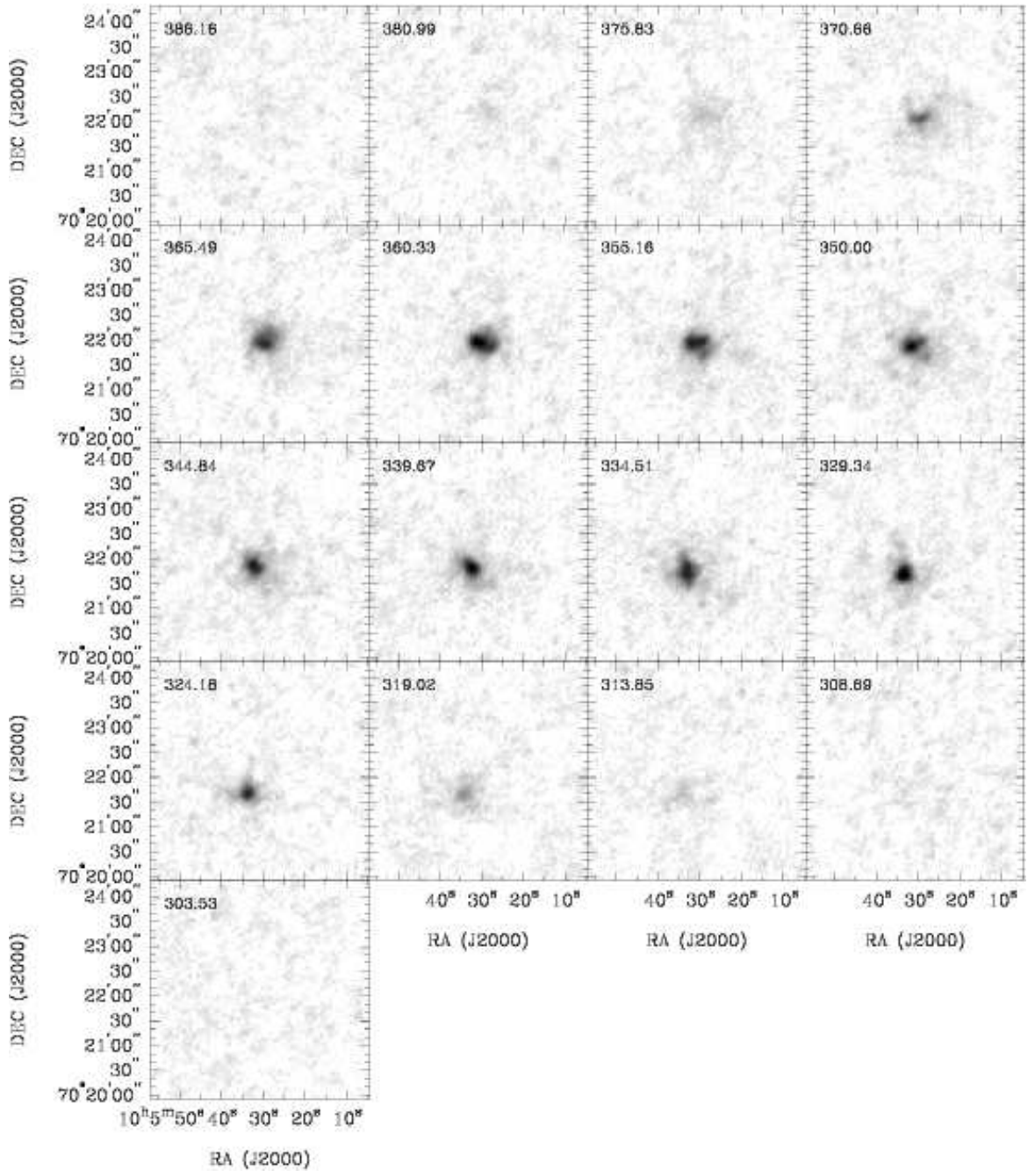


FIG. 30.— **M 81 dwarf B**: Channel maps based on the NA cube (greyscale range:  $-0.02$  to  $12 \text{ mJy beam}^{-1}$ ). Every second channel is shown (channel width:  $2.6 \text{ km s}^{-1}$ ). The area shown in each panel is identical to the area shown on the next figure.

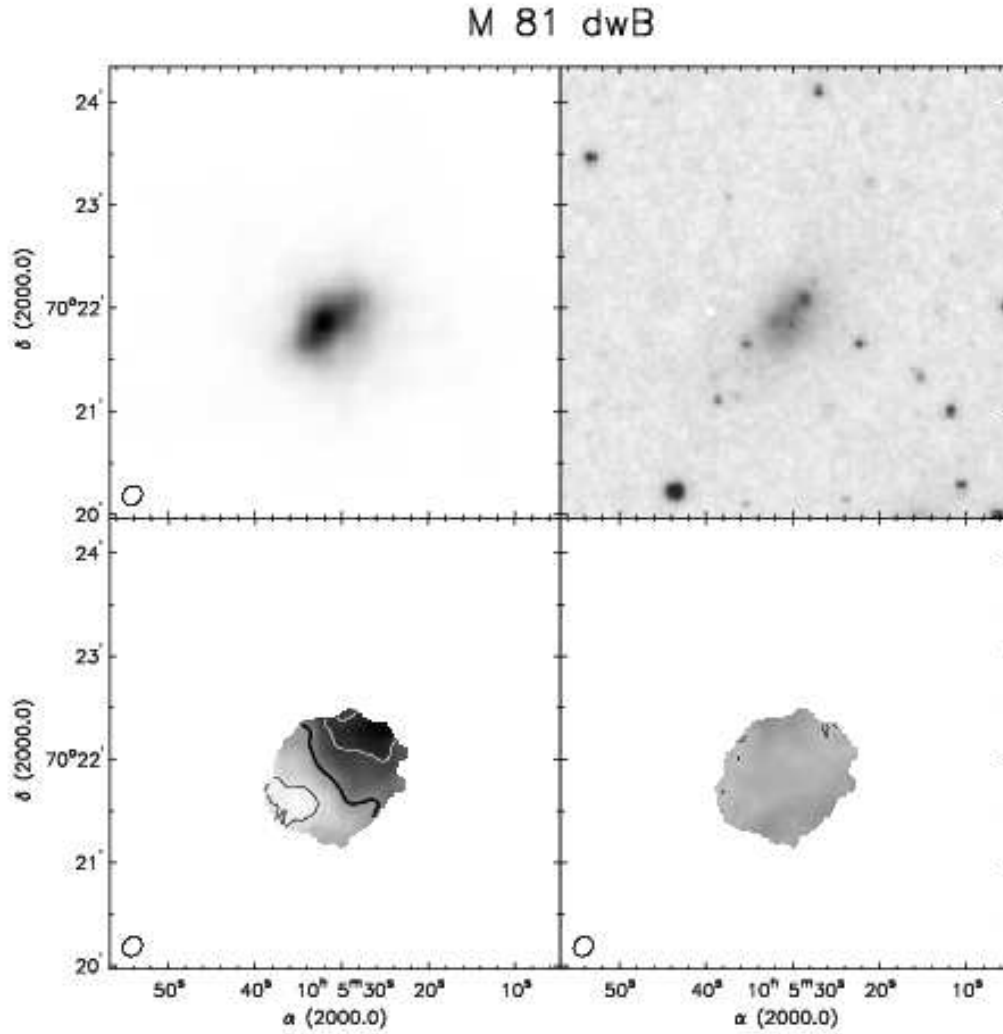


FIG. 31.— **M 81 dwarf B.** *Top left:* integrated HI map (moment 0). Greyscale range from 0–364  $\text{Jy km s}^{-1}$ . *Top right:* Optical image from the digitized sky survey (DSS). *Bottom left:* Velocity field (moment 1). Black contours (lighter greyscale) indicate approaching emission, white contours (darker greyscale) receding emission. The thick black contour is the systemic velocity ( $v_{\text{sys}}=346.41 \text{ km s}^{-1}$ ), the iso-velocity contours are spaced by  $\Delta v=12.50 \text{ km s}^{-1}$ . *Bottom right:* Velocity dispersion map (moment 2). A contours is plotted at  $5.0 \text{ km s}^{-1}$ .

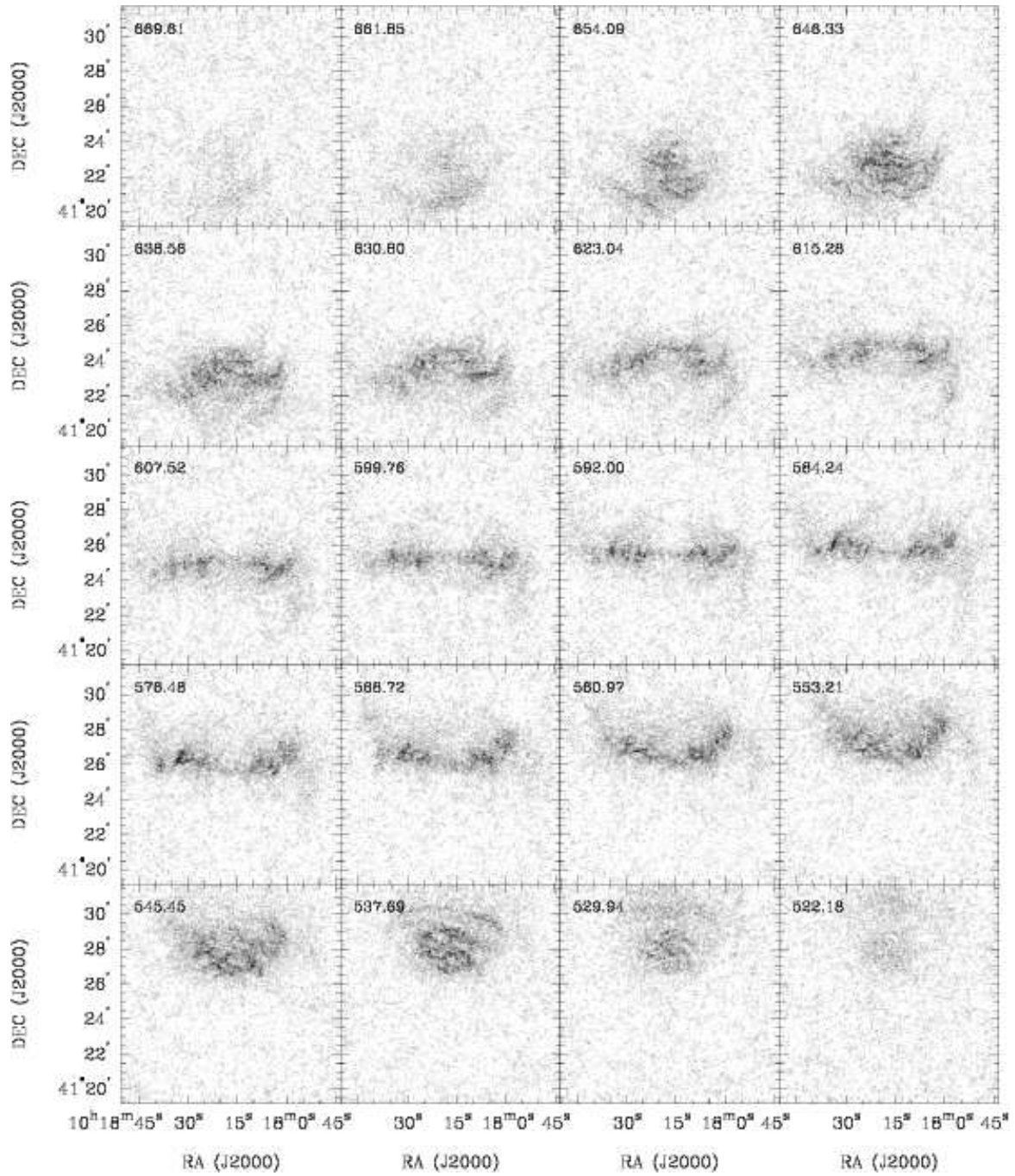


FIG. 32.— **NGC 3184**: Channel maps based on the NA cube (greyscale range:  $-0.02$  to  $5 \text{ mJy beam}^{-1}$ ). Every third channel is shown (channel width:  $5.2 \text{ km s}^{-1}$ ). The area shown in each panel is identical to the area shown on the next figure

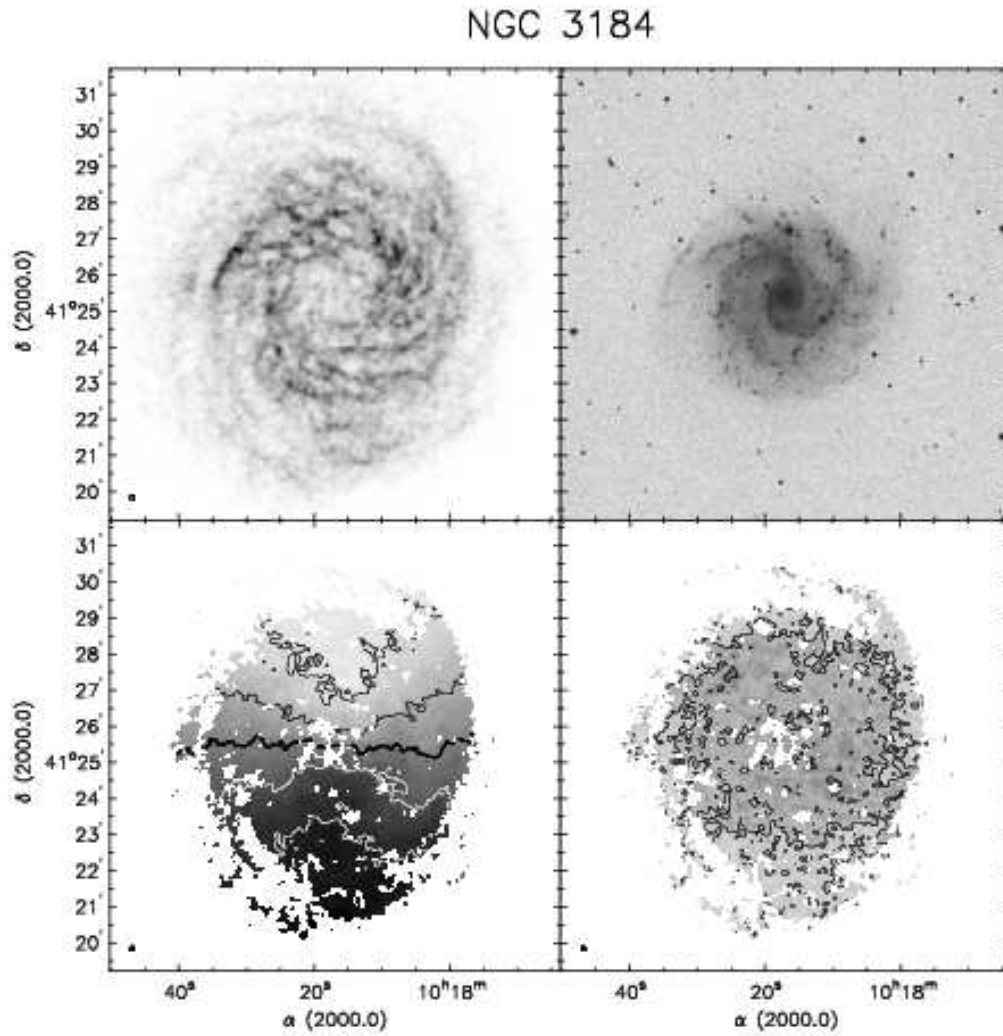


FIG. 33.— **NGC 3184.** *Top left:* integrated HI map (moment 0). Greyscale range from 0–95  $\text{Jy km s}^{-1}$ . *Top right:* Optical image from the digitized sky survey (DSS). *Bottom left:* Velocity field (moment 1). Black contours (lighter greyscale) indicate approaching emission, white contours (darker greyscale) receding emission. The thick black contour is the systemic velocity ( $v_{\text{sys}}=593.3 \text{ km s}^{-1}$ ), the iso-velocity contours are spaced by  $\Delta v=25 \text{ km s}^{-1}$ . *Bottom right:* Velocity dispersion map (moment 2). Contours are plotted at 5 and 10  $\text{km s}^{-1}$ .

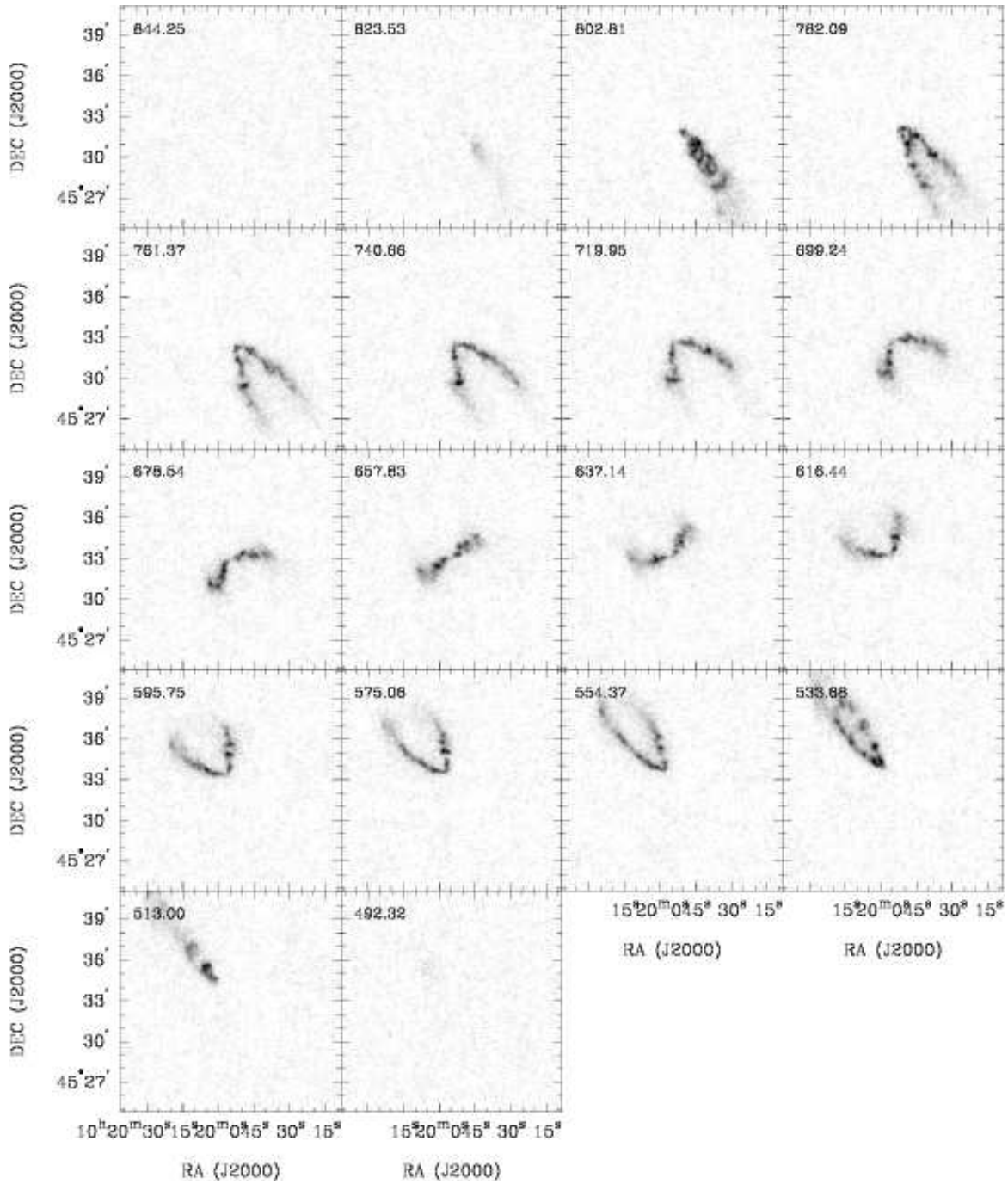


FIG. 34.— **NGC 3198**: Channel maps based on the NA cube (greyscale range:  $-0.02$  to  $12 \text{ mJy beam}^{-1}$ ). Every fourth channel is shown (channel width:  $5.2 \text{ km s}^{-1}$ ). The area shown in each panel is identical to the area shown on the next figure

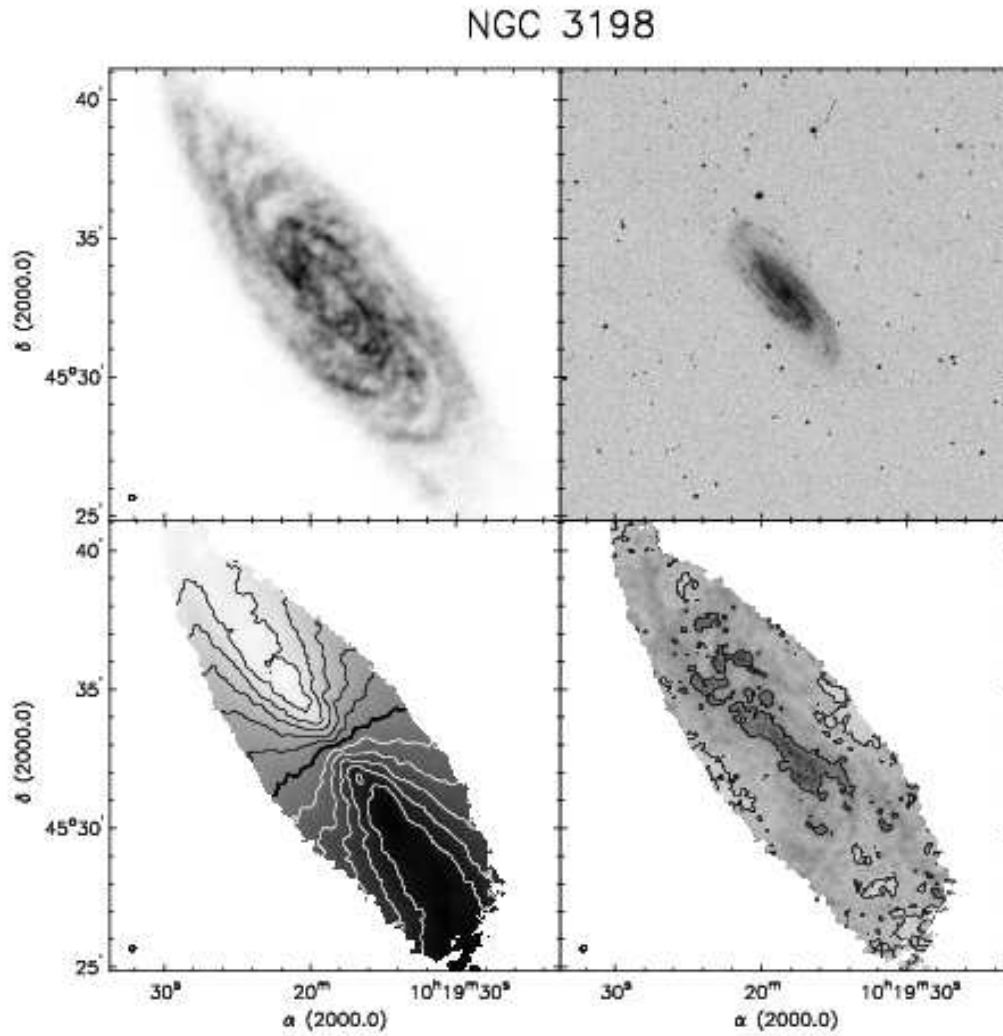


FIG. 35.— **NGC 3198.** *Top left:* integrated HI map (moment 0). Greyscale range from 0–421  $\text{Jy km s}^{-1}$ . *Top right:* Optical image from the digitized sky survey (DSS). *Bottom left:* Velocity field (moment 1). Black contours (lighter greyscale) indicate approaching emission, white contours (darker greyscale) receding emission. The thick black contour is the systemic velocity ( $v_{\text{sys}} = 661.2 \text{ km s}^{-1}$ ), the iso-velocity contours are spaced by  $\Delta v = 25 \text{ km s}^{-1}$ . *Bottom right:* Velocity dispersion map (moment 2). Contours are plotted at 5, 10 and 20  $\text{km s}^{-1}$ .

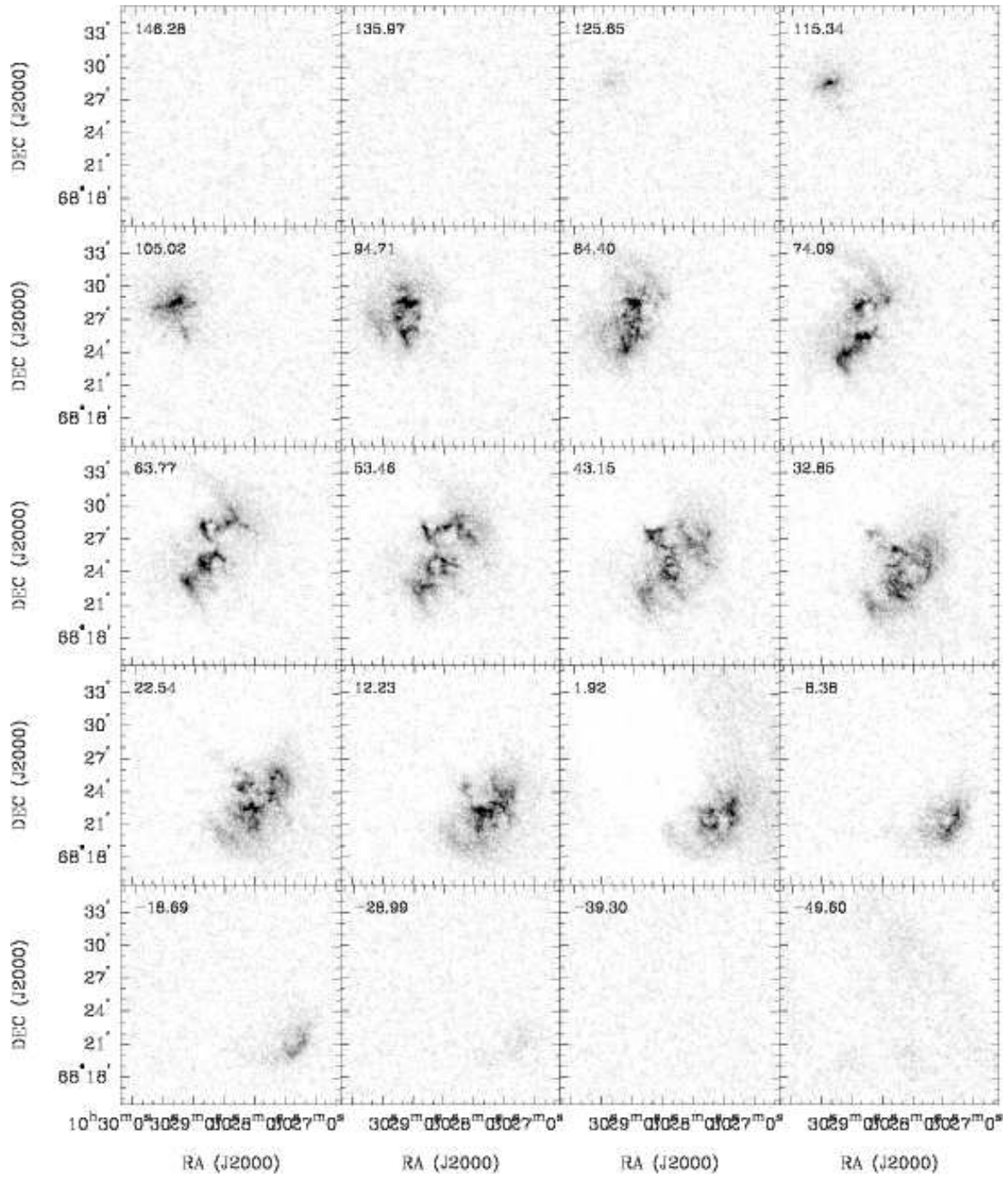


FIG. 36.— **IC 2574**: Channel maps based on the NA cube (greyscale range:  $-0.02$  to  $15 \text{ mJy beam}^{-1}$ ). Every fourth channel is shown (channel width:  $2.6 \text{ km s}^{-1}$ ). The area shown in each panel is identical to the area shown on the next figure



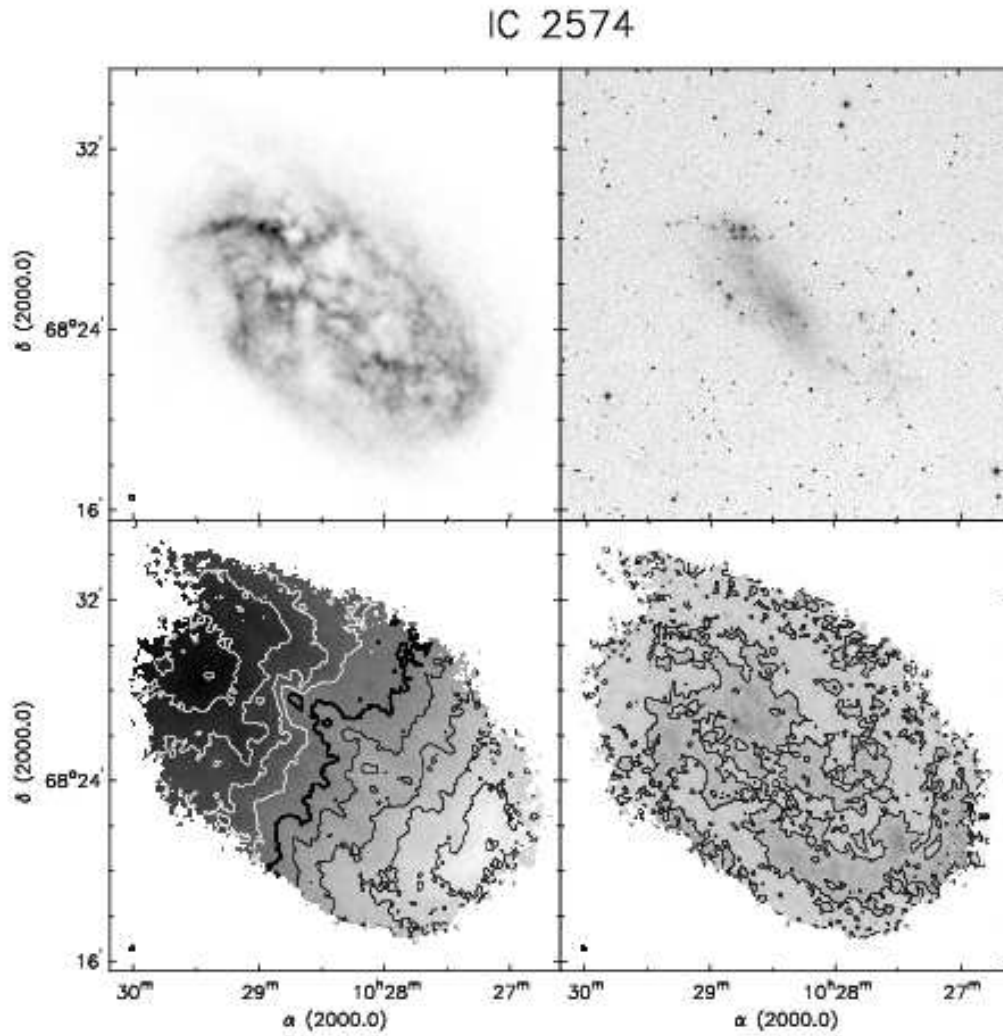


FIG. 37.— **IC 2574**. *Top left*: integrated HI map (moment 0). Greyscale range from 0–639  $\text{Jy km s}^{-1}$ . *Top right*: Optical image from the digitized sky survey (DSS). *Bottom left*: Velocity field (moment 1). Black contours (lighter greyscale) indicate approaching emission, white contours (darker greyscale) receding emission. The thick black contour is the systemic velocity ( $v_{\text{sys}}=48.6 \text{ km s}^{-1}$ ), the iso-velocity contours are spaced by  $\Delta v=12.5 \text{ km s}^{-1}$ . *Bottom right*: Velocity dispersion map (moment 2). Contours are plotted at 5 and 10  $\text{km s}^{-1}$ .

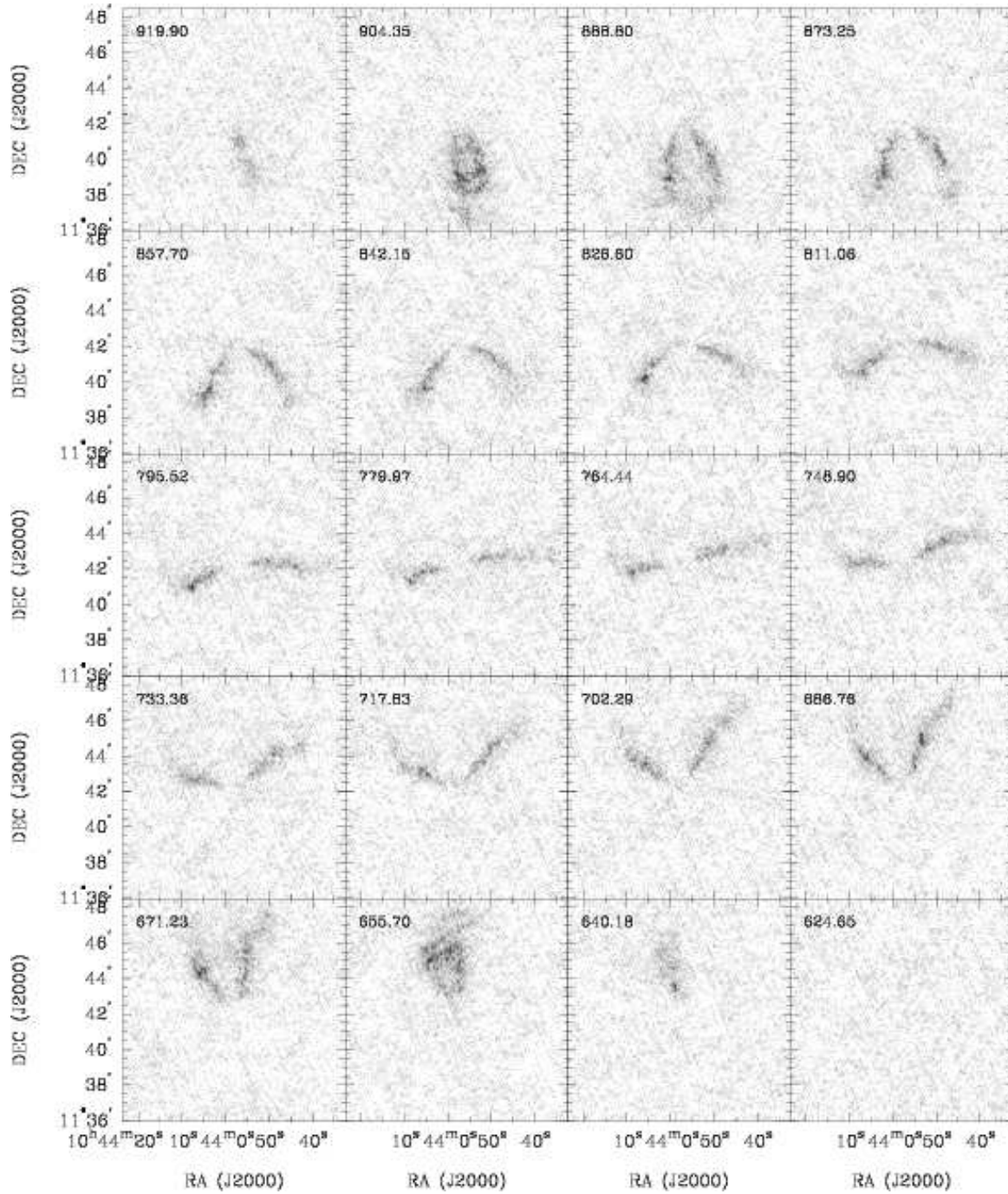


FIG. 38.— **NGC 3351**: Channel maps based on the NA cube (greyscale range:  $-0.02$  to  $5 \text{ mJy beam}^{-1}$ ). Every third channel is shown (channel width:  $5.2 \text{ km s}^{-1}$ ). The area shown in each panel is identical to the area shown on the next figure

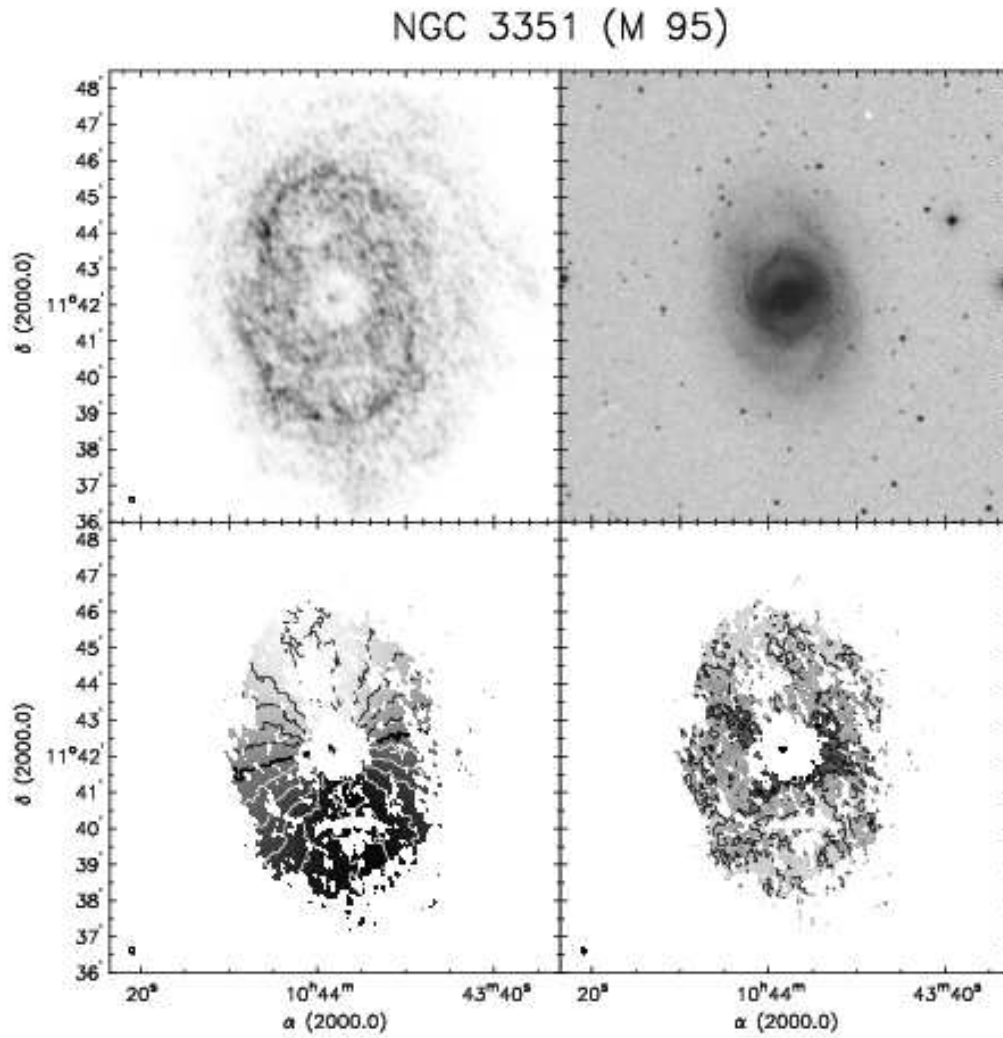


FIG. 39.— **NGC 3351**. *Top left*: integrated HI map (moment 0). Greyscale range from 0–83 Jy km s<sup>-1</sup>. *Top right*: Optical image from the digitized sky survey (DSS). *Bottom left*: Velocity field (moment 1). Black contours (lighter greyscale) indicate approaching emission, white contours (darker greyscale) receding emission. The thick black contour is the systemic velocity ( $v_{\text{sys}}=779.0$  km s<sup>-1</sup>), the iso-velocity contours are spaced by  $\Delta v=25.0$  km s<sup>-1</sup>. *Bottom right*: Velocity dispersion map (moment 2). Contours are plotted at 5, 10 and 20 km s<sup>-1</sup>.

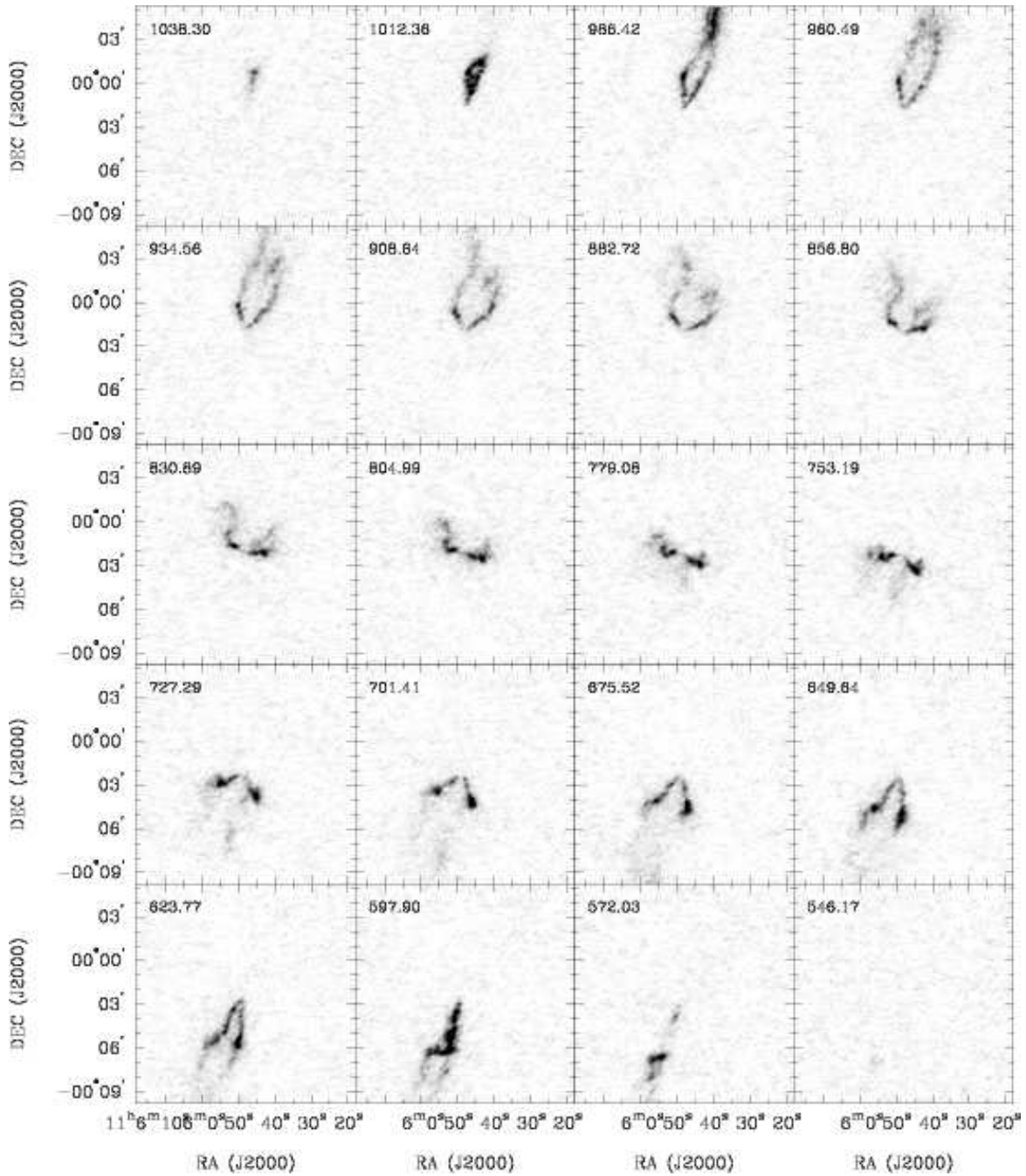


FIG. 40.— **NGC 3521**: Channel maps based on the NA cube (greyscale range:  $-0.02$  to  $12 \text{ mJy beam}^{-1}$ ). Every fifth channel is shown (channel width:  $5.2 \text{ km s}^{-1}$ ). The area shown in each panel is identical to the area shown on the next figure

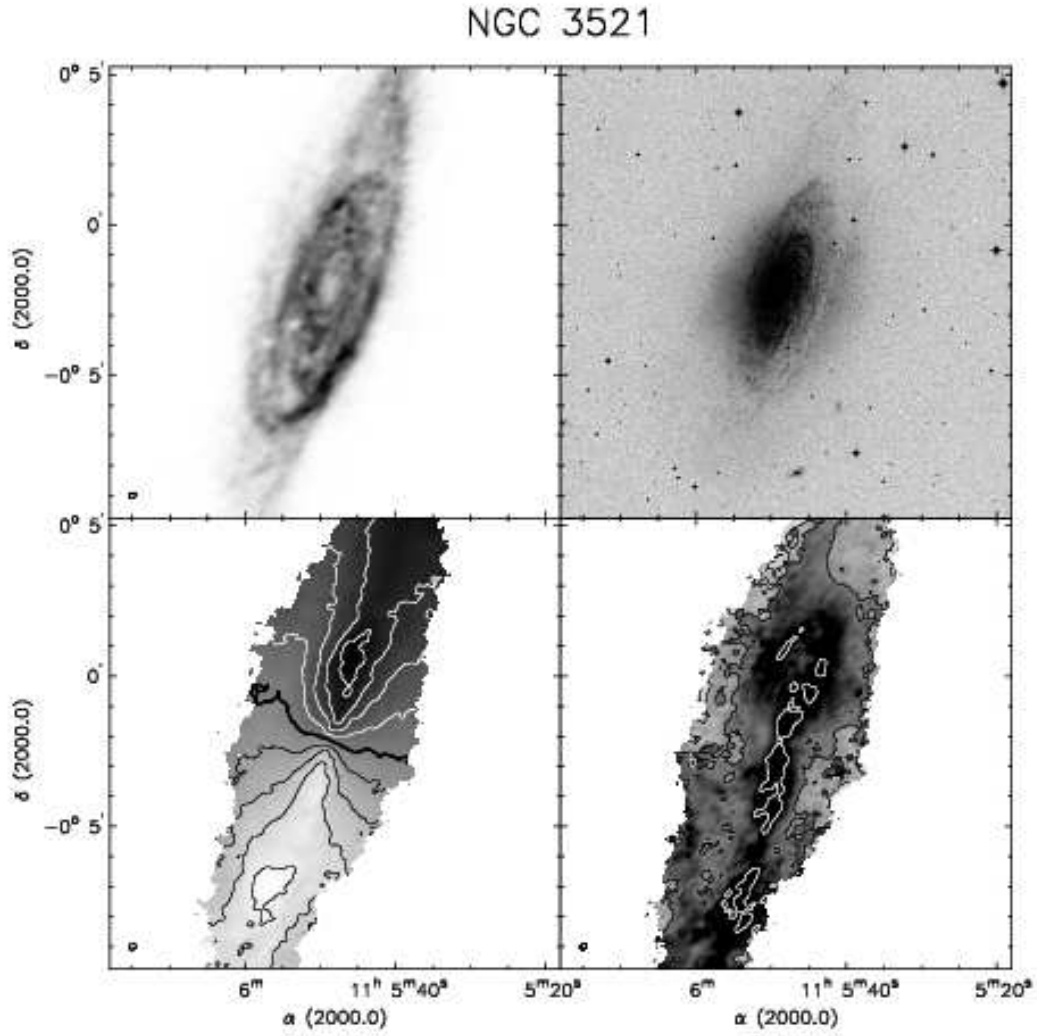


FIG. 41.— **NGC 3521**. *Top left*: integrated HI map (moment 0). Greyscale range from 0–740 Jy km s<sup>-1</sup>. *Top right*: Optical image from the digitized sky survey (DSS). *Bottom left*: Velocity field (moment 1). Black contours (lighter greyscale) indicate approaching emission, white contours (darker greyscale) receding emission. The thick black contour is the systemic velocity ( $v_{\text{sys}}=798.2$  km s<sup>-1</sup>), the iso-velocity contours are spaced by  $\Delta v=50$  km s<sup>-1</sup>. *Bottom right*: Velocity dispersion map (moment 2). Contours are plotted at 5, 10 and 20 km s<sup>-1</sup> (white contour: 50 km s<sup>-1</sup>).

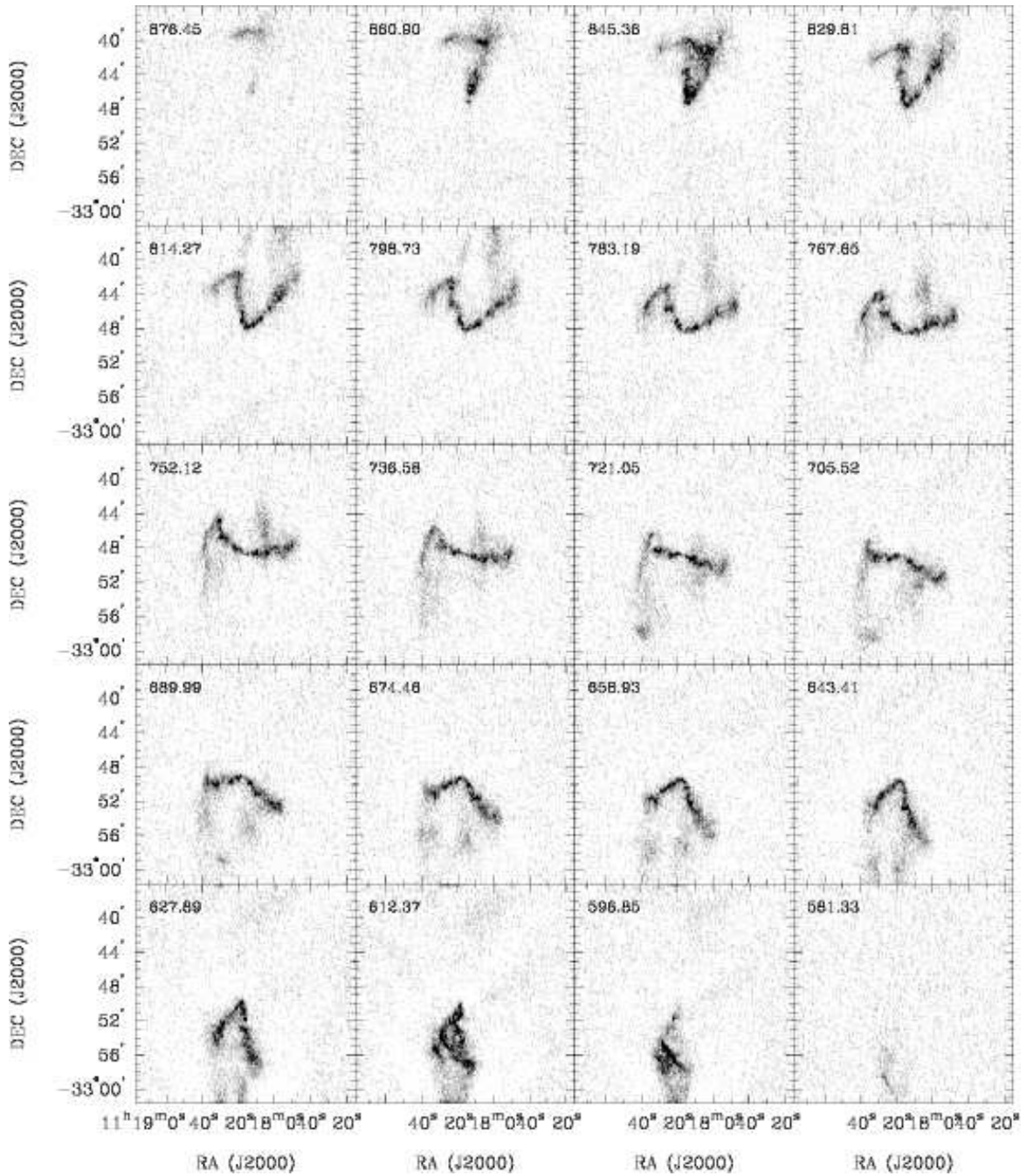


FIG. 42.— **NGC 3621**: Channel maps based on the NA cube (greyscale range:  $-0.02$  to  $10 \text{ mJy beam}^{-1}$ ). Every third channel is shown (channel width:  $5.2 \text{ km s}^{-1}$ ). The area shown in each panel is identical to the area shown on the next figure

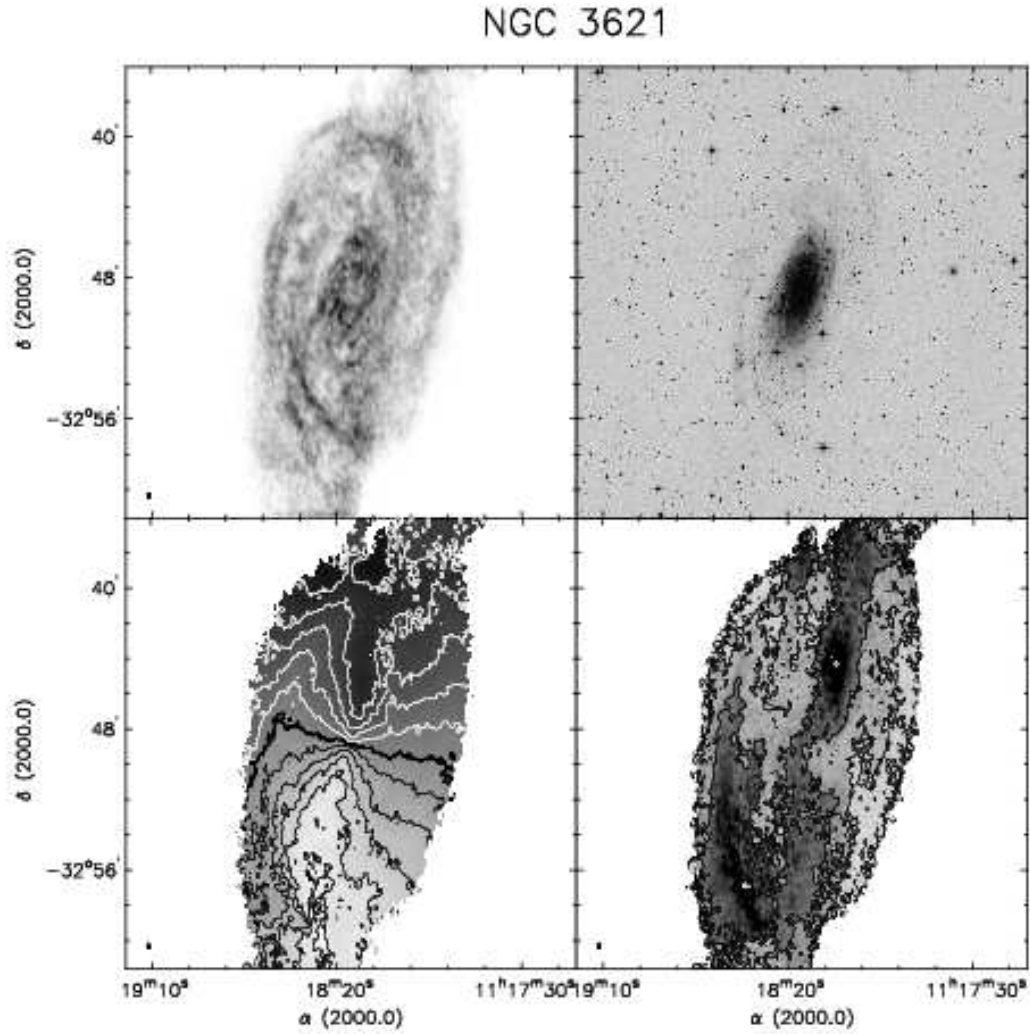


FIG. 43.— **NGC 3621**. *Top left*: integrated HI map (moment 0). Greyscale range from 0–525 Jy km s<sup>-1</sup>. *Top right*: Optical image from the digitized sky survey (DSS). *Bottom left*: Velocity field (moment 1). Black contours (lighter greyscale) indicate approaching emission, white contours (darker greyscale) receding emission. The thick black contour is the systemic velocity ( $v_{\text{sys}}=730.1$  km s<sup>-1</sup>), the iso-velocity contours are spaced by  $\Delta v=25$  km s<sup>-1</sup>. *Bottom right*: Velocity dispersion map (moment 2). Contours are plotted at 5, 10 and 20 km s<sup>-1</sup> (white contour: 50 km s<sup>-1</sup>).

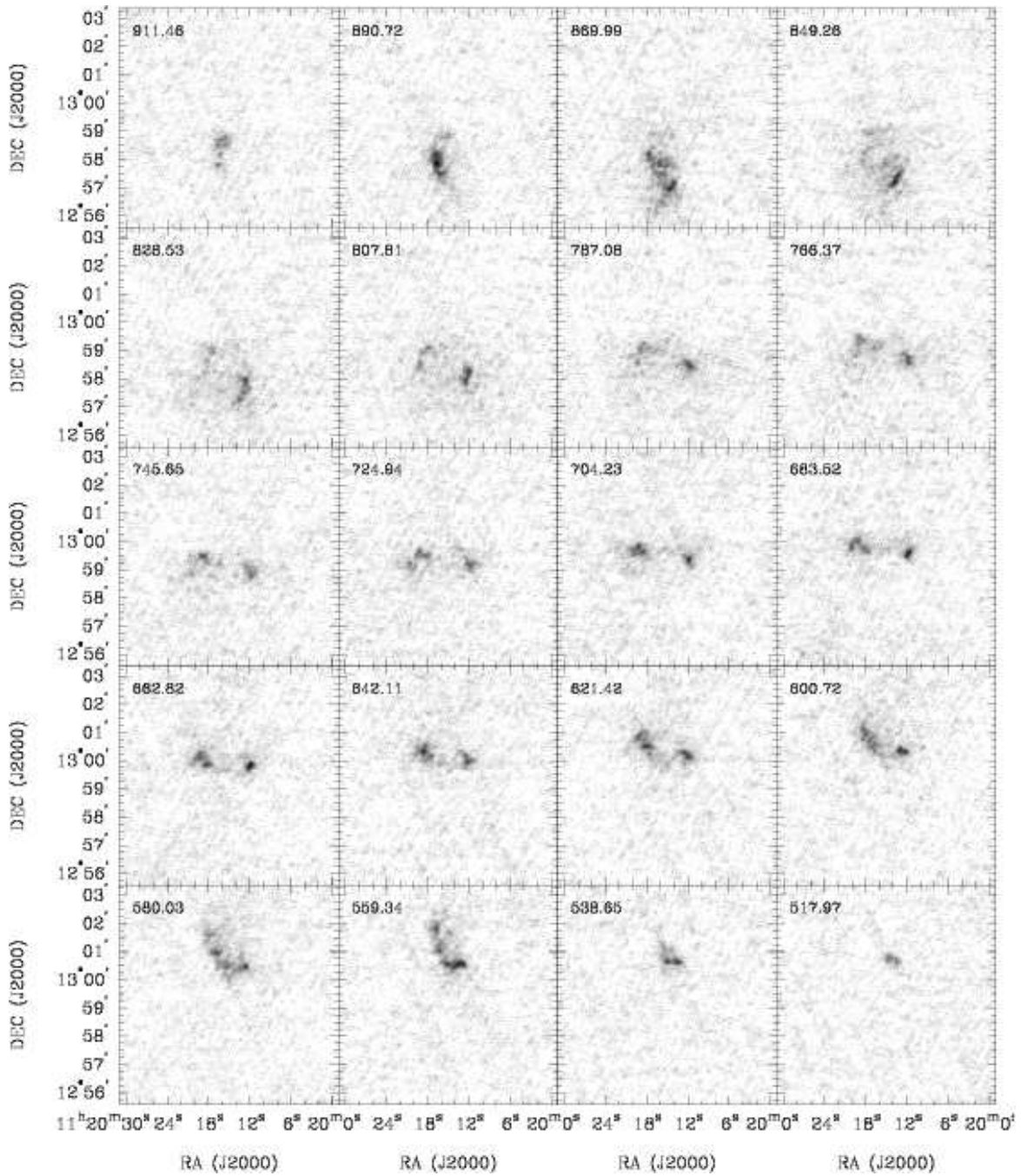


FIG. 44.— **NGC 3627**: Channel maps based on the NA cube (greyscale range:  $-0.02$  to  $7 \text{ mJy beam}^{-1}$ ). Every fourth channel is shown (channel width:  $5.2 \text{ km s}^{-1}$ ). The area shown in each panel is identical to the area shown on the next figure



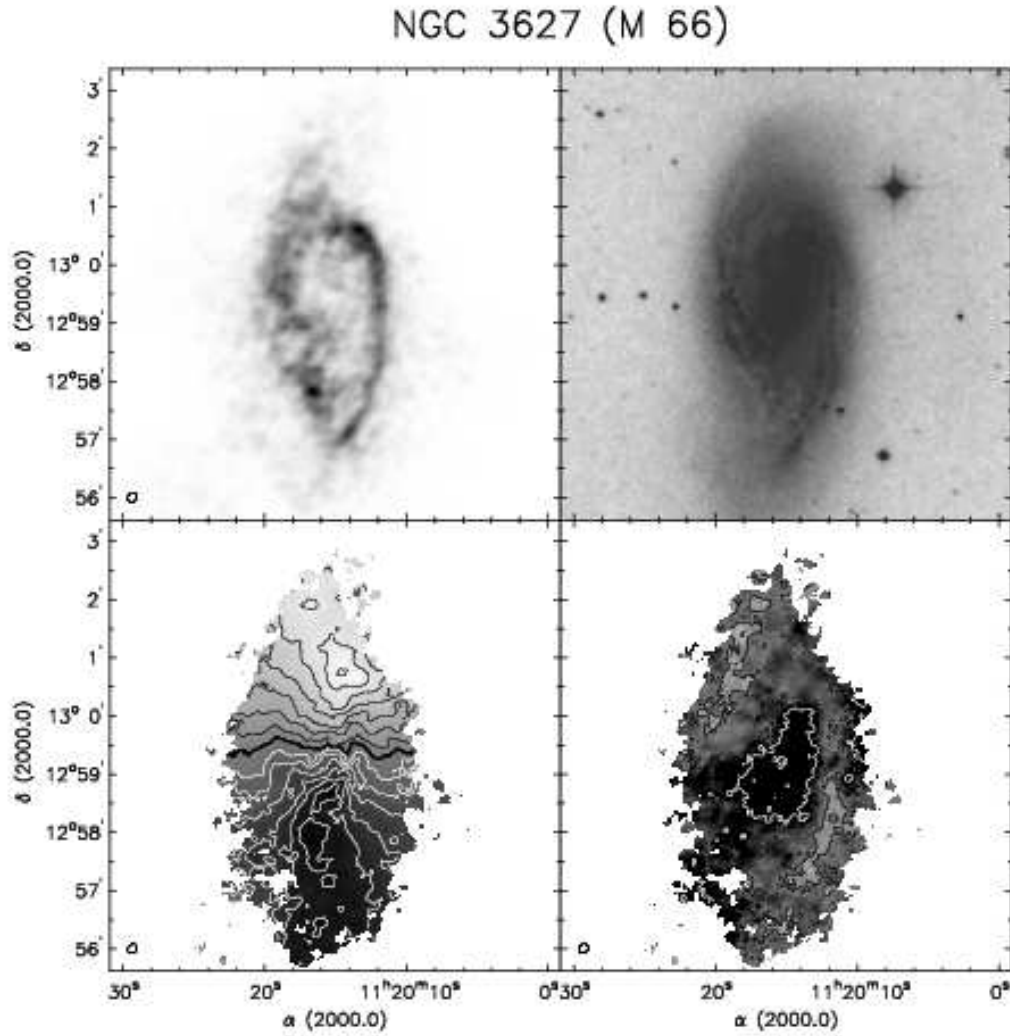


FIG. 45.— **NGC 3627**. *Top left*: integrated HI map (moment 0). Greyscale range from 0–293  $\text{Jy km s}^{-1}$ . *Top right*: Optical image from the digitized sky survey (DSS). *Bottom left*: Velocity field (moment 1). Black contours (lighter greyscale) indicate approaching emission, white contours (darker greyscale) receding emission. The thick black contour is the systemic velocity ( $v_{\text{sys}}=717.3 \text{ km s}^{-1}$ ), the iso-velocity contours are spaced by  $\Delta v=25 \text{ km s}^{-1}$ . *Bottom right*: Velocity dispersion map (moment 2). Contours are plotted at 5, 10 and  $20 \text{ km s}^{-1}$  (white contours: 50 and  $100 \text{ km s}^{-1}$ ).

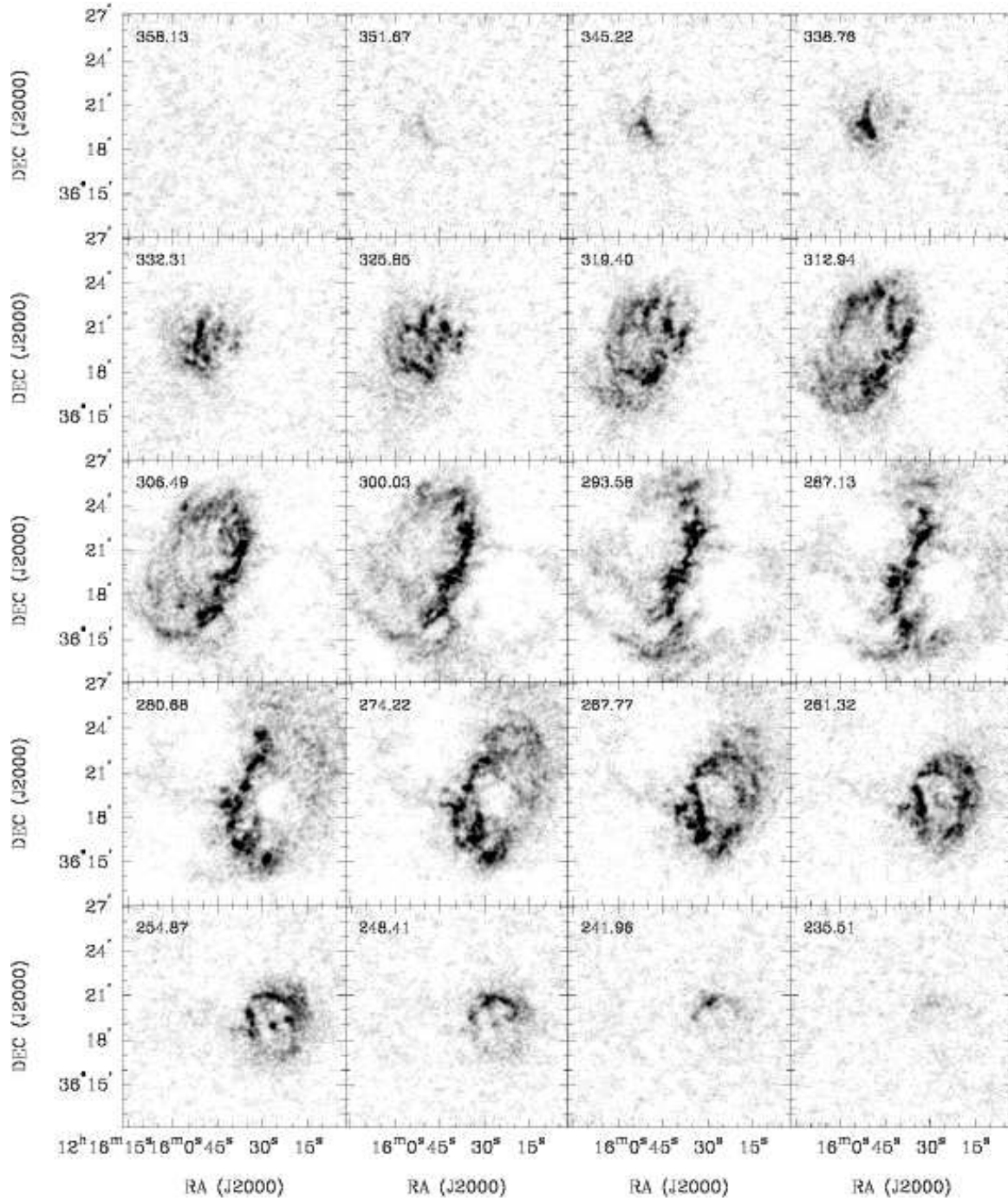


FIG. 46.— **NGC 4214**: Channel maps based on the NA cube (greyscale range:  $-0.02$  to  $10 \text{ mJy beam}^{-1}$ ). Every fifth channel is shown (channel width:  $1.3 \text{ km s}^{-1}$ ). The area shown in each panel is identical to the area shown on the next figure

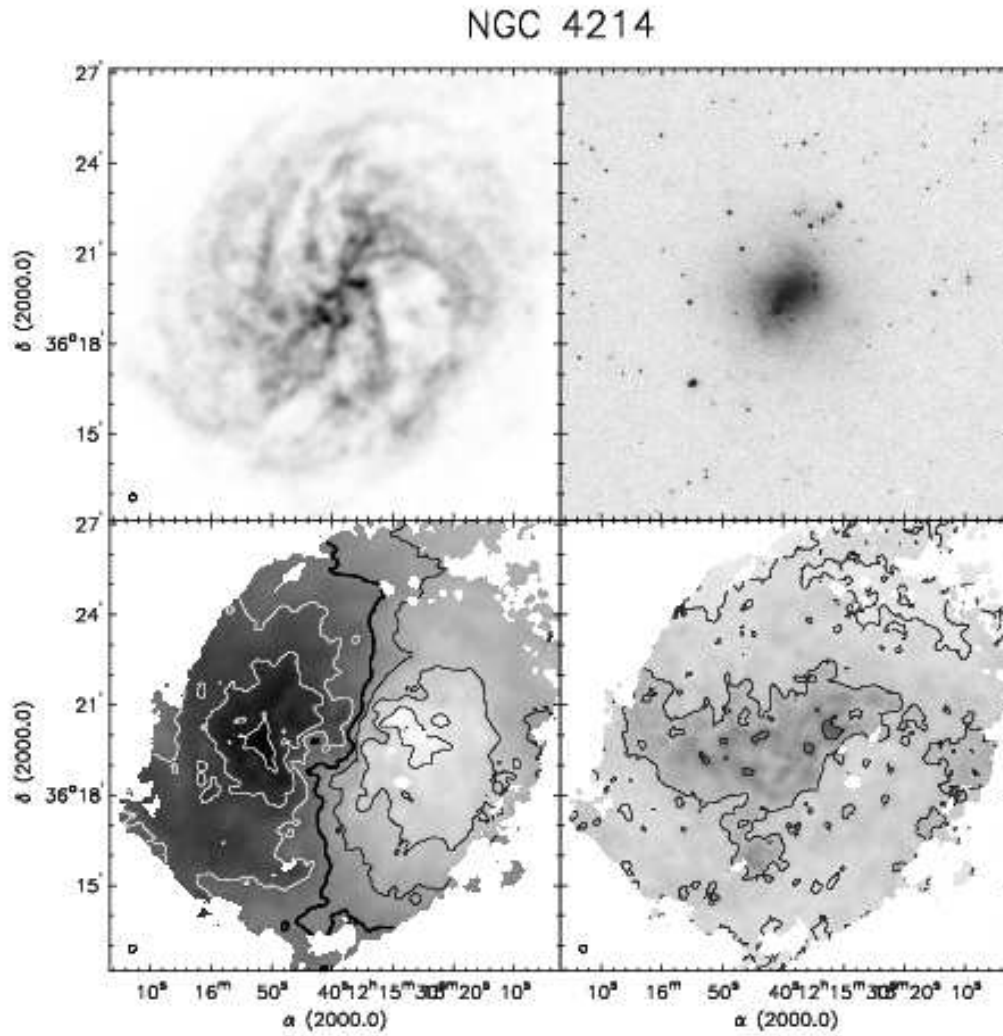


FIG. 47.— **NGC 4214**. *Top left:* integrated HI map (moment 0). Greyscale range from 0–610  $\text{Jy km s}^{-1}$ . *Top right:* Optical image from the digitized sky survey (DSS). *Bottom left:* Velocity field (moment 1). Black contours (lighter greyscale) indicate approaching emission, white contours (darker greyscale) receding emission. The thick black contour is the systemic velocity ( $v_{\text{sys}} = 292.8 \text{ km s}^{-1}$ ), the iso-velocity contours are spaced by  $\Delta v = 12.5 \text{ km s}^{-1}$ . *Bottom right:* Velocity dispersion map (moment 2). Contours are plotted at 5, 10 and 20  $\text{km s}^{-1}$ .

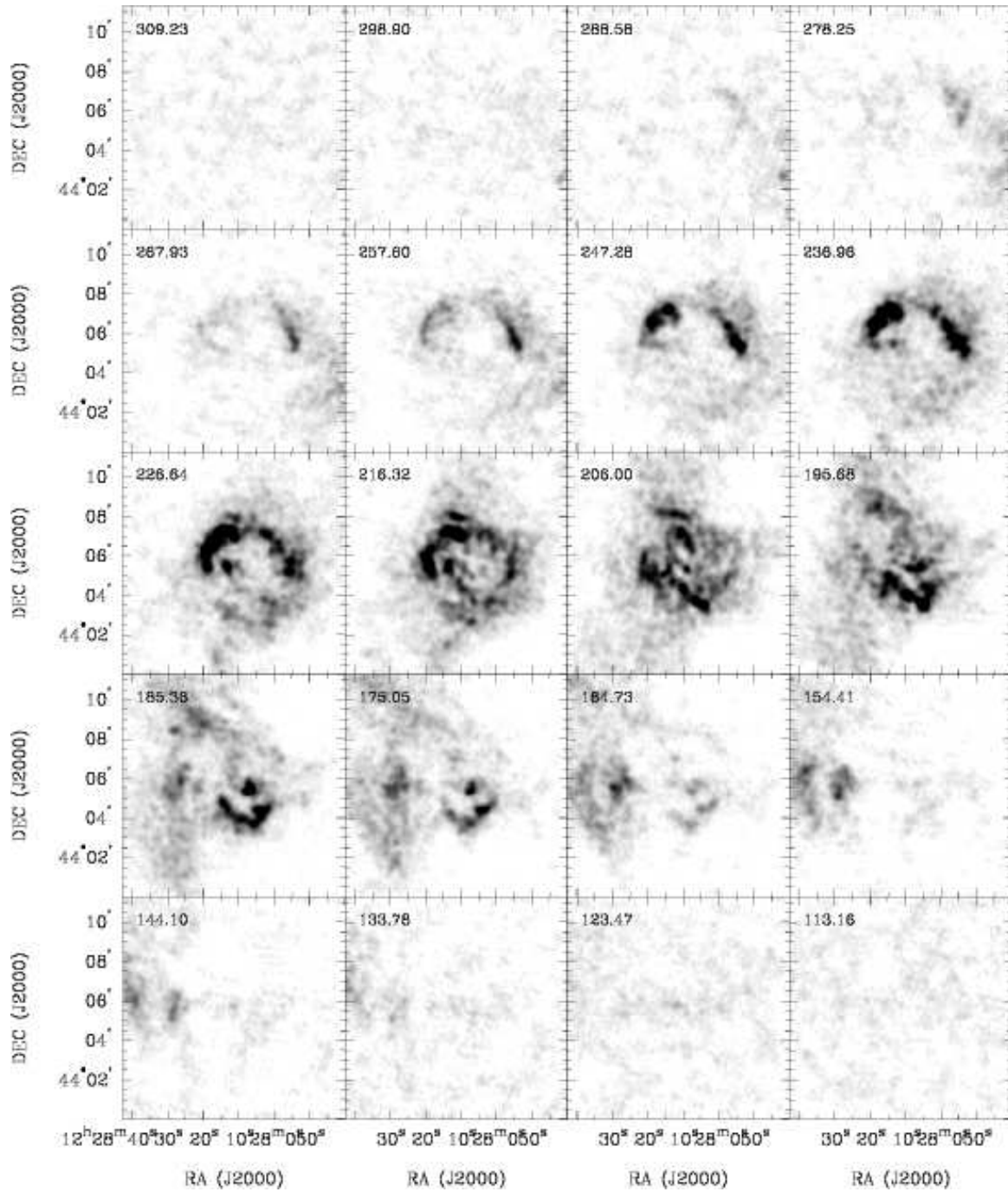


FIG. 48.— **NGC 4449**: Channel maps based on the NA cube (greyscale range:  $-0.02$  to  $20 \text{ mJy beam}^{-1}$ ). Every second channel is shown (channel width:  $5.2 \text{ km s}^{-1}$ ). The area shown in each panel is identical to the area shown on the next figure

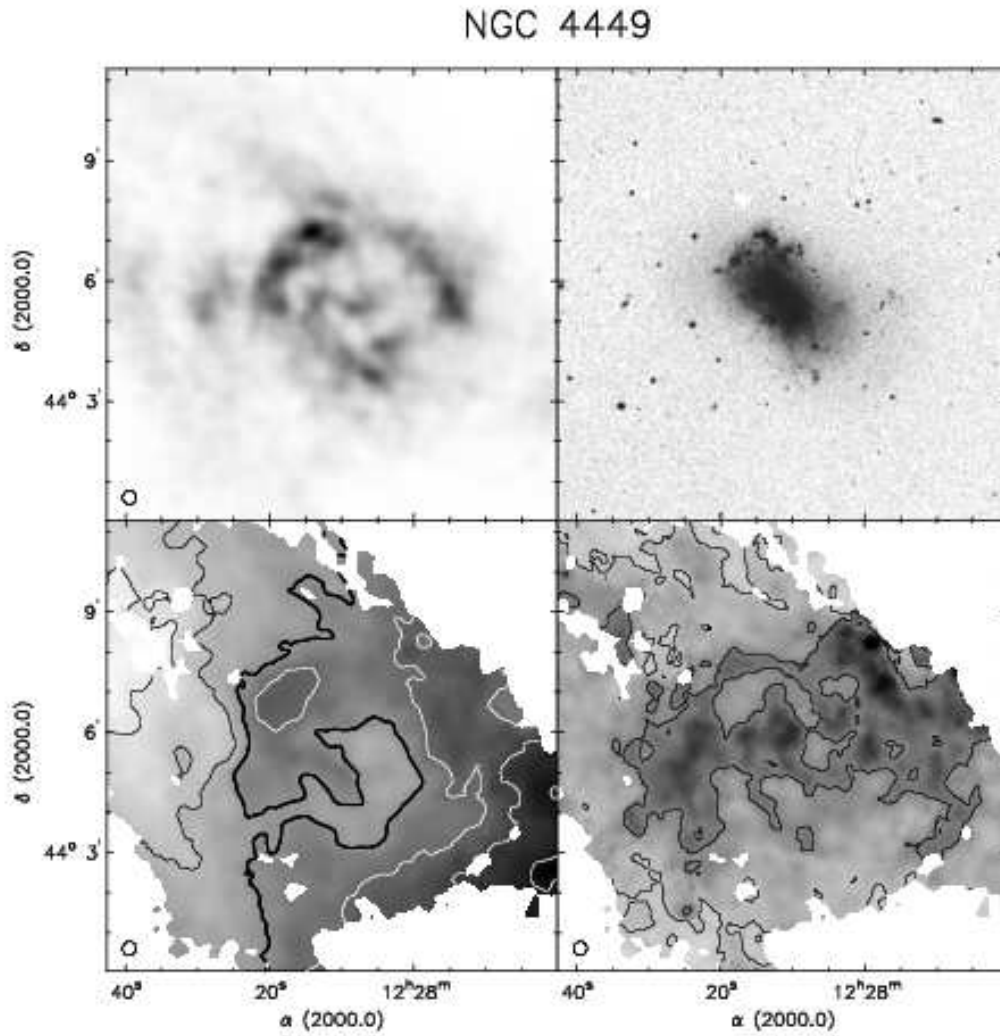


FIG. 49.— NGC 4449. *Top left*: integrated HI map (moment 0). Greyscale range from 0–1830 Jy km s<sup>-1</sup>. *Top right*: Optical image from the digitized sky survey (DSS). *Bottom left*: Velocity field (moment 1). Black contours (lighter greyscale) indicate approaching emission, white contours (darker greyscale) receding emission. The thick black contour is the systemic velocity ( $v_{\text{sys}}=202.7$  km s<sup>-1</sup>), the iso-velocity contours are spaced by  $\Delta v=25.0$  km s<sup>-1</sup>. *Bottom right*: Velocity dispersion map (moment 2). Contours are plotted at 5, 10 and 20 km s<sup>-1</sup>.

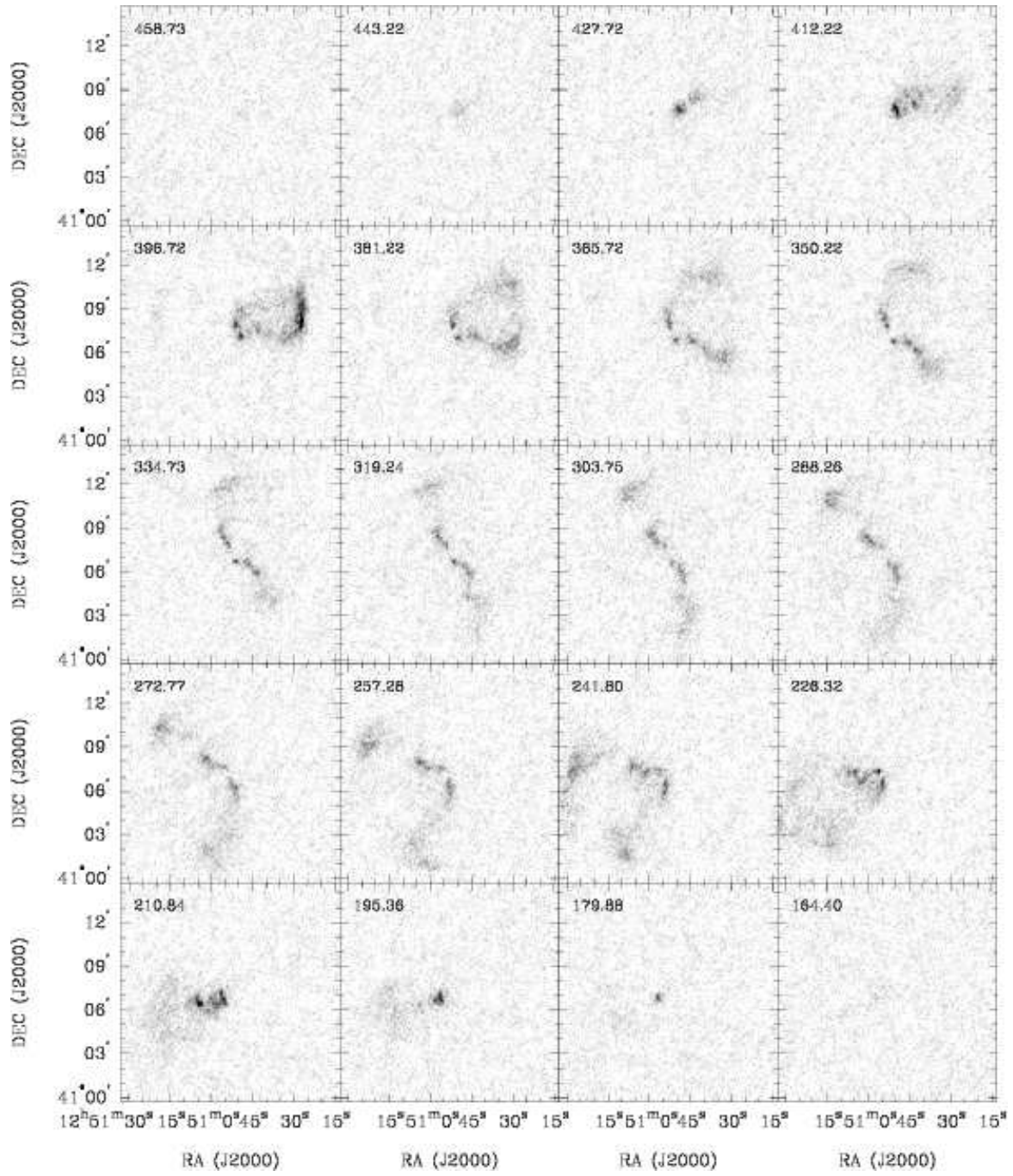


FIG. 50.— **NGC 4736**: Channel maps based on the NA cube (greyscale range:  $-0.02$  to  $6 \text{ mJy beam}^{-1}$ ). Every third channel is shown (channel width:  $5.2 \text{ km s}^{-1}$ ). The area shown in each panel is identical to the area shown on the next figure

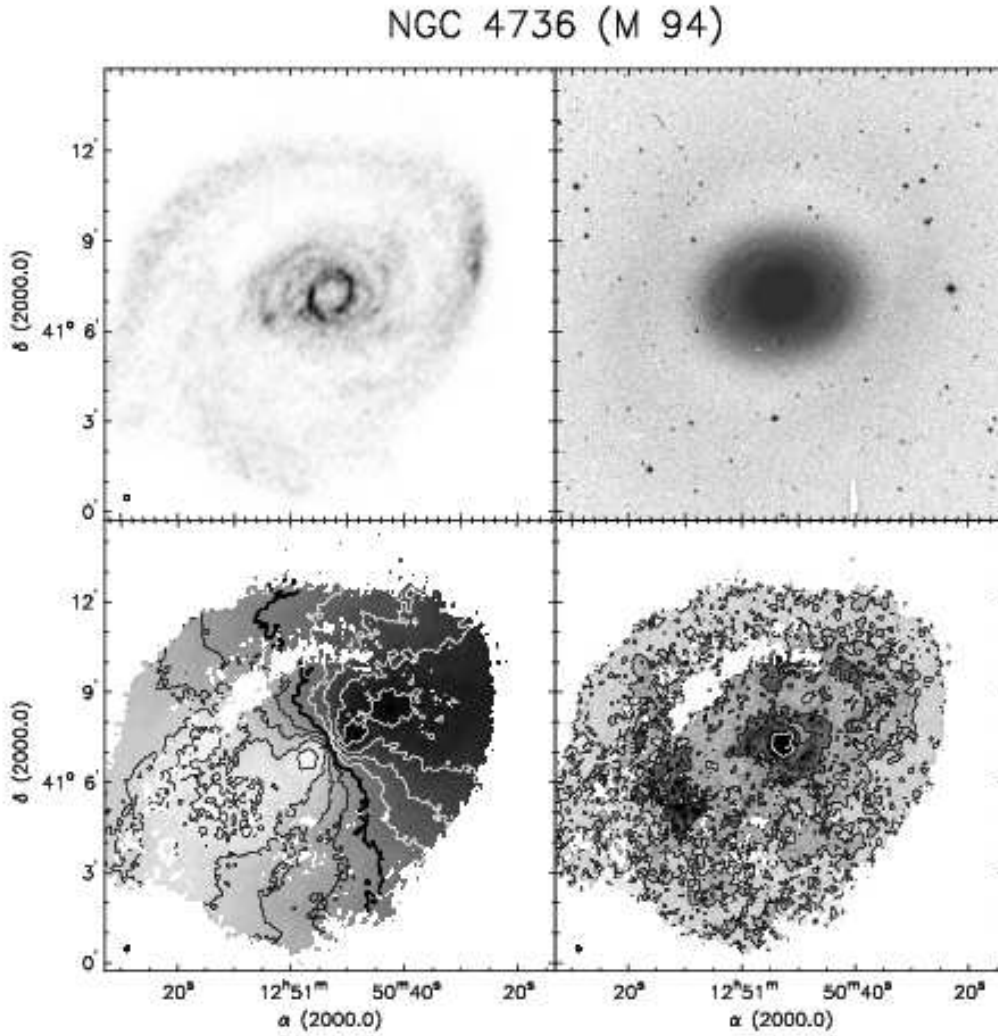


FIG. 51.— **NGC 4736**. *Top left*: integrated HI map (moment 0). Greyscale range from 0–209  $\text{Jy km s}^{-1}$ . *Top right*: Optical image from the digitized sky survey (DSS). *Bottom left*: Velocity field (moment 1). Black contours (lighter greyscale) indicate approaching emission, white contours (darker greyscale) receding emission. The thick black contour is the systemic velocity ( $v_{\text{sys}}=307.6 \text{ km s}^{-1}$ ), the iso-velocity contours are spaced by  $\Delta v=25.0 \text{ km s}^{-1}$ . *Bottom right*: Velocity dispersion map (moment 2). Contours are plotted at 5, 10 and 20  $\text{km s}^{-1}$  (white contour: 50  $\text{km s}^{-1}$ ).

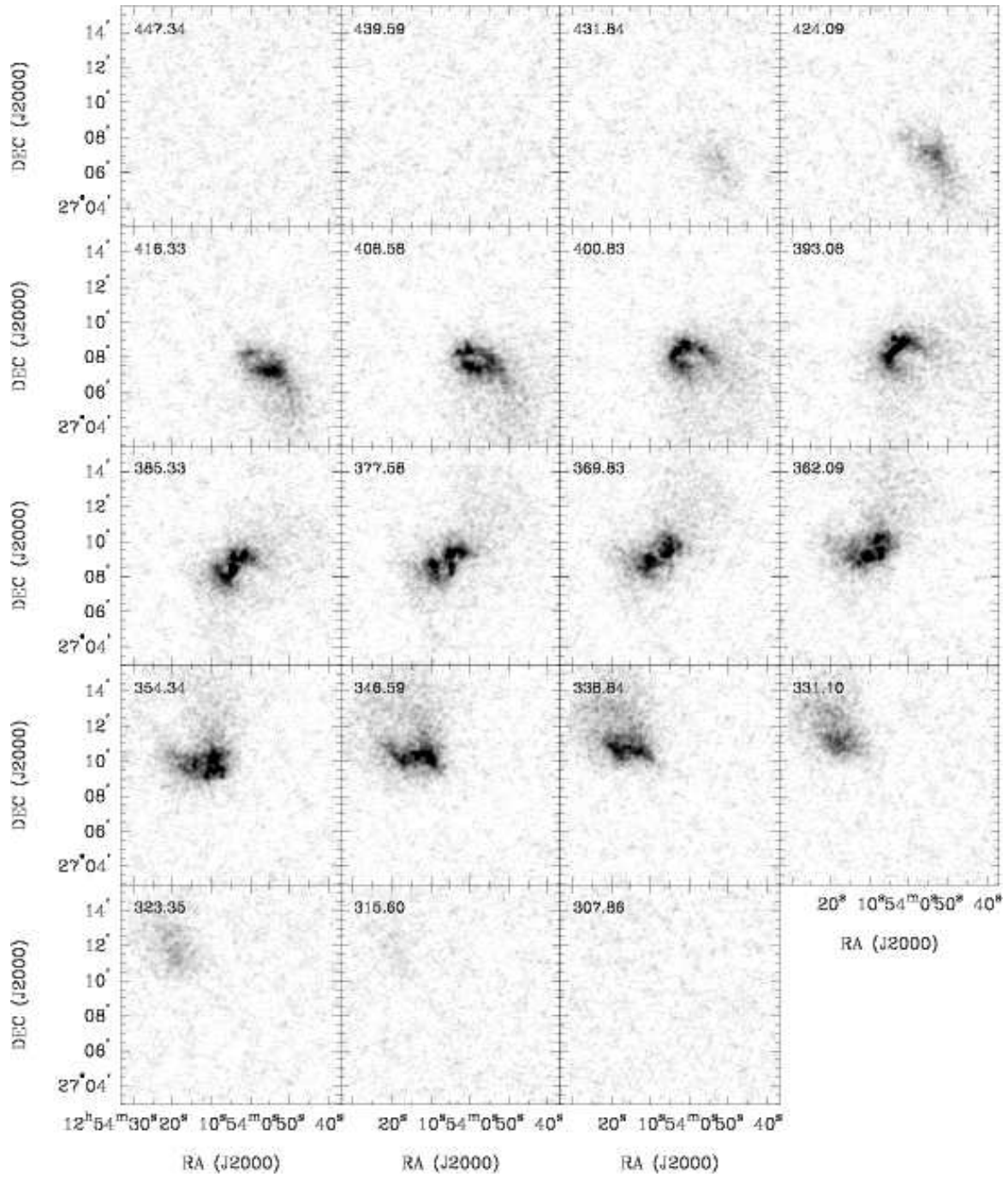


FIG. 52.— **DDO 154**: Channel maps based on the NA cube (greyscale range:  $-0.02$  to  $10 \text{ mJy beam}^{-1}$ ). Every third channel is shown (channel width:  $2.6 \text{ km s}^{-1}$ ). The area shown in each panel is identical to the area shown on the next figure



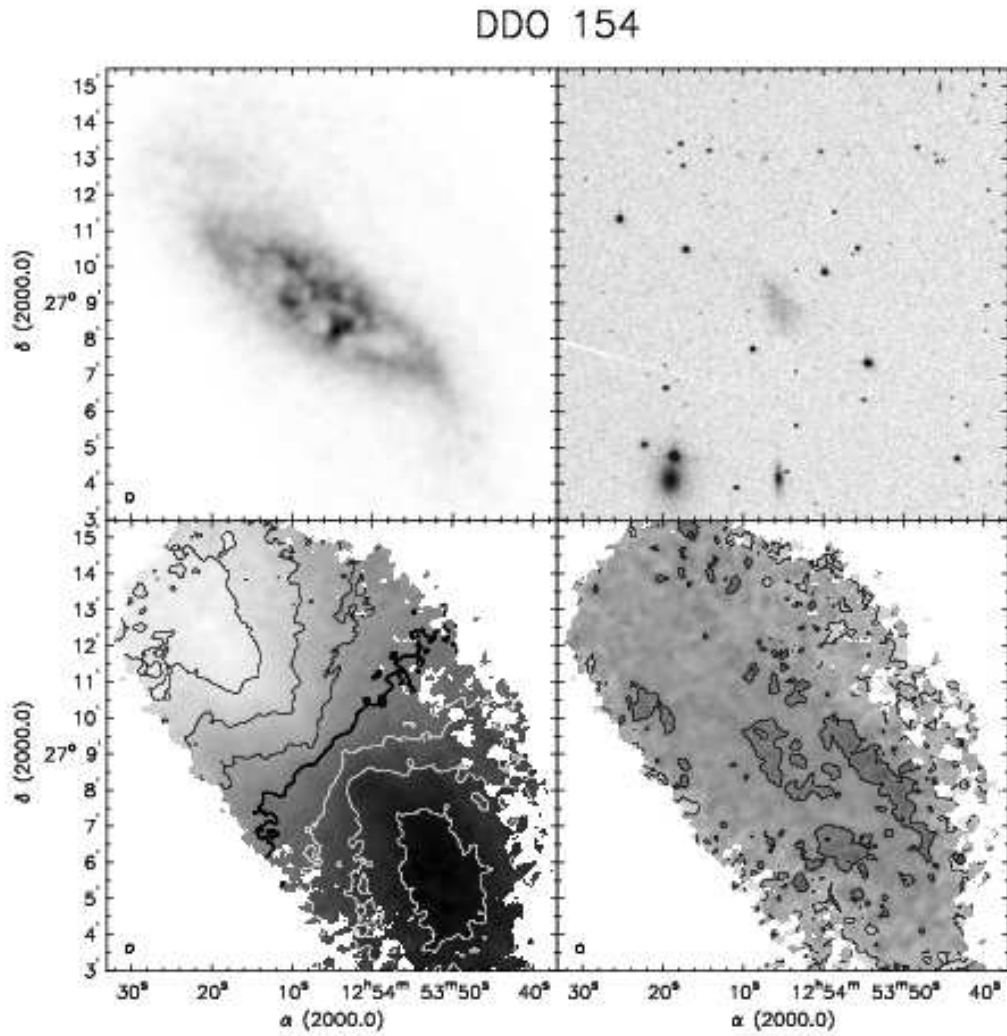


FIG. 53.— **DDO 154**. *Top left:* integrated HI map (moment 0). Greyscale range from 0–454  $\text{Jy km s}^{-1}$ . *Top right:* Optical image from the digitized sky survey (DSS). *Bottom left:* Velocity field (moment 1). Black contours (lighter greyscale) indicate approaching emission, white contours (darker greyscale) receding emission. The thick black contour is the systemic velocity ( $v_{\text{sys}} = 375.5 \text{ km s}^{-1}$ ), the iso-velocity contours are spaced by  $\Delta v = 12.50 \text{ km s}^{-1}$ . *Bottom right:* Velocity dispersion map (moment 2). Contours are plotted at 5, 10  $\text{km s}^{-1}$ .

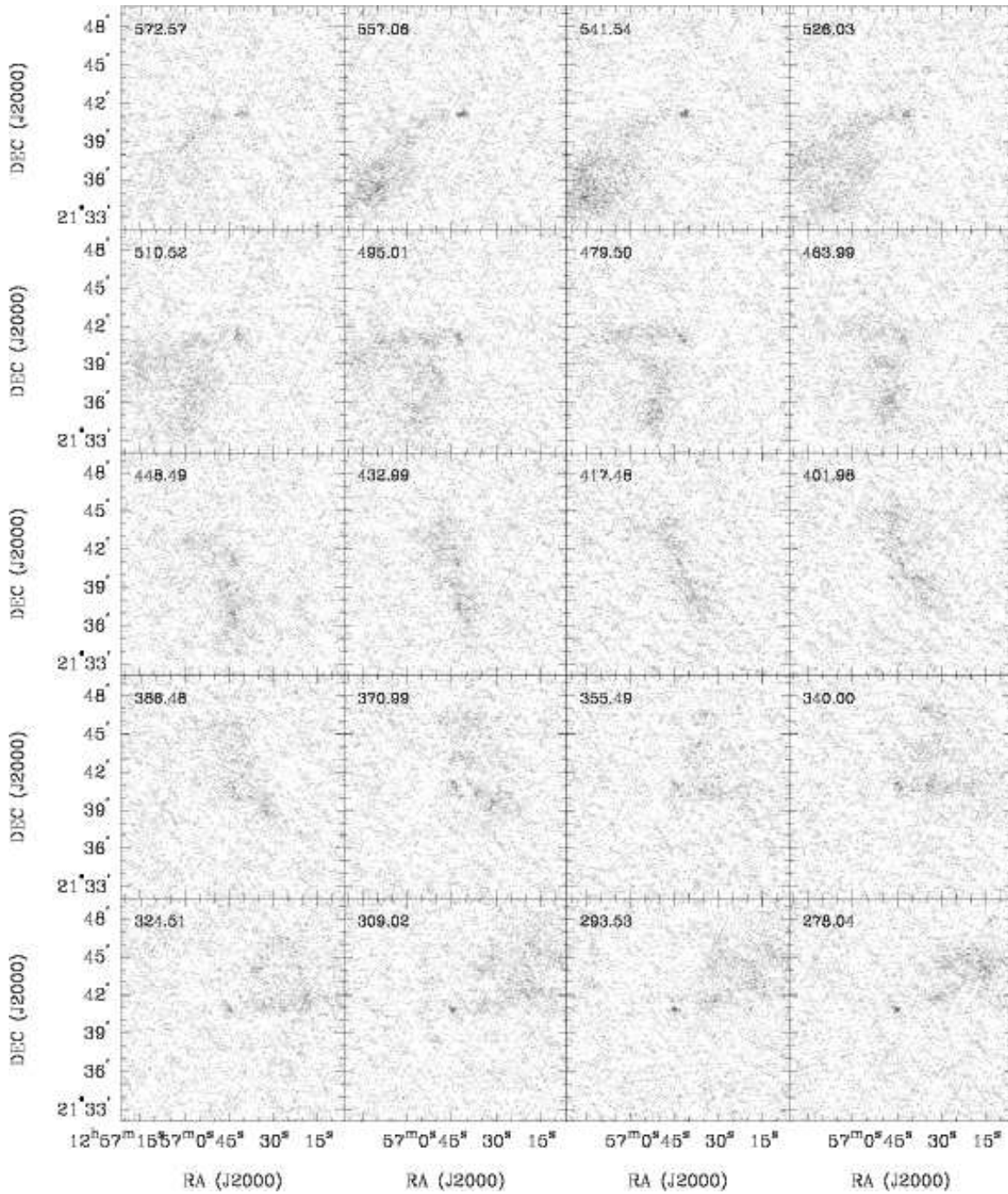


FIG. 54.— **NGC 4826**: Channel maps based on the NA cube (greyscale range:  $-0.02$  to  $5 \text{ mJy beam}^{-1}$ ). Every third channel is shown (channel width:  $5.2 \text{ km s}^{-1}$ ). The area shown in each panel is identical to the area shown on the next figure

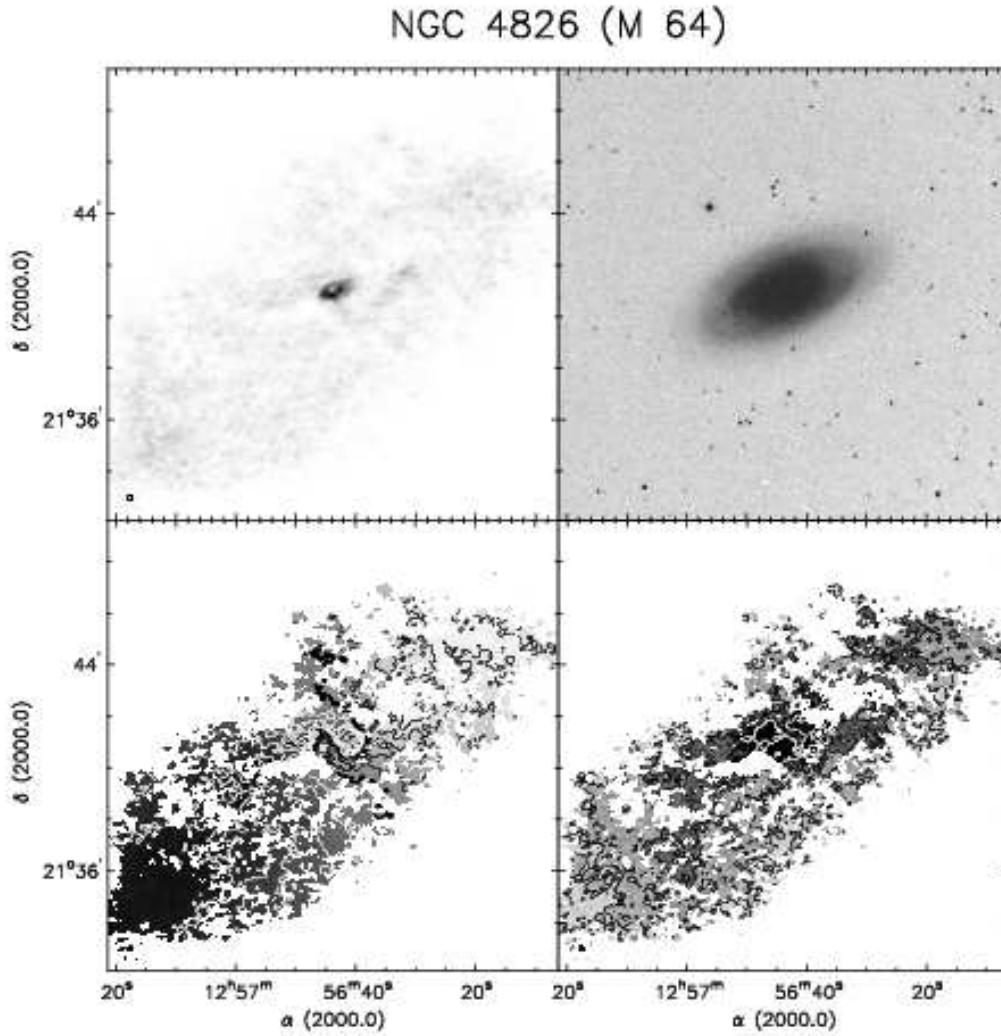


FIG. 55.— **NGC 4826**. *Top left*: integrated HI map (moment 0). Greyscale range from 0–205  $\text{Jy km s}^{-1}$ . *Top right*: Optical image from the digitized sky survey (DSS). *Bottom left*: Velocity field (moment 1). Black contours (lighter greyscale) indicate approaching emission, white contours (darker greyscale) receding emission. The thick black contour is the systemic velocity ( $v_{\text{sys}}=407.90 \text{ km s}^{-1}$ ), the iso-velocity contours are spaced by  $\Delta v=25.0 \text{ km s}^{-1}$ . *Bottom right*: Velocity dispersion map (moment 2). Contours are plotted at 5, 10 and  $20 \text{ km s}^{-1}$  (white contour:  $50 \text{ km s}^{-1}$ ).

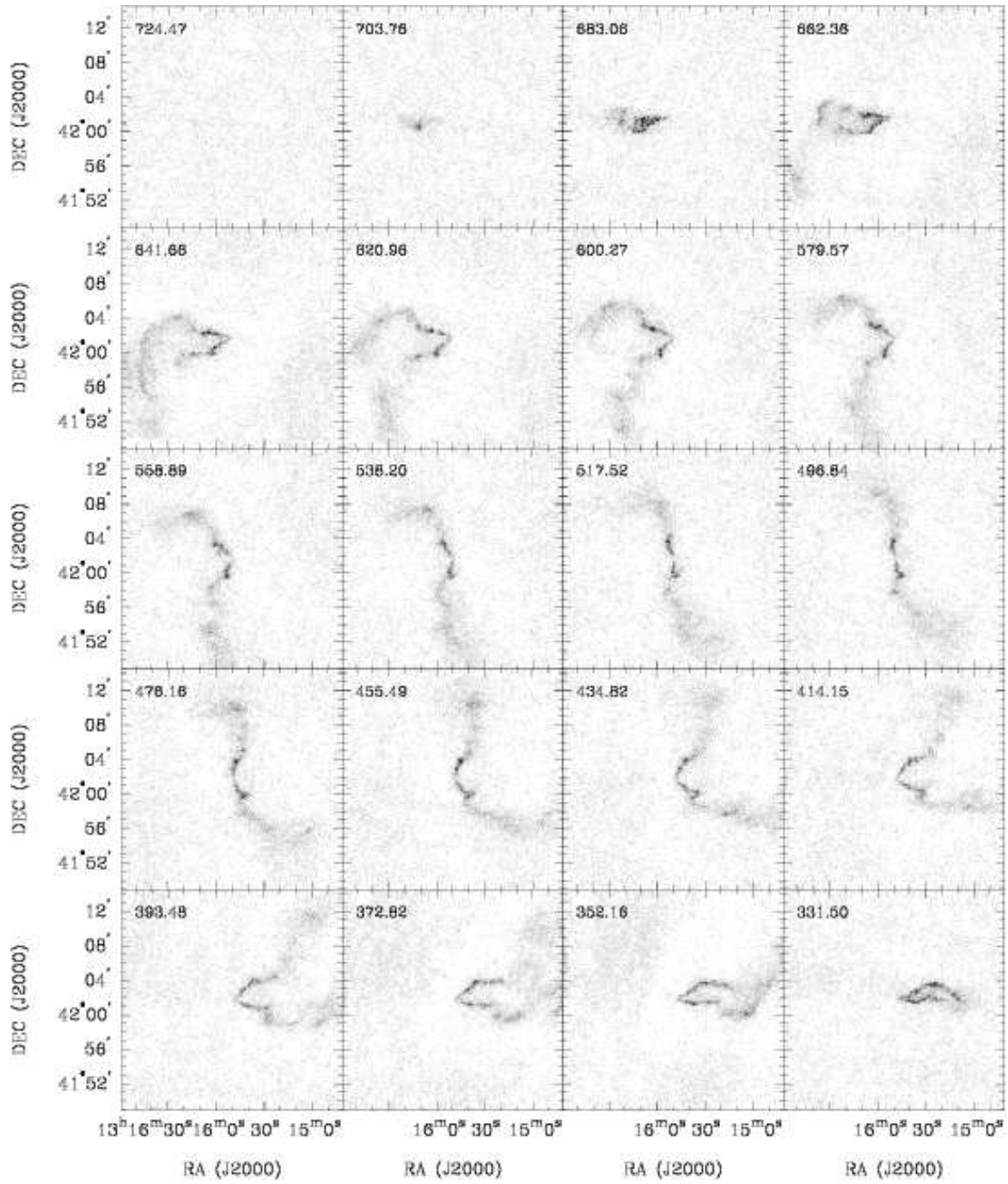


FIG. 56.— **NGC 5055**: Channel maps based on the NA cube (greyscale range:  $-0.02$  to  $8 \text{ mJy beam}^{-1}$ ). Every fourth channel is shown (channel width:  $5.2 \text{ km s}^{-1}$ ). The area shown in each panel is identical to the area shown on the next figure

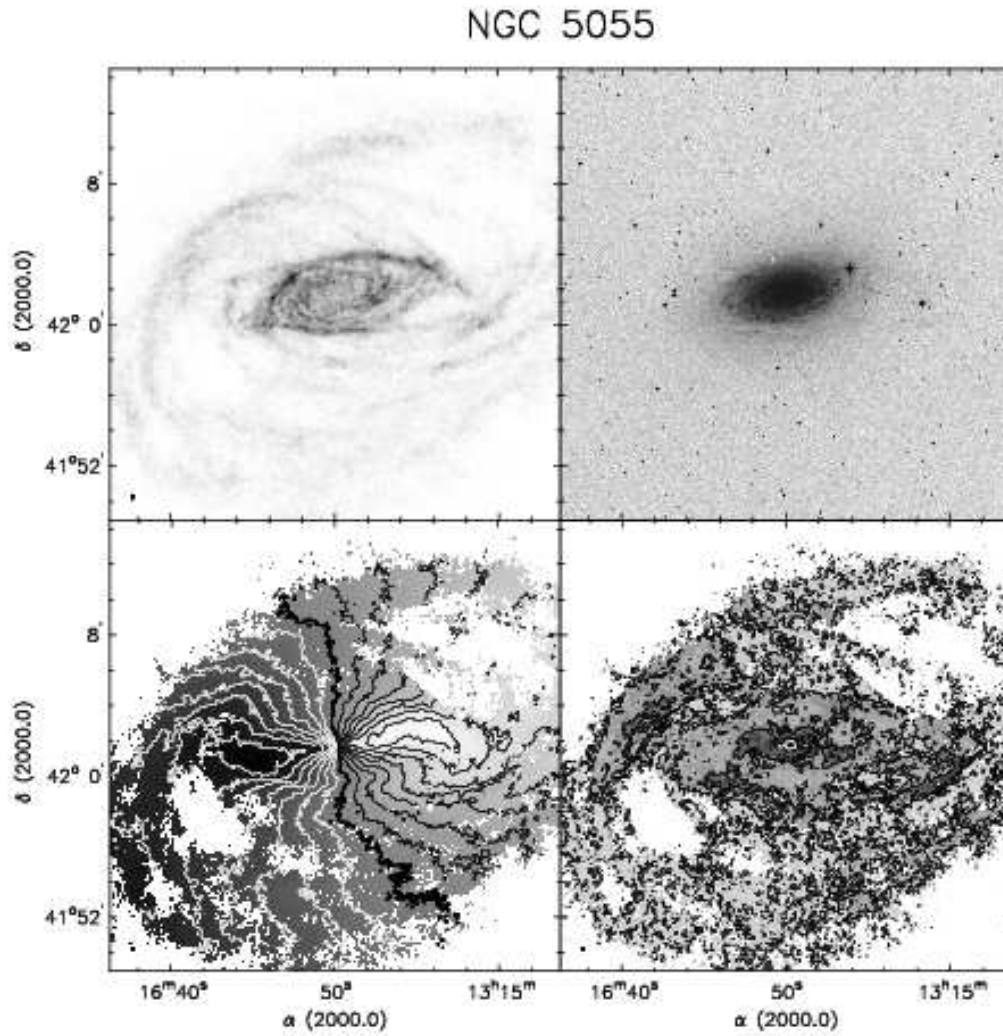


FIG. 57.— **NGC 5055**. *Top left*: integrated HI map (moment 0). Greyscale range from 0–285  $\text{Jy km s}^{-1}$ . *Top right*: Optical image from the digitized sky survey (DSS). *Bottom left*: Velocity field (moment 1). Black contours (lighter greyscale) indicate approaching emission, white contours (darker greyscale) receding emission. The thick black contour is the systemic velocity ( $v_{\text{sys}}=499.3 \text{ km s}^{-1}$ ), the iso-velocity contours are spaced by  $\Delta v=25 \text{ km s}^{-1}$ . *Bottom right*: Velocity dispersion map (moment 2). Contours are plotted at 5, 10 and  $20 \text{ km s}^{-1}$  (white contour:  $50 \text{ km s}^{-1}$ ).

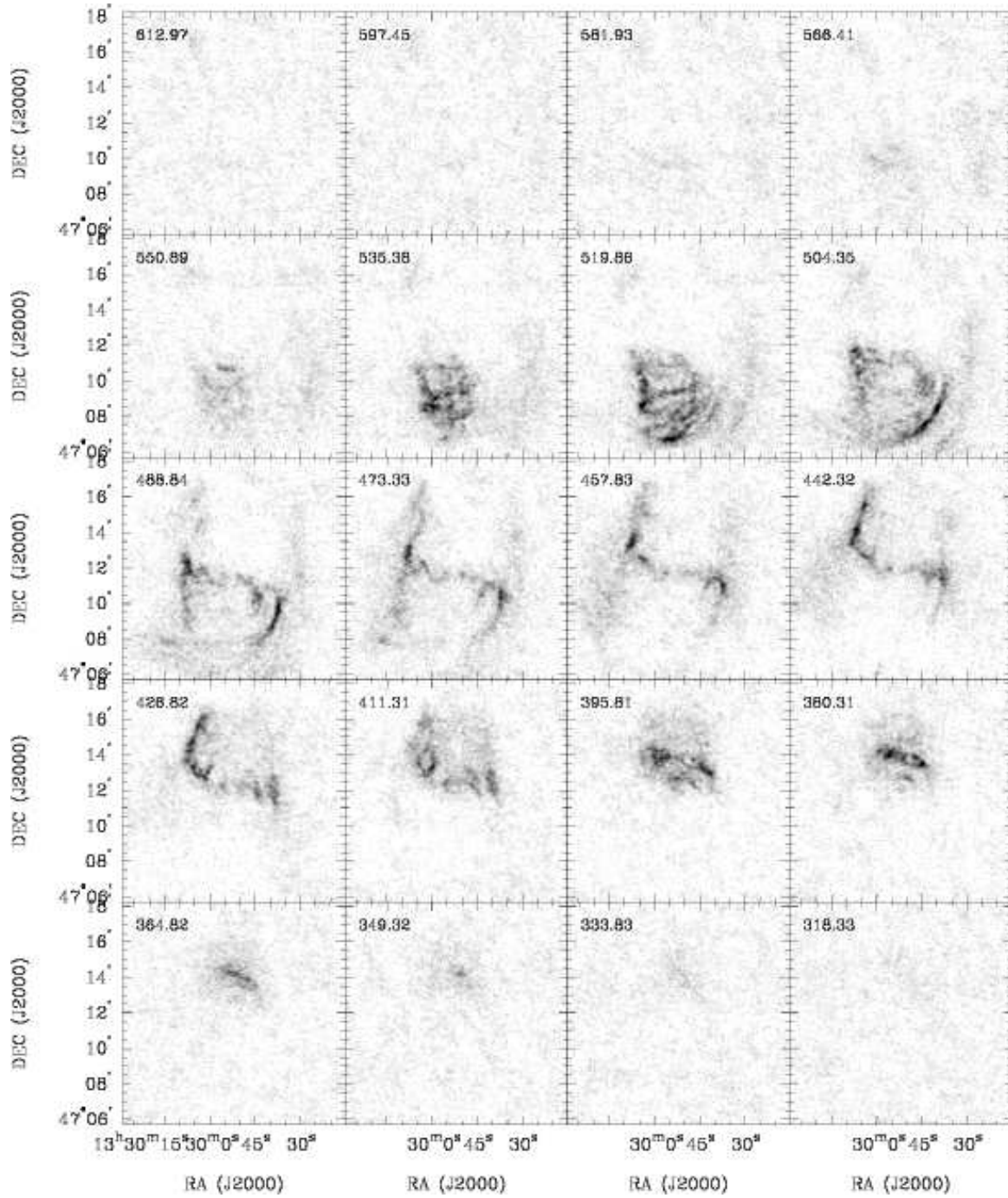


FIG. 58.— **NGC 5194**: Channel maps based on the NA cube (greyscale range:  $-0.02$  to  $8 \text{ mJy beam}^{-1}$ ). Every third channel is shown (channel width:  $5.2 \text{ km s}^{-1}$ ). The area shown in each panel is identical to the area shown on the next figure

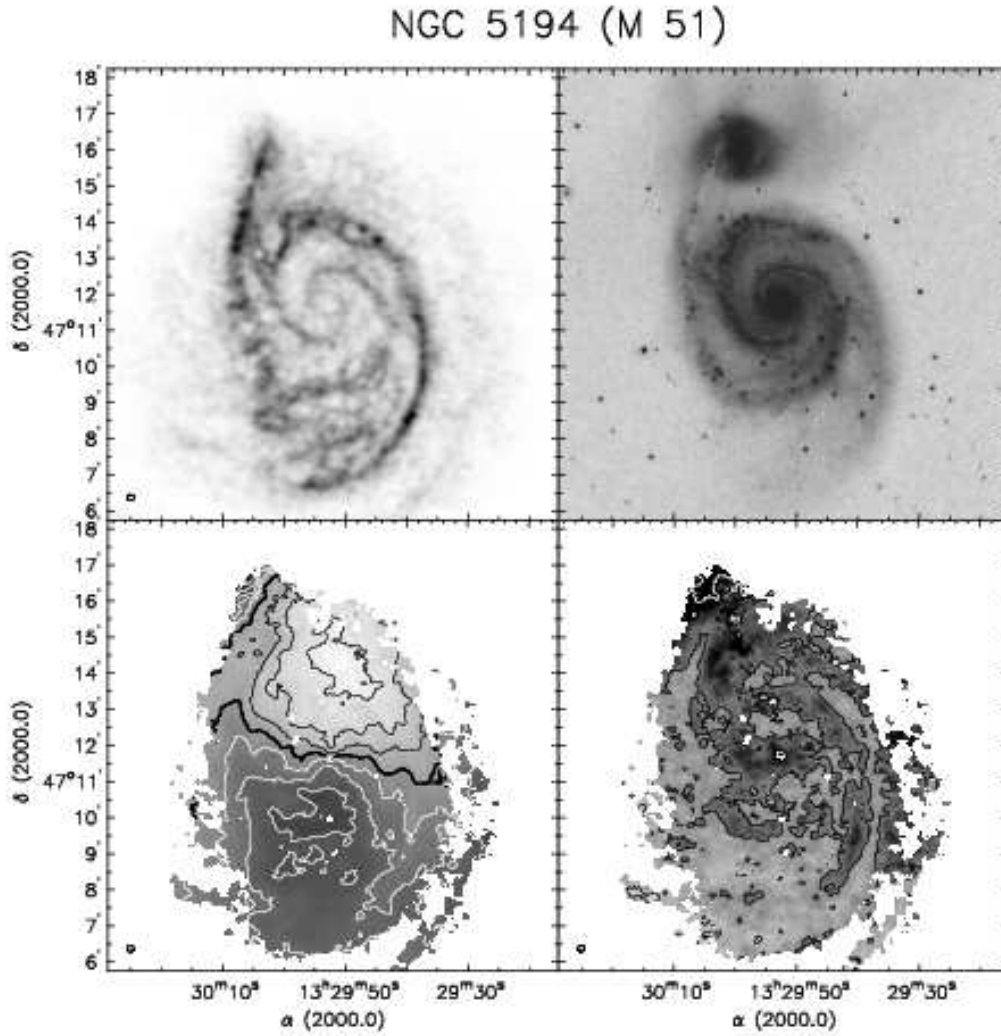


FIG. 59.— **NGC 5194**. *Top left*: integrated HI map (moment 0). Greyscale range from 0–312 Jy km s<sup>-1</sup>. *Top right*: Optical image from the digitized sky survey (DSS). *Bottom left*: Velocity field (moment 1). Black contours (lighter greyscale) indicate approaching emission, white contours (darker greyscale) receding emission. The thick black contour is the systemic velocity ( $v_{\text{sys}}=456.2$  km s<sup>-1</sup>), the iso-velocity contours are spaced by  $\Delta v=25$  km s<sup>-1</sup>. *Bottom right*: Velocity dispersion map (moment 2). Contours are plotted at 5, 10 and 20 km s<sup>-1</sup> (white contour: 50 km s<sup>-1</sup>).

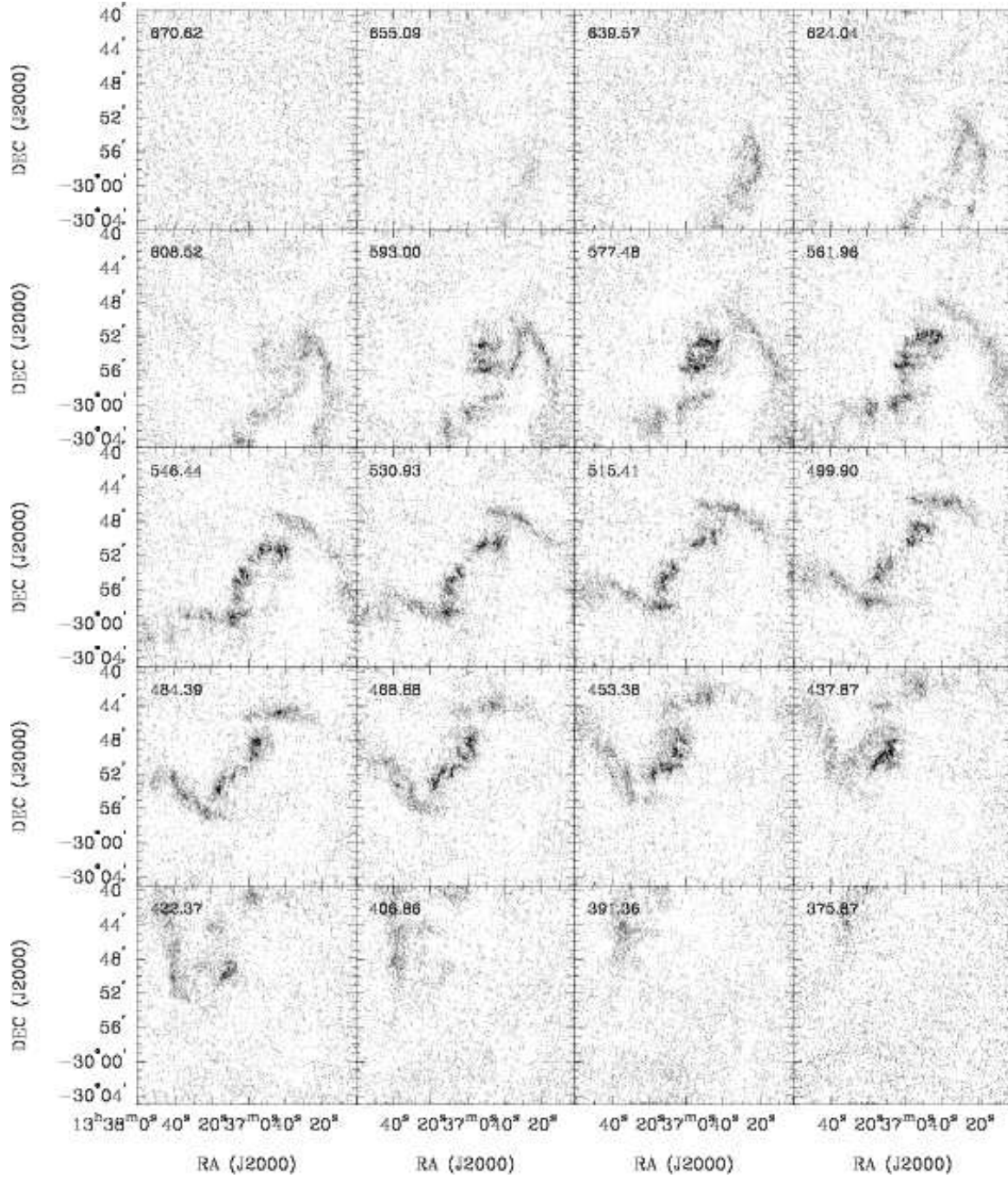


FIG. 60.— **NGC 5236**: Channel maps based on the NA cube (greyscale range:  $-0.02$  to  $8 \text{ mJy beam}^{-1}$ ). Every sixth channel is shown (channel width:  $2.6 \text{ km s}^{-1}$ ). The area shown in each panel is identical to the area shown on the next figure



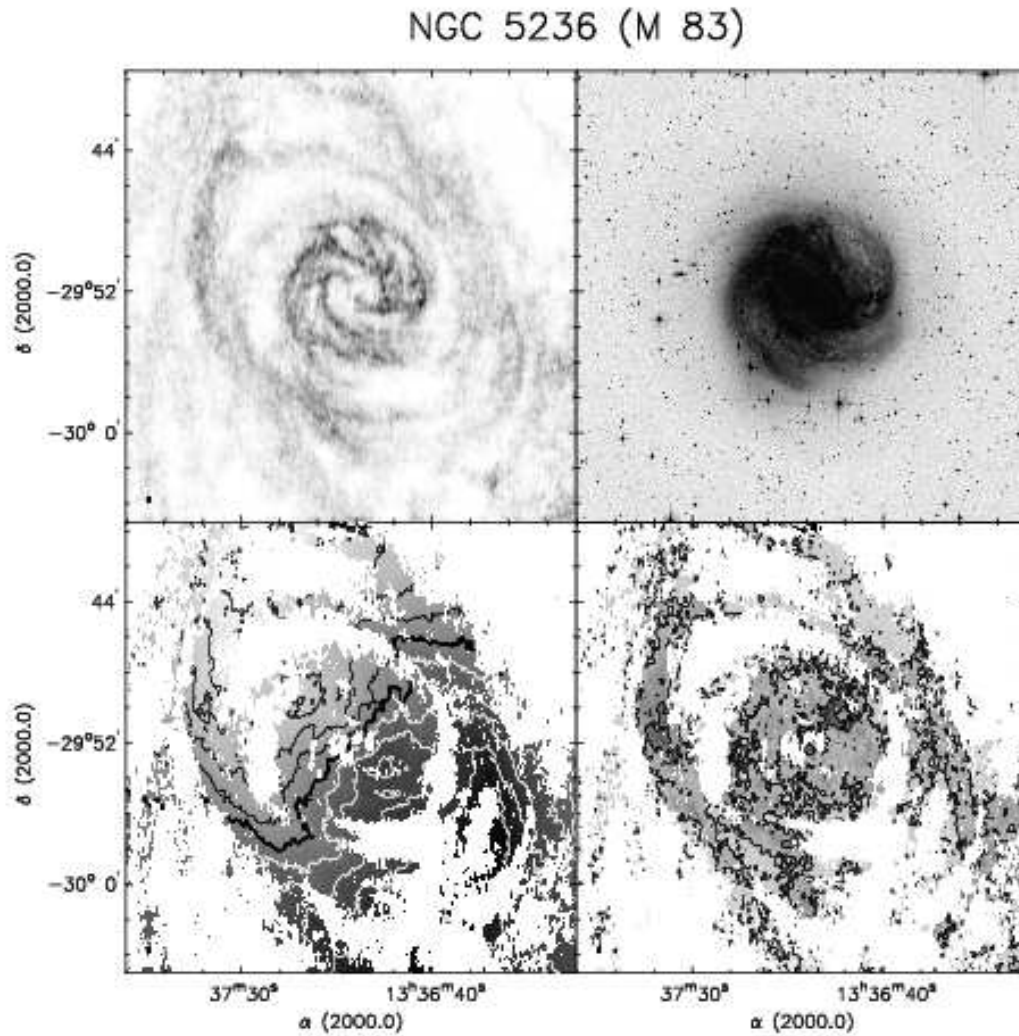


FIG. 61.— **NGC 5236**. *Top left*: integrated HI map (moment 0). Greyscale range from 0–301 Jy km s<sup>-1</sup>. *Top right*: Optical image from the digitized sky survey (DSS). *Bottom left*: Velocity field (moment 1). Black contours (lighter greyscale) indicate approaching emission, white contours (darker greyscale) receding emission. The thick black contour is the systemic velocity ( $v_{\text{sys}}=510.0$  km s<sup>-1</sup>), the iso-velocity contours are spaced by  $\Delta v=25$  km s<sup>-1</sup>. *Bottom right*: Velocity dispersion map (moment 2). Contours are plotted at 5, 10 and 20 km s<sup>-1</sup>.

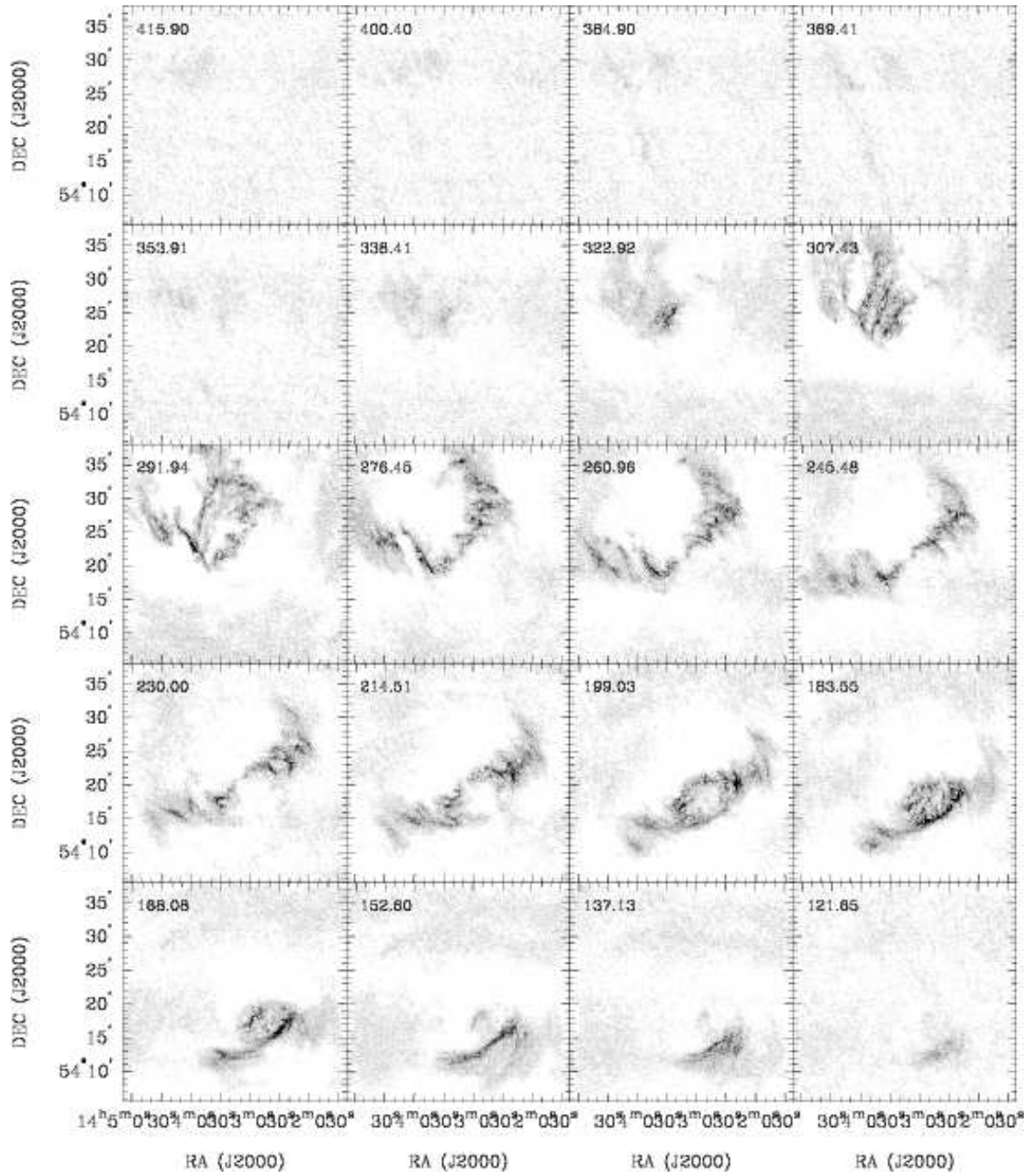


FIG. 62.— **NGC 5457**: Channel maps based on the NA cube (greyscale range:  $-0.02$  to  $10 \text{ mJy beam}^{-1}$ ). Every third channel is shown (channel width:  $5.2 \text{ km s}^{-1}$ ). The area shown in each panel is identical to the area shown on the next figure

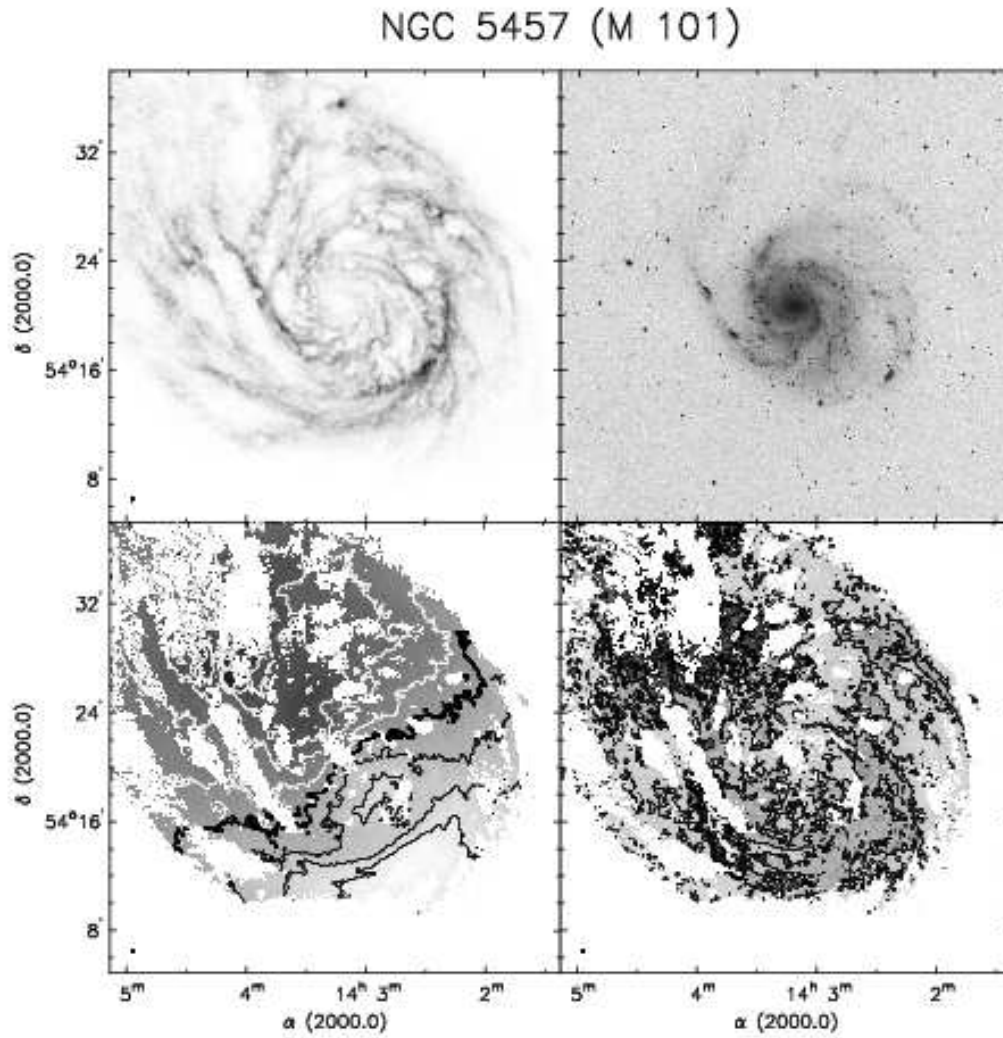


FIG. 63.— **NGC 5457**. *Top left*: integrated HI map (moment 0). Greyscale range from 0–510  $\text{Jy km s}^{-1}$ . *Top right*: Optical image from the digitized sky survey (DSS). *Bottom left*: Velocity field (moment 1). Black contours (lighter greyscale) indicate approaching emission, white contours (darker greyscale) receding emission. The thick black contour is the systemic velocity ( $v_{\text{sys}}=226.4 \text{ km s}^{-1}$ ), the iso-velocity contours are spaced by  $\Delta v=25 \text{ km s}^{-1}$ . *Bottom right*: Velocity dispersion map (moment 2). Contours are plotted at 5, 10 and 20  $\text{km s}^{-1}$ .

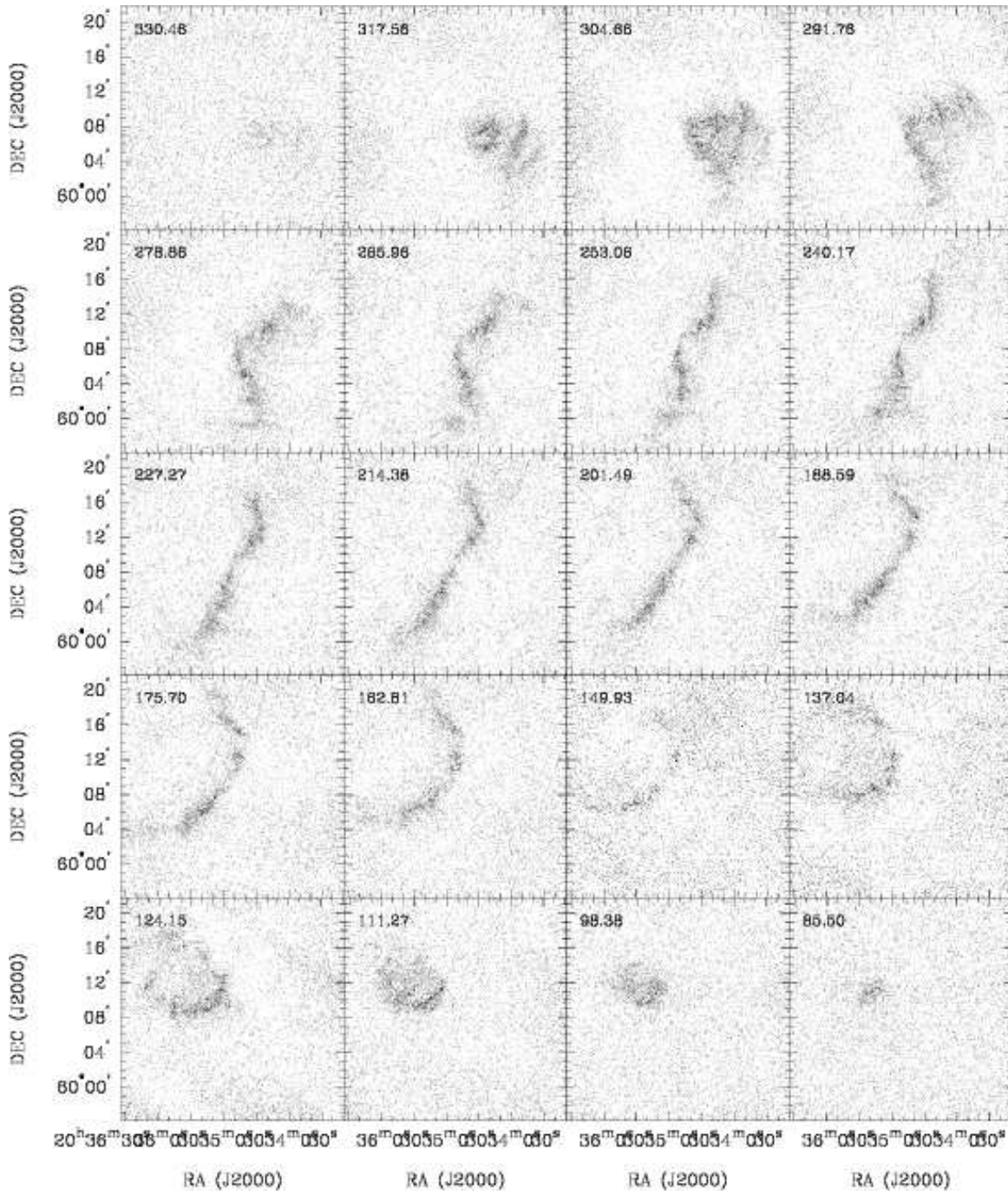


FIG. 64.— **NGC 6946**: Channel maps based on the NA cube (greyscale range:  $-0.02$  to  $6 \text{ mJy beam}^{-1}$ ). Every fifth channel is shown (channel width:  $2.6 \text{ km s}^{-1}$ ). The area shown in each panel is identical to the area shown on the next figure

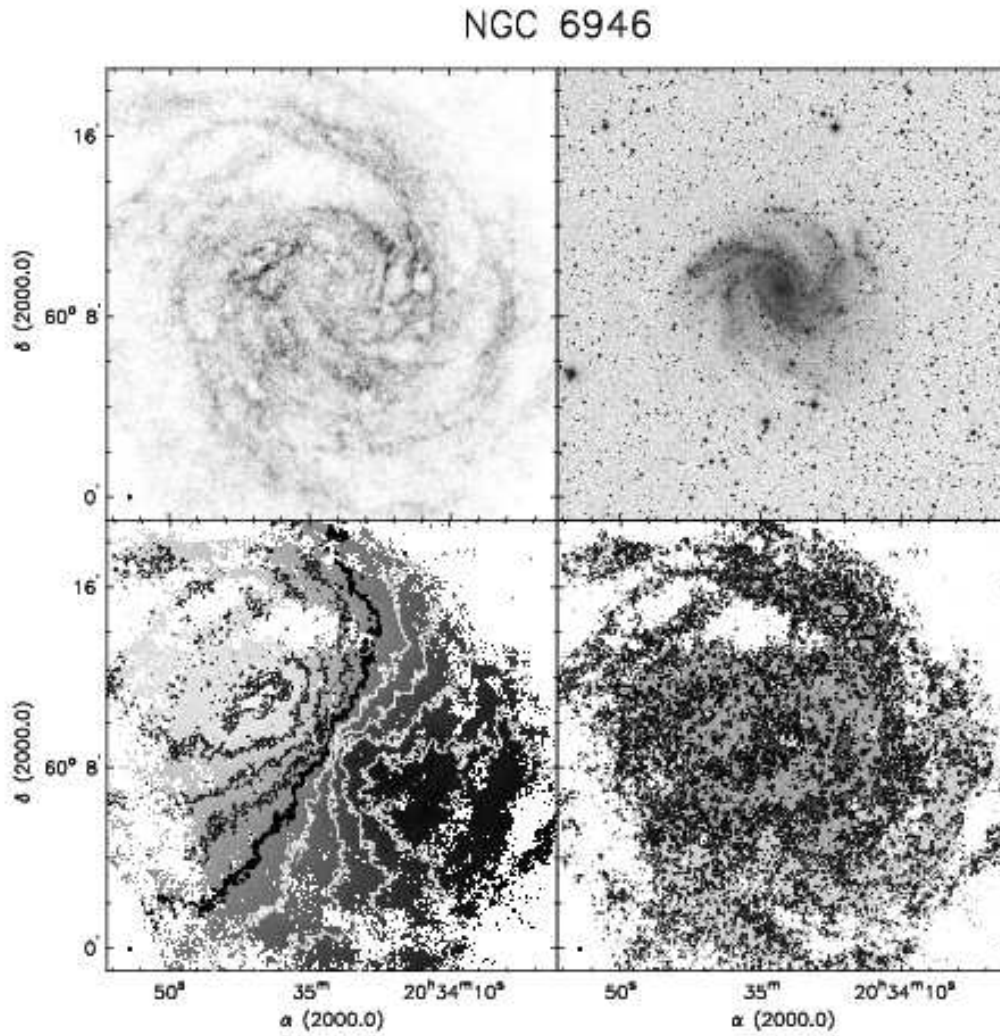


FIG. 65.— **NGC 6946**. *Top left*: integrated HI map (moment 0). Greyscale range from 0–121  $\text{Jy km s}^{-1}$ . *Top right*: Optical image from the digitized sky survey (DSS). *Bottom left*: Velocity field (moment 1). Black contours (lighter greyscale) indicate approaching emission, white contours (darker greyscale) receding emission. The thick black contour is the systemic velocity ( $v_{\text{sys}} = 200.0 \text{ km s}^{-1}$ ), the iso-velocity contours are spaced by  $\Delta v = 25 \text{ km s}^{-1}$ . *Bottom right*: Velocity dispersion map (moment 2). Contours are plotted at 5, 10 and 20  $\text{km s}^{-1}$ .

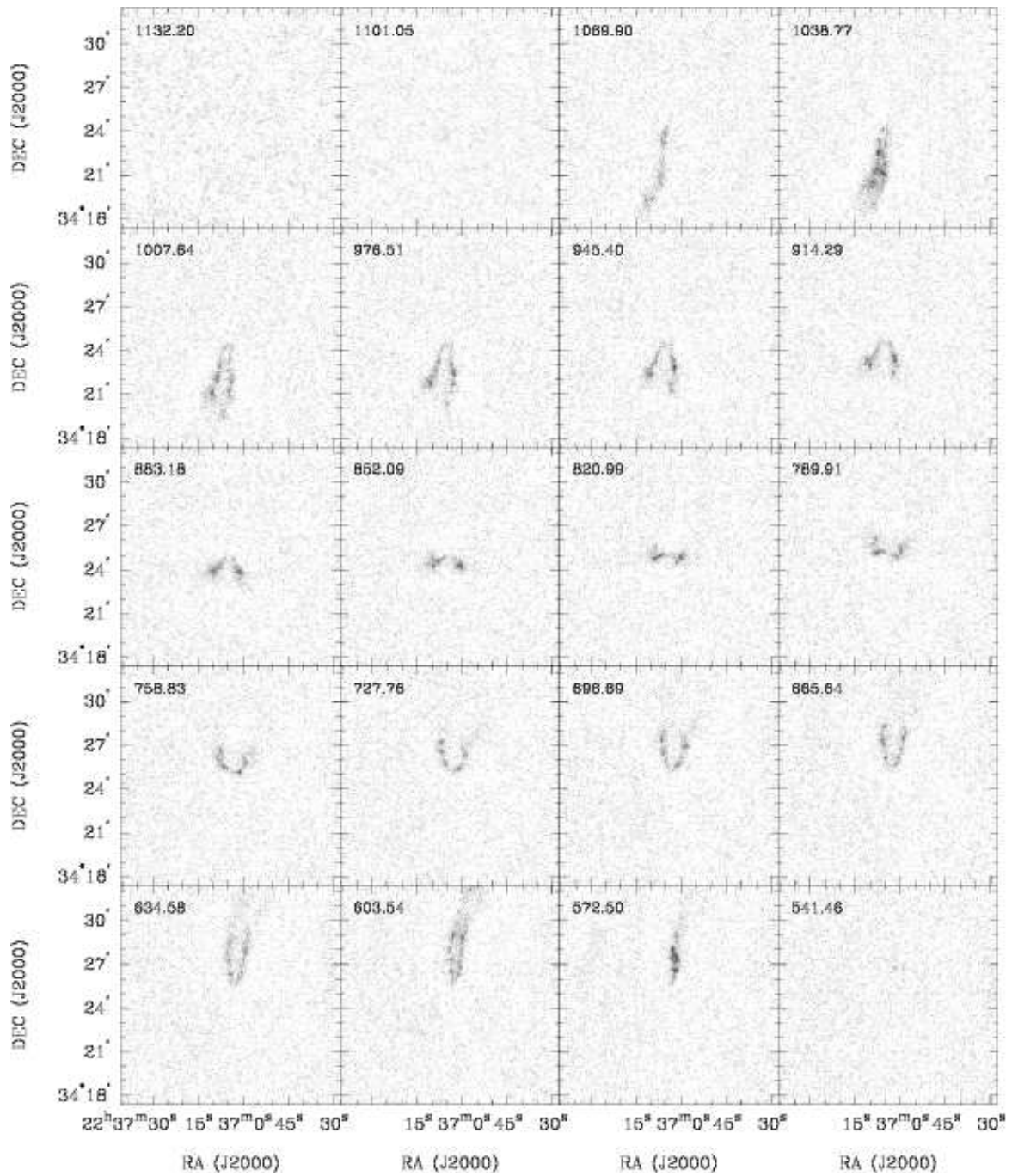


FIG. 66.— **NGC 7331**: Channel maps based on the NA cube (greyscale range:  $-0.02$  to  $8 \text{ mJy beam}^{-1}$ ). Every sixth channel is shown (channel width:  $5.2 \text{ km s}^{-1}$ ). The area shown in each panel is identical to the area shown on the next figure

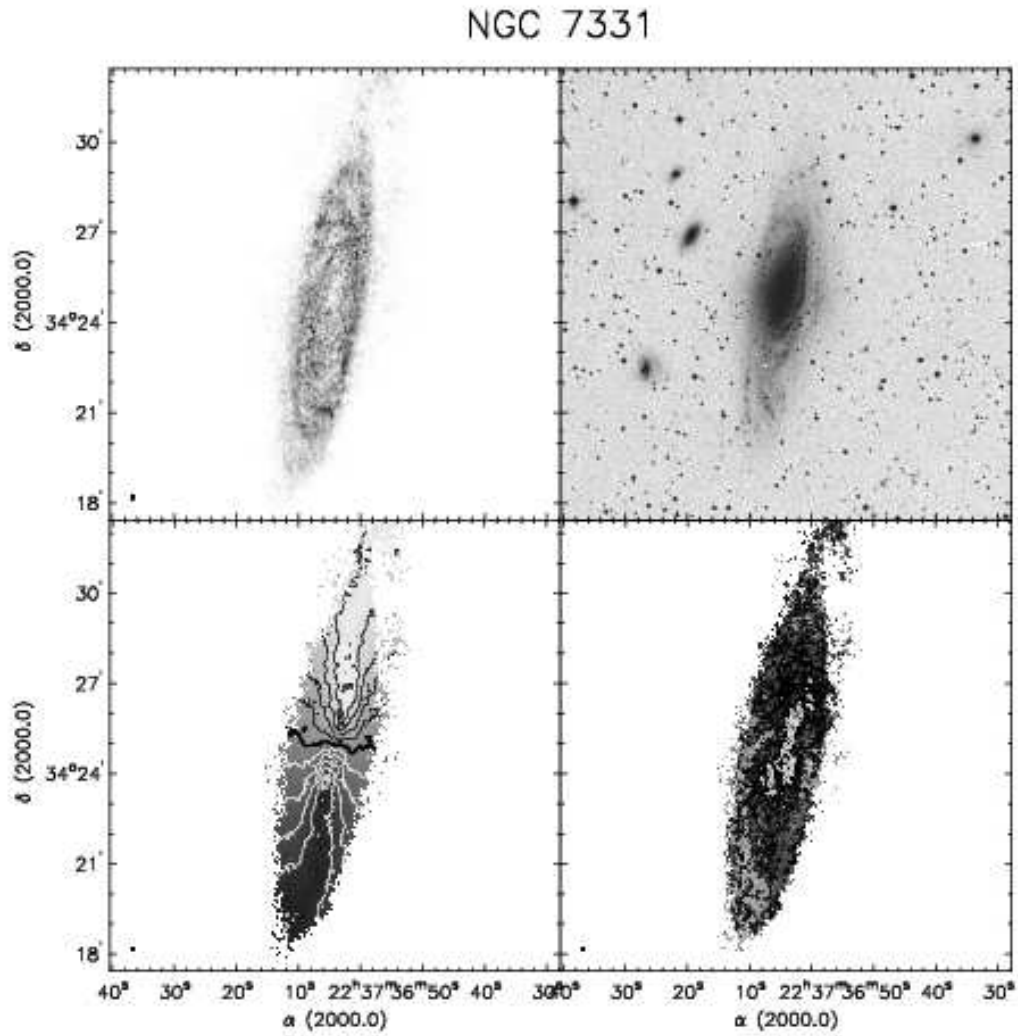


FIG. 67.— **NGC 7331**. *Top left*: integrated HI map (moment 0). Greyscale range from 0–258  $\text{Jy km s}^{-1}$ . *Top right*: Optical image from the digitized sky survey (DSS). *Bottom left*: Velocity field (moment 1). Black contours (lighter greyscale) indicate approaching emission, white contours (darker greyscale) receding emission. The thick black contour is the systemic velocity ( $v_{\text{sys}}=815.7 \text{ km s}^{-1}$ ), the iso-velocity contours are spaced by  $\Delta v=50 \text{ km s}^{-1}$ . *Bottom right*: Velocity dispersion map (moment 2). Contours are plotted at 5, 10 and  $20 \text{ km s}^{-1}$  (white contour:  $50 \text{ km s}^{-1}$ ).

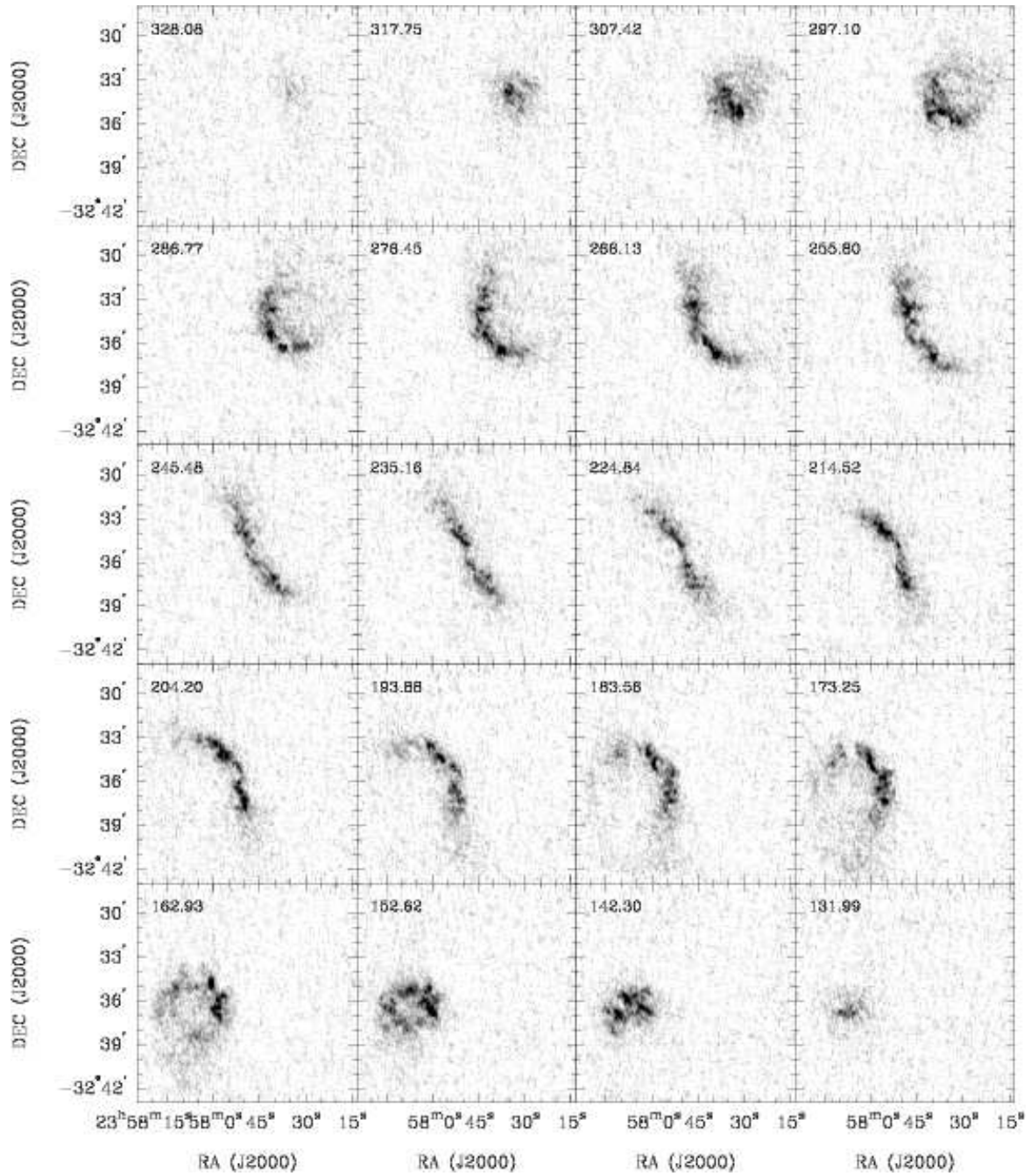


FIG. 68.— **NGC 7793**: Channel maps based on the NA cube (greyscale range:  $-0.02$  to  $14 \text{ mJy beam}^{-1}$ ). Every fourth channel is shown (channel width:  $2.6 \text{ km s}^{-1}$ ). The area shown in each panel is identical to the area shown on the next figure



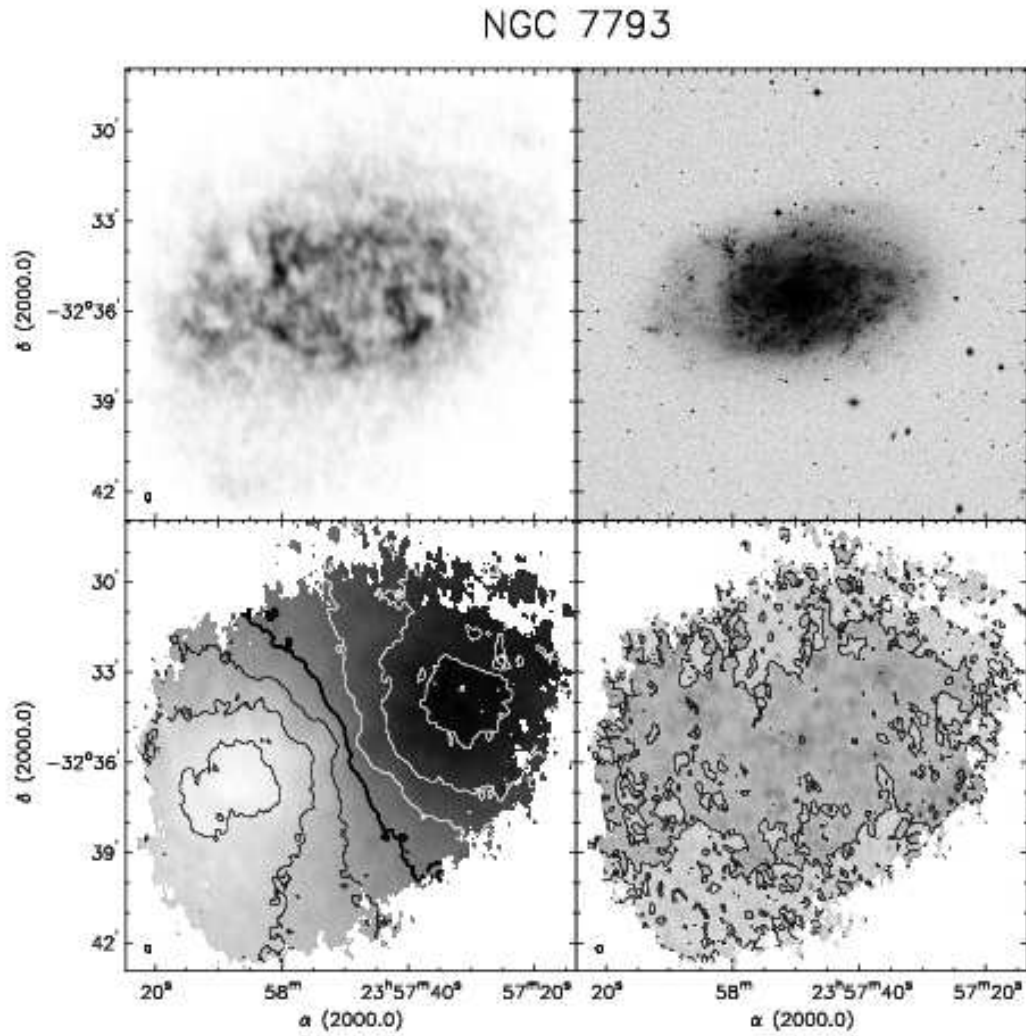


FIG. 69.— **NGC 7793**. *Top left*: integrated HI map (moment 0). Greyscale range from 0–507 Jy km s<sup>-1</sup>. *Top right*: Optical image from the digitized sky survey (DSS). *Bottom left*: Velocity field (moment 1). Black contours (lighter greyscale) indicate approaching emission, white contours (darker greyscale) receding emission. The thick black contour is the systemic velocity ( $v_{\text{sys}}=227.2$  km s<sup>-1</sup>), the iso-velocity contours are spaced by  $\Delta v=25.0$  km s<sup>-1</sup>. *Bottom right*: Velocity dispersion map (moment 2). Contours are plotted at 5, 10 and 20 km s<sup>-1</sup>.